Università della Calabria

Dottorato di Ricerca in
Scienze e Ingegneria dell'Ambiente, delle Costruzioni e dell'Energia

Tesi

ADVANCED MODELING APPROACHES FOR THE FAILURE ANALYSIS OF HETEROGENEOUS MATERIALS AND STRUCTURES

Settore Scientifico Disciplinare: ICAR/08 – Scienza delle Costruzioni

Supervisori

Prof. Ing. Fabrizio Greco

Ing. Lorenzo Leonetti

Fabrizio Greco 31.07.2024 09:25:10 GMT+00:00

LORENZO LEONETTI 31.07.2024 10:51:46 GMT+01:00

Candidato

Ing. Daniele Gaetano

DANIELE GAETANO 31.07.2024 09:57:56 GMT+00:00

Ciclo XXXVI

Il Coordinatore del Corso di Dottorato

Prof. Salvatore Critelli

Salvatore Critelli 31.07.2024 10:29:32 GMT+00:00

A.A. 2023-2024

Abstract

The development of new engineered materials and the introduction of innovative design techniques have led researchers in the field of structural engineering to focus their attention on the mechanical behavior of these materials to develop optimal and innovative design procedures to improve the structural performance of new and existing buildings, especially concerning their seismic behavior.

The most investigated aspects are, on the one hand, the mechanical characterization of complex microstructures, such as those of composite reinforced with fibers and/or particles, to be carried out taking into account the influence of the micro-constituents on the global properties, and, on the other hand, the study of the interactions between these materials and the structural elements to which these composites are applied for mechanical reinforcement, considering the damage and fracture phenomena that can potentially occur.

From a mechanical point of view, both innovative materials (e.g. composite laminates) and conventional materials (e.g. concrete, reinforced concrete, and masonry) can be considered heterogeneous materials, as they are composed of a more or less complex microstructure, made up of different constituents, usually distinguishable at very small scale compared to the dimensions of the whole structure, known as microscopic scale [1]. Being formed by the combination of distinct phases, such materials often have different (even better) mechanical properties than those of the individual constituents, but at the same time are subject to failure phenomena including:

- fiber/matrix debonding, for composites, or FRP/substrate debonding for FRP-strengthened structures;
- delamination between the different constituents for layered composites;
- matrix cracking;
- damage and plasticity phenomena;
- growth of voids in the matrix phase;
- microscopic and macroscopic instabilities due to finite deformations.

As a characteristic feature of materials with heterogeneous microstructure, the different failure mechanisms may interact with each other, especially if coupled with additional effects related to unilateral contact (with or without friction) between the surfaces of the cracks or due to the presence of imperfect interfaces between the different phases [2]. As a consequence, the analysis of these non-linear phenomena and the associated structural response, results in the solution of highly non-linear problems, which make the study of the behavior of heterogeneous materials extremely challenging, requiring highly specialized theoretical and numerical knowledge as well as accurate and computationally efficient tools.

In recent decades, different theoretical and numerical models have been developed to study the collapse mechanisms in heterogeneous materials and their influence on the overall properties in terms of strength and stiffness. Among these, for example, multiscale approaches that make it possible to analyze the response by considering the interaction that occurs between the various phenomena at different involved scales, or methods that use damage and fracture mechanics to describe the behavior of heterogeneous solids subject to damage phenomena. Besides the study of these issues, research interest in recent years has been focusing on structural health monitoring and damage identification within existing structures; the aim is to reduce the risk of collapse mechanisms within the materials so that the structural integrity is no longer compromised and premature and catastrophic collapses of the structures are avoided.

This thesis aims to develop a series of advanced numerical methods for the failure analysis of heterogeneous materials and structures, both at the meso- and micro-scale. All the developed models use a cohesive/volumetric finite element method, based on an inter-element fracture approach [3].

In particular, two models have been developed:

- A first model combining the cohesive fracture approach with a hierarchical multiscale model used to study the collapse phenomena of materials at a microscopic scale;
- A second model, based exclusively on the inter-element cohesive approach, to analyze the structural behavior of FRP-strengthened reinforced concrete elements subjected to cyclic loading conditions for structural health monitoring, as well as to investigate the failure mechanisms in masonry elements.

The key aspect of this work is to illustrate the models developed, to show the different strategies and procedures required to adapt them to different scales, and to the different materials and structures in the engineering fields.

Chapter 1 contains the introduction and a review of the technical literature, as well as the aims and objectives of the work. Chapter 2 presents the theoretical formulation of the proposed models, while Chapters 3 and 4 review the obtained numerical results.

Finally, Chapter 5 outlines the conclusions and the future perspective of the present work.

Sommario

Lo sviluppo di nuovi materiali ingegnerizzati, nonché l'introduzione di tecniche di progettazione innovative e sempre più efficienti, fa sì che uno degli argomenti al centro della ricerca nel campo dell'ingegneria strutturale sia lo studio del comportamento meccanico di tali materiali, al fine di consentire una progettazione ottimale per migliorare le prestazioni strutturali delle costruzioni, sia nuove che esistenti, con particolare riferimento al comportamento sismico.

Gli aspetti maggiormente indagati sono, da una parte, la caratterizzazione meccanica di microstrutture complesse, quali ad esempio quelle dei compositi rinforzati con fibre e/o particelle, da effettuarsi tenendo conto dell'influenza dei micro-costituenti sulle proprietà globali, e, dall'altra, lo studio delle interazioni tra questi materiali e gli elementi strutturali (realizzati con materiali convenzionali) su cui tali compositi vengono applicati ai fini del rinforzo meccanico, prendendo in considerazione i fenomeni di frattura e di danneggiamento che possono potenzialmente insorgere.

Dal punto di vista meccanico, sia i materiali innovativi (ad esempio, i laminati compositi) che i materiali convenzionali (come calcestruzzo e muratura) possono essere considerati materiali eterogenei, in quanto caratterizzati da microstruttura più o meno complessa, composta da diversi costituenti, distinguibili solitamente ad una scala di osservazione molto piccola rispetto alla scala dell'intera struttura, detta scala microscopica o micro-scala [1]. Essendo formati dalla combinazione di fasi distinte tra loro, tali materiali spesso sono dotati di proprietà meccaniche diverse (anche migliori) di quelle dei singoli costituenti, ma al contempo sono soggetti a fenomeni di collasso diversi da quelli dei materiali omogenei, tra cui:

• distacco tra rinforzo e matrice (debonding fibra/matrice nel caso dei compositi) o tra rinforzo e substrato (debonding FRP/substrato di supporto nel caso di rinforzo di elementi strutturali in calcestruzzo armato);

• distacco tra i diversi costituenti (lamine) nei laminati (detto anche delaminazione);

• fessurazione dei singoli costituenti (in particolare della matrice);

• danneggiamento e plasticità nei singoli costituenti;

• crescita di vuoti nella matrice;

• instabilità microscopiche e macroscopiche in presenza di grandi deformazioni.

Come peculiarità dei materiali con microstruttura eterogenea, i diversi meccanismi di collasso possono interagire tra loro, anche in modo complesso, soprattutto se accompagnati da ulteriori effetti legati al contatto unilatero (con o senza attrito) tra le superfici delle fessure presenti o in corrispondenza di interfacce imperfette poste tra le diverse fasi [2].

Ne consegue che l'analisi accurata dei suddetti fenomeni e della complessa risposta strutturale globale ad essi associata si traduce nella soluzione di problemi altamente non lineari e di grandi

dimensioni, che rendono lo studio del comportamento dei materiali eterogenei estremamente difficile, richiedendo conoscenze teoriche e numeriche altamente specialistiche, nonché strumenti di calcolo accurati e computazionalmente efficienti.

Negli ultimi decenni sono stati sviluppati diversi modelli teorici e numerici che permettono di analizzare i diversi meccanismi di collasso nei materiali eterogenei, nonché la loro influenza sulle proprietà globali in termini di resistenza e rigidezza. Ad esempio, gli approcci multiscala che consentono di analizzare la risposta dei materiali eterogenei considerando l'interazione che avviene tra i vari fenomeni alle diverse scale coinvolte, o i metodi che utilizzano la meccanica del danno e la meccanica della frattura per descrivere il comportamento di solidi eterogenei soggetti a fenomeni di danneggiamento. Parallelamente allo studio di queste problematiche, negli ultimi anni l'interesse della ricerca si sta concentrando sull'identificazione del danno all'interno delle strutture, ponendo sempre più attenzione al patrimonio esistente di strutture e infrastrutture. Lo scopo è quello di ridurre il rischio che possano insorgere meccanismi di collasso all'interno dei materiali in modo da non compromettere l'integrità dell'opera ed evitare collassi prematuri della struttura.

Il presente elaborato si pone l'obiettivo di analizzare una serie di metodi numerici avanzati al fine di analizzare i meccanismi di collasso nei materiali e nelle strutture eterogenee, tanto alla meso-scala quanto ad una scala microscopica. Tutti i modelli sviluppati utilizzano un metodo agli elementi finiti coesivi/volumetrici, basato su un approccio di frattura di tipo inter-elemento [3].

Nello specifico, sono stati sviluppati due modelli:

- Un primo modello che combina l'approccio di frattura coesiva con un modello multiscala di tipo gerarchico, utilizzato per studiare i fenomeni di collasso dei materiali eterogenei ad una scala microscopica;
- Un secondo modello, basato esclusivamente sull'approccio coesivo inter-elemento, al fine di analizzare il comportamento strutturale di elementi in calcestruzzo e calcestruzzo armato rinforzati mediante l'applicazione di FRP, soggetti a fenomeni di danneggiamento e sottoposti a condizioni di carico ciclico ai fini dell'identificazione del danno nelle strutture esistenti, nonché per analizzare i fenomeni di rottura negli elementi in muratura.

L'aspetto chiave della presente tesi è quello di illustrare i modelli sviluppati, mostrare le diverse strategie e procedure necessarie al fine di adattarli alle diverse scale, ed ai diversi materiali e strutture presenti nel campo ingegneristico.

Il capitolo 1 contiene l'introduzione ed una rassegna della letteratura di interesse, nonché gli obiettivi e gli scopi dell'elaborato. Nel capitolo 2 viene riportata la formulazione teorica del modello, mentre nei capitoli 3 e 4 vengono passati in rassegna i risultati numerici ottenuti. Infine, il capitolo 5 contiene le conclusioni ed i possibili sviluppi futuri del presente lavoro.

List of Contents

List of Figures

List of Tables

Introduction

As is widely known, structural materials are prone to different failure phenomena that may compromise their efficiency and integrity leading to catastrophic and premature collapses in structures.

From a mechanical point of view, both innovative materials (e.g. composite laminates) and conventional materials (e.g. concrete, reinforced concrete, and masonry) can be considered heterogeneous materials, as they are composed of a more or less complex microstructure, made up of different constituents, usually detectable at a very small scale compared to the dimensions of the whole structure, known as microscopic scale [1]. Being formed by the combination of distinct phases, such materials often have different, and even better, mechanical properties than those of the individual constituents, but at the same time are subject to failure phenomena including:

- fiber/matrix debonding, for composites;
- delamination between the different constituents;
- matrix cracking;
- damage and plasticity phenomena;
- growth of voids in the matrix phase;
- microscopic and macroscopic instabilities due to finite deformations.

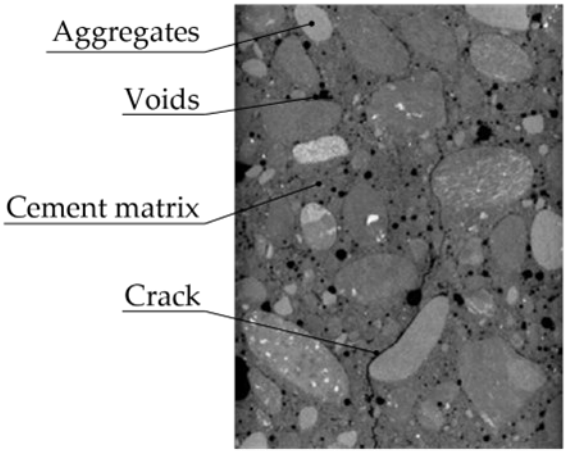

Fig. 1. Detail of concrete microstructure with voids and cracks.

As a characteristic feature of materials with heterogeneous microstructure, the different failure mechanisms may interact with each other, especially if coupled with additional effects related to unilateral contact (with or without friction) between the surfaces of the cracks or due to the presence of imperfect interfaces between the different phases [2]. As a consequence, the analysis of these non-linear phenomena and the associated structural response of the structure leads to the solution of highly non-linear problems, which makes the study of the behavior of heterogeneous materials extremely

challenging, requiring highly specialized theoretical and numerical knowledge as well as accurate and computationally efficient tools.

All these failure mechanisms are mostly triggered at the microscopic level, generated by physical phenomena reliant on the mechanical properties of the materials, and then spreading to the macroscopic scale, affecting the strength and stiffness of the whole structure. To this end, it is, therefore, necessary to properly investigate the mechanical characterization of the microstructure of the single materials by considering the influence of the micro-constituents on the overall properties and incorporating possible damage and fracture phenomena that may arise.

In order to take into account all these potential failure mechanisms in heterogeneous materials, fully microscopic problems should be formulated and subsequently solved, being able to provide a complete description of all the microstructural details as well as of their evolution [4,5]. Nevertheless, the related numerical simulations would be unpractical due to the resulting huge computational effort, so more efficient approaches are usually required for engineering applications. In particular, two alternative classes of models have been extensively used to define accurate material behaviors for complex microstructures: phenomenological models and micromechanical models. The former consider the effects of micro-cracks on the material's response at the macroscopic scale through the introduction of damage state variables related to the reduction of the material stiffness. Many of them have been developed within the Continuum Damage Mechanics (CDM) field for isotropic materials and then adapted to the anisotropic ones [6,7]. The main con of these approaches is that they lead to difficulties in identifying a large number of associated material parameters.

The latter, instead, can predict the overall response of heterogeneous materials starting from the supposedly known properties of the microscopic constituents. This is possible by defining either numerical or analytical relationships between the microscopic and macroscopic fields [8–10].

Scope and outline

The growing interest in the analysis of damage phenomena in heterogeneous materials and structures, motivated by the continued focus on existing structures and the interest in improving the capabilities of innovative materials, has led researchers to develop increasingly advanced numerical models that allow accurate prediction of material behavior and the evolution of damage phenomena within structures.

It is therefore important to be able to understand the behavior of materials and structures at both a macro/mesoscopic and microscopic scale. In view of this duality, this work aims to develop a numerical fracture model based on a cohesive/volumetric finite element framework, which can be applied to both scales.

In particular, the developed cohesive approach has been used in combination with a hierarchical multiscale model for the collapse analysis of heterogeneous materials at a microscopic scale with applications on composite materials, and subsequently at a macroscopic scale for the study of the main collapse mechanisms in concrete, reinforced concrete and masonry structures.

The outline of the thesis is as follows.

Chapter 1 contains an extensive overview of the technical literature behind the numerical methods proposed in the present work. In particular, after a brief introduction to the basic concepts of damage and fracture mechanics, the numerical approaches for fractures in quasi-brittle materials are reported. Subsequently, a review of the multiscale methods for composites is presented, after the introduction to the basic homogenization theories.

In Chapter 2, the developed numerical method based on the cohesive fracture approach will be presented. In the first part of the chapter, the theoretical background of the adopted method is presented concerning the variational formulation for the case of planar elasticity. In the second part, the novel aspects of the models are presented to adapt the approach to the different case studies. The two-scale finite element model, based on a hybrid continuous/discontinuous hierarchical homogenization, is presented for composite with period microstructure. In this model, the cohesive fracture approach introduced in the first part of the chapter is accounted for to capture multiple cracking at the microscopic scale. Subsequently, the improvement of the variational formulation for studying reinforced concrete structures subjected to cyclic loading conditions is introduced, regarding the effect of concrete plasticity on the proposed numerical model. At the end of the chapter, instead, the mixed-mode frictional interface model for the failure simulation of masonry structures is introduced underlying the main adjustment necessary to adapt the method in order to capture the failure mechanisms of masonry materials.

Chapter 3 and Chapter 4 are devoted to the numerical results obtained for the failure analysis of heterogeneous materials and for the non-linear analysis of load-induced degradation of vibration characteristics in structural elements.

Finally, in Chapter 5 the conclusions and the future perspectives of the work are given with comments and observations about the obtained numerical results and the possible improvements of the proposed numerical methods.

1. Numerical approaches for fracture analysis in quasi-brittle materials

The study and development of numerical models for the analysis of fracture phenomena in quasi-brittle materials has been, and still is, one of the most investigated topics in the field of fracture mechanics. Over the years, different approaches have been taken by the researchers to investigate such issue. Initially, the behavior of fractured bodies, as is known to be highly complex and difficult to analyze, has been mostly studied with theoretical approaches based mainly on Linear Elastic Fracture Mechanics (LEFM). Such approaches, which are still used today due to their simplicity and their basic concepts in the field of fracture mechanics, fail to capture all the complex fracture phenomena that quasi-brittle materials exhibit. Therefore, in recent years, reliance has been placed on more sophisticated models based on Finite Element Method (FEM), involving both discrete and continuous damage mechanics models. Such approaches overcome the issues of simplified theoretical models by providing increasingly accurate results and thus being able to properly describe the behavior of quasi-brittle materials subjected to fracture phenomena. In this chapter, an extensive review of the aforementioned numerical fracture models is given, not without recalling the basic theoretical concepts of fracture mechanics, on which, as is important to remember, these models are based. However, it is important to emphasize that a detailed analysis of the evolution of fracture theories and their specific formulation is beyond the scope of this work. Therefore, for the sake of brevity, only a brief literature review with appropriate references will be presented, before moving instead into a deep explanation of the computational approaches for cracking analysis, that are the subject of the present work. For any further details, please refer to the references cited at the beginning of the following section.

1.1 Computational modelling approaches for cracking analysis

Before moving on to the subject of computational approaches for cracking analysis in quasi-brittle materials, it is important to briefly introduce the basic concepts of fracture mechanics.

Fracture mechanics is the discipline that studies the behavior of fractured solids. Fracture refers to the irreversible process that leads to rupture within the material, following the steps of crack onset and growth. This process is influenced by a large number of factors, e.g. microstructure of the considered solid or the boundary conditions to which it is subjected, etc. In order to study the fracture phenomena, it is therefore necessary to introduce the basic principles of fracture mechanics. To this end, two main theories have been widely used: Linear Elastic Fracture Mechanics (LEFM) and Elastic-Plastic Fracture Mechanics (EPFM). The former, used to study the behavior of brittle materials, assumes that non-linear effects and, therefore, anelastic deformations can be neglected.

This simplification is accepted in brittle materials where such non-linear effects are concentrated and limited within a very small area, i.e. at the tip of the cracks. The latter, on the other hand, seeks to overcome the limitations introduced by LEFM and it is used to study the fracture behavior of all those materials for which the extension of the inelastic deformations can no longer be neglected.

The LEFM is applicable to all materials whose behavior can be assumed to be linearly elastic, as long as the extension of the area in which anelastic deformations are present is small, compared to the crack or body sizes. The results provided by the LEFM are very accurate whenever the previous assumptions are met [11].

One of the first works on fractured bodies was presented by Inglis in 1913 [12]. He analyzed the behavior of a uniformly stressed elliptical cavity and observed that the closer the ellipse came to a line, the more the stresses at the ellipse's vertices tended towards infinity. However, the work that revolutionized the subject was that of Griffith in 1921 [13], who analyzed the phenomenon in elastic bodies starting from an isolated crack. Based on the fundamental energy theorems of mechanics and thermodynamics, Griffith succeeded in defining a criterion for crack propagation based on an energy equilibrium principle: the crack can propagate inside the body if the energy available to extend the crack by a unit surface area equals the energy required to do so.

At this point, therefore, it was necessary to introduce analytical formulations, in addition to Griffith's own and based on his work, in order to evaluate this available energy. This was done with the works of Iwrin [14] and Rice [15,16]. In particular, the former introduced asymptotic expressions of the stress field to evaluate the energy available for fracture. The latter, based on the assumption of non-linear elastic behavior around the crack tip, proposed an alternative method to estimate the amount of the required energy to fracture through a contour or a line integral that encloses the crack front.

Alongside LEFM, Elastic-Plastic Fracture Mechanics (EPFM) has been developed for all those bodies for which inelastic deformations can no longer be neglected. The physical phenomenon beyond the introduction of this branch of fracture mechanics is to be found in the fact that for some bodies, due to the concentration of stresses at the crack tip, a plastic zone develops when the yield stress of the materials is exceeded. The size of this plastic zone, which increases as the load increases, may extend over a large region or the entire solid, depending on the geometric and material properties, until crack onset takes place. In such an area, due to the fact the local stresses are limited to the yield strength of the material, the linear elastic fracture mechanics is no longer accurate for evaluating the fracture parameters. Furthermore, the stress-intensity factors are meaningless, since as we know they are valid for materials with linear-elastic behavior. However, it was clear that the size of the plastic zone could have been a corrective parameter for the evaluation of the effective stress-intensity factor, taking into account the plastic effects around the crack tip. Therefore, it was necessary to assess the

extension of this plastic zone. According to the assumption of small-scale yielding, this size is small compared to the size of the structure or the extension of the crack. This aspect, therefore, has been the subject of important works by several researchers, including the most famous works of Irwin [17] and Dugdale [18]. The goal for both of them was to estimate the extension of the fracture zone at the crack tip and then, modify the energy balance equation introduced by Griffith [13]. Furthermore, EPFM introduced a new local measure of the plastic strains around the crack tip, the so-called crack tip opening displacement (CTOD) [19,20]. Such quantity was introduced as an experimentally motivated quantity, as opposed to the known classical fracture parameters.

The most important fracture theories previously introduced, based on the assumption that the fracture process is lumped all into the tip of a sharp crack, neglect a detailed description of the fracture behavior in the neighborhood of the crack tip, i.e. in the so-called fracture process zone (FPZ). However, the real FPZ extension is not negligible in small- and medium-sized structures, which are the most common ones in the engineering practice.

Around 1960s, in some experimental tensile tests, a strain softening behavior with a decrease in the loading carry capacity, i.e. a negative slope in the stress-deformation curve is observed in concrete specimens [21], due to microcracking and localization of the deformation in a narrow band where energy dissipation occurs. From a computational point of view, especially in the continuum analysis, the strain softening behavior could introduce some numerical phenomena related to the loss of both stability and uniqueness of the solution, and bifurcation of the equilibrium path. The first to encounter such issues were Rashid [22] and Scanlon [23] during the concrete cracking analysis in the framework of the finite element method (FEM). In particular, adopting the so-called *damage models* in which the cracking process is simulated through suitably defined constitutive relations, they discovered that the energy dissipated by the fracture decreases with the refinement of the mesh and converges to zero, leading to results strongly dependent on the mesh size. To avoid this spurious mesh sensitivity, suitable regularization approaches must be introduced in the model, thus leading to a correct capturing of damage-induced softening.

In the literature, two models' groups with different softening constitutive laws can be distinguished: cohesive crack models, and smeared crack models. The former models assume a softening constitutive law, based on a stress-crack opening displacement relation, to simulate the material behavior of the so-called *fictitious crack*, that is the extension of the real crack where the material keeps its ability to transfer the stress. The latter models, instead, introduce a softening stress-strain relation included in a band around the crack in order to describe the fracture process in a wide range of materials.

In the following Sections a description of both above-mentioned models is presented, together with some of the related computational details.

1.1.1 Cohesive Zone models

The first reference to the cohesive model can be found in Barenblatt's pioneering work of 1962 [24], where the sentence "*cohesive zone*" is used to describe the region where the atomic forces interact with each other across the faces of an opening crack. This stems from the idea that the failure process during the fracture of a given material only occurs in a *narrow strip-shaped* zone in front of the main crack [25], within which the damage propagates until separation occurs. Another pioneer model was developed by Dugdale [18] for the simulation of the crack in ductile metal sheets. Over the years, other researchers have used cohesive zone models to investigate fracture phenomena in different materials; for instance, Hillerborg et al. [26], applied a cohesive method for crack simulation in concrete structures, Petersson [27], developed a cohesive FE formulation based on a boundary integral method for concrete behavior under mode-I loading condition, and Ingraffea and Gerstle [28], that analyzed the mixed-mode loading condition.

1.1.1.1 Basic concepts of the cohesive approach

The cohesive approach assumes that a fictitious crack, where the material albeit damaged is still able to transfer stresses, begins to form when the principal tensile stress reaches the critical tensile strength of the material. In this zone, called fracture process zone (FPZ), the stresses transferred by the material are governed by a traction-separation cohesive law and decrease as the displacement discontinuity increases, while outside of this region, the material behavior is linear-elastic. Such a cohesive function, which describes the interaction force between the two crack faces, represents a real local material property and relates the traction force and the opening displacement of the crack. In the literature, several cohesive laws have been proposed, which differ from each other according to various materials and failure mechanisms [29]. However, it does not exist a "natural" cohesive law given a priori, since the cohesive model is a phenomenological model that does not claim to model the real physical fracture process, so the choice of a separation law is free. In Fig. 2 some typical shapes of traction-separation law are illustrated. They can be collected into two main groups: intrinsic cohesive laws (Fig. 2(a), and Fig. 2(b)), characterized by a linear-elastic branch before the softening branch and usually employed in fracture analysis for which the cohesive elements are inserted prior to the simulation along predefined crack paths, and extrinsic cohesive law (Fig. 2(c)), without the initial linear-elastic branch, because the cohesive elements are inserted during the simulation (i.e. on the fly) in the area where the critical tensile strength of the material has already been reached.

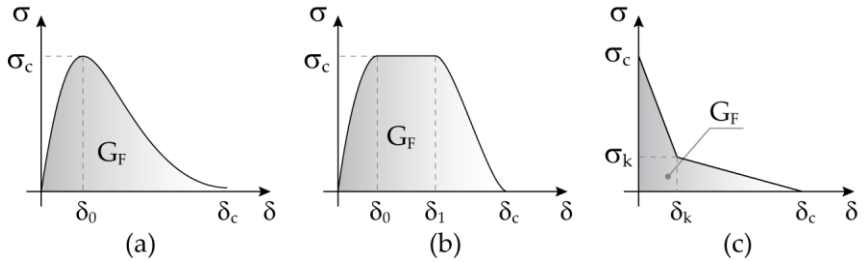

Fig. 2. Exponential (a), trapezoidal (b) and bi-linear (c) traction-separation law

In particular, the intrinsic cohesive relation starts with a linear-elastic branch in which the stress increases with growing crack opening displacement, up to a maximum value σ_c, called cohesive strength, which is regarded as a material property. After which, a softening branch usually characterized by a decrease in the load-carrying capacity occurs until a critical decohesion opening δ_c is reached, then the material is completely separated, and no stress can be transmitted. Integrating the traction-separation law up to the critical opening δ_c, i.e. computing the area under the separation curve, the dissipated fracture energy G_F during the crack propagation is obtained:

$$G_F = \int_0^{\delta_c} \sigma(\delta) d\delta \tag{1}$$

A fully exponential law, depicted in Fig. 2(a), based on an energy potential of atomic bonds [30], is proposed by Needleman [31] in a modified form for cohesive zone models in which the dependence of the traction forces on the opening displacement is given by:

$$\sigma(\delta) = \sigma_c \frac{\delta}{\delta_0} \exp\left(-\frac{\delta}{\delta_0}\right) \tag{2}$$

After a quasi-linear branch up to the critical strength, σ_c, the curve decays exponentially. A characteristic feature of this model is that the traction does not approach zero at finite $\delta = \delta_c$.

In the failure analysis of ductile materials, such as metals, an alternative intrinsic cohesive law, illustrated in Fig. 2(b), with a region of constant maximum tension before the softening branch, is proposed by Tvergaard and Hutchinson [32]. Such a trapezoidal law has been obtained by using an additional parameter δ_1, which can be freely chosen, leading to the following formulation for the function $\sigma(\delta)$:

$$\sigma(\delta) = \begin{cases} \sigma_c \left[2\left(\dfrac{\delta}{\delta_0}\right) - \left(\dfrac{\delta}{\delta_0}\right)^2 \right] & \text{for } \delta < \delta_0 \\ \sigma_c & \text{for } \delta_0 < \delta < \delta_1 \\ \sigma_c \left[2\left(\dfrac{\delta - \delta_1}{\delta_c - \delta_1}\right)^3 - 3\left(\dfrac{\delta - \delta_1}{\delta_c - \delta_1}\right)^2 + 1 \right] & \text{for } \delta_1 < \delta < \delta_c \end{cases} \tag{3}$$

In the pioneering work of Petersson on crack propagation analysis in concrete structures, an extrinsic bi-linear traction-separation law, shown in Fig. 2(c), is used to simulate the behavior of cohesive elements inserted adaptively when a stress criterion is satisfied [27]. The softening stress can be written as:

$$\sigma(\delta)=\begin{cases}\sigma_c-\dfrac{(\sigma_c-\sigma_k)\delta}{\delta_k} & \text{for } \delta<\delta_k\\ \sigma_k-\dfrac{\sigma_k(\delta-\delta_k)}{(\delta_c-\delta_k)} & \text{for } \delta_k<\delta<\delta_c\end{cases} \tag{4}$$

where σ_k and δ_k are the kink point coordinates. To fit the experimental results, describing the concrete fracture behavior more realistically, Petersson proposes $\sigma_k=\sigma_c/3$ and $\delta_k=2\delta_c/9$. Finally, the essential parameters required by a traction-separation law, needed to implement a cohesive crack model in its simplest form, are the tensile strength and the fracture toughness (or fracture energy) of the tested material, which can be easily obtained by simple experimental tests.

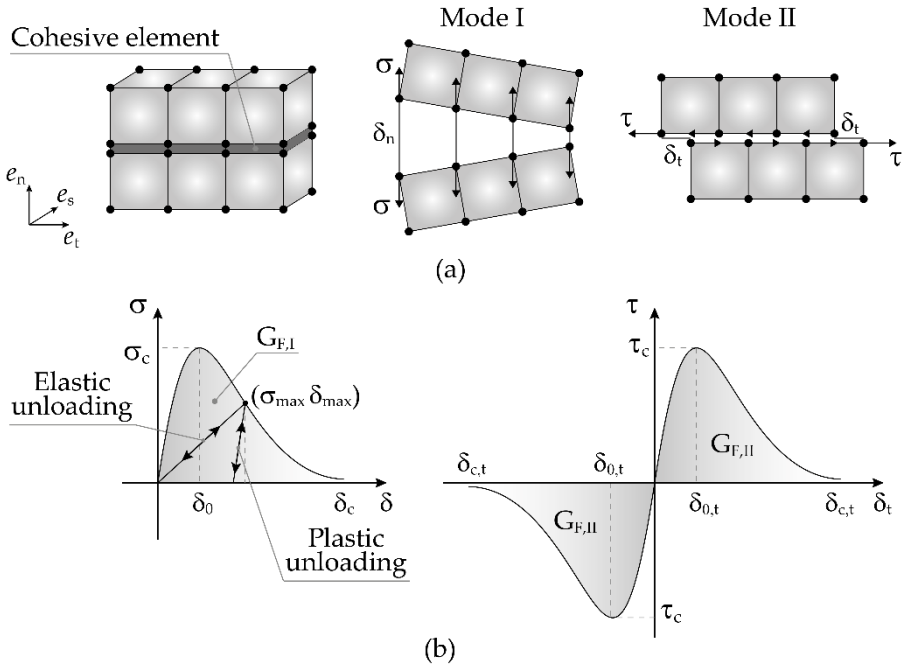

Fig. 3. Mode-I and Mode-II loading conditions in a 2D cohesive finite element framework (a) and cohesive laws (b).

In a general loading condition, the nodes of the damaged interfaces move in the perpendicular direction to the crack (mode I), but they can also shift to each other in the tangential (mode II) and transversal (mode III) directions to the crack (Fig. 3(a)). Thus, the opening displacement vector $\delta=[\delta_n\ \delta_t\ \delta_s]^T$ is defined in the local coordinate system $(\mathbf{e}_n,\mathbf{e}_t,\mathbf{e}_s)$. The cohesive stresses and the opening displacement, in a two-dimensional case, are related by:

$$\begin{matrix}\mathbf{t}=\sigma\mathbf{e}_n+\tau\mathbf{e}_t\\ \boldsymbol{\delta}=\delta_n\mathbf{e}_n+\delta_t\mathbf{e}_t\end{matrix},\quad \mathbf{t}=f(\boldsymbol{\delta})\ \text{ or }\ \begin{cases}\sigma=f_n(\delta_n,\delta_t)\\ \tau=f_t(\delta_n,\delta_t)\end{cases} \tag{5}$$

In Fig. 3(b), a typical cohesive law for two-dimensional analysis, which describes both separation modes (I and II), is depicted. It is worth noting that, the normal stress is confined by the constraint $\delta \geq 0$, since otherwise a contact of crack faces occurs, producing additional reaction forces to avoid material interpenetration. In the mode-II relation, the tangential stresses change their sign if the direction of the sliding displacement δ_t changes. An alternative method for simulating the local mixed-mode condition and avoiding considering a cohesive law for each separation mode is proposed by Ortiz and Pandolfi [33], based on the introduction of an *effective displacement* δ, relating both normal and tangential local displacements:

$$\delta=\sqrt{(\delta_n)^2+(\eta\delta_t)^2} \tag{6}$$

whereby, the factor η determines the ratio between shear and tensile stiffness in the cohesive law.

The normal and tangential stress functions can be derived from an energy potential Φ_e. For instance, the exponential law proposed by Needleman [31] can be obtained by considering the following energy potential:

$$\Phi_e(\delta)=\int_0^{\delta_c}\sigma(\delta)d\delta=G\left[1-\left(1+\frac{\delta}{\delta_0}\right)\exp\left(-\frac{\delta}{\delta_0}\right)\right] \tag{7}$$

By using the expression for the effective displacement δ, the normal and tangential cohesive laws can be extracted as:

$$\begin{matrix}\sigma=\dfrac{\partial\Phi_e}{\partial\delta_n}=\dfrac{t}{\delta}\delta_n,\\ \tau=\dfrac{\partial\Phi_e}{\partial\delta_t}=\dfrac{t}{\delta}\eta^2\delta_t\end{matrix}\quad, \tag{8}$$

from which an effective cohesive stress can be defined as:

$$t=\sqrt{(\sigma)^2+\left(\frac{\tau}{\eta}\right)^2}\ . \tag{9}$$

The unloading during the irreversible fracture process is taken into account by the traction-separation law in the numerical analysis. In particular, up to the critical tensile strength of the material, the unloading runs elastically on the same curve to the origin. In the softening branch, instead, the unloading and eventually re-loading occur along a different path. If a quasi-brittle material is simulated, the unloading path follows towards the origin, instead, for ductile material the unloading runs parallel to the initial elastic slope and a plastic deformation occurs. In both cases, the maximum

value of the effective displacement $\delta_{\max}$ over the entire loading history is necessary to be computed, so that:

$$\text{Loading:} \quad \delta = \delta_{\max}$$

$$\text{Unloading:} \quad \delta < \delta_{\max} \begin{cases} \text{elastic}: \; t = a\delta \quad \text{with} \quad a = \dfrac{\partial^2 \Phi_e(0)}{\partial \delta^2} \\ \text{plastic}: \; t = \dfrac{t_{\max}}{\delta_{\max}} \delta \end{cases} . \tag{10}$$

The cohesive crack approach is generally used in conjunction with computational techniques to approximate the nonlinear fracture process. Within a finite element setting, two main strategies to investigate failure can be found in the literature, i.e. inter-element and intra-element models. They will be explained in detail in the next Sections.

1.1.1.2 Inter-element cohesive models

In inter-element cohesive models, cracks are constrained to be extended between the finite element of the mesh, and their propagation is allowed by using specific interface elements, equipped with a constitutive relation, written in terms of the above-mentioned traction separation law. Such cohesive interface elements can be a priori inserted in the case of a known crack path, for example, to simulate debonding problems in composite laminates. Instead, in the case of unknown crack paths, these elements are inserted during the simulation, adaptively. Several cohesive interface models of this kind have been proposed in the literature to analyze mixed-mode fracture in concrete and other quasi-brittle materials [34–39]. Here, two of the main inter-element cohesive models will be explained, highlighting their advantages and/or potential drawbacks in the failure analysis.

1.1.1.3 Cohesive/volumetric finite element model proposed by Xu and Needleman

A particular inter-element cohesive model is proposed by Xu and Needleman [3] to investigate the dynamic crack growth and crack branching phenomena in isotropic elastic solids subjected to tensile loading conditions. The basic idea of the model is to disperse potentially damaging cohesive surfaces over the discretized body. Thus, a crossed-triangle quadrilateral mesh, in a finite element framework, consisting of volumetric finite elements bordered by cohesive surface elements is involved to perform dynamic crack analysis (Fig. 4).

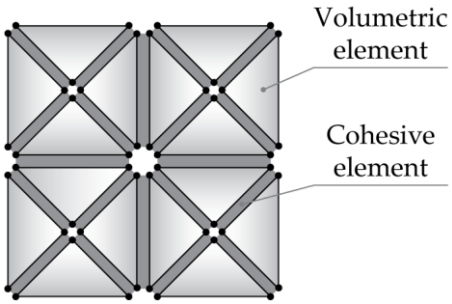

Fig. 4. Representation of the cohesive/volumetric finite element method.

A constitutive law that relates stress and strain governs the elastic behavior of volumetric bulk elements, while a traction-displacement jump law is used to describe the nonlinear behavior of a specific set of cohesive surfaces, that are interspersed throughout the continuum.

The equilibrium problem of the discretized body was formulated as a nonlinear boundary value problem (BVP) expressed in the following weak form:

$$\int_V \mathbf{s} : \delta\mathbf{F} dV - \int_{S_{int}} \mathbf{T} \cdot \delta\boldsymbol{\Delta} dS = \int_{S_{ext}} \mathbf{t} \cdot \delta\mathbf{u} dS - \int_V \rho \frac{\partial^2 \mathbf{u}}{\partial t^2} \cdot \delta\mathbf{u} dV \tag{11}$$

where $\mathbf{s}$, $\mathbf{F}$, $\mathbf{t}$ and $\mathbf{T}$ are the nonsymmetric nominal stress tensor, the gradient of deformation, the external load vector, and the cohesive traction vector, respectively. The displacement jump across the cohesive surface is denoted as $\boldsymbol{\Delta}$, whilst, V, S_{int}, and S_{ext} are the volume, external surface, and internal cohesive surface, respectively. The symbol ρ represents the density of the material. A constitutive law for isotropic hyper-elastic bulk elements is considered so that the second Piola-Kirchhoff stress tensor is:

$$\mathbf{S} = \mathbf{s} \cdot \mathbf{F}^{-1} = \frac{\partial W}{\partial \bar{\mathbf{F}}} \tag{12}$$

where W represents the strain energy density. The Lagrangian strain tensor $\bar{\mathbf{F}}$ is given by:

$$\bar{\mathbf{F}} = \frac{1}{2}(\mathbf{F}^{T} \cdot \mathbf{F} - \mathbf{I}) \tag{13}$$

where $\mathbf{I}$ is the identity matrix.

Cohesive elements are equipped, instead, with a phenomenological mechanical constitutive relation between the traction and the displacement jump. Fully exponential intrinsic laws, used to describe the cohesive forces behavior for each fracture mode (mode I and II), are obtained by the energy potential Φ illustrated in [3], so that:

$$\mathbf{T} = \frac{\partial \Phi}{\partial \boldsymbol{\Delta}} \tag{14}$$

The cohesive/volumetric FE model has been used to perform a dynamic analysis of the wave propagation in a block with and without an initial crack. The specimen is discretized by quadrilateral

elements, enriched with diagonal elements at 45°, all surrounded by cohesive surface elements. The effect of varying the impact velocity on the crack branching was investigated. Fig. 5 shows the crack pattern of the block subjected to symmetric loading condition with wave speeds equal to 1 ms^{-1} (a), and 15 ms^{-1} (b).

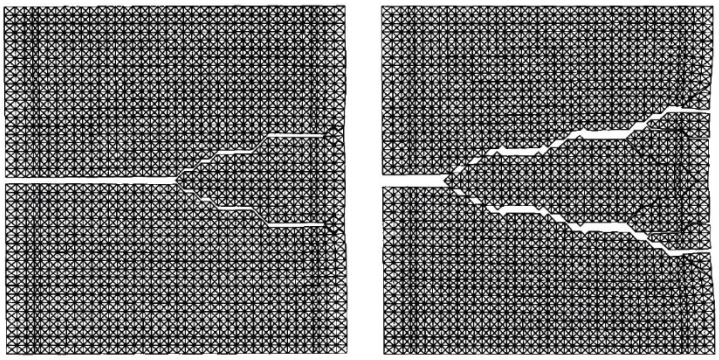

Fig. 5 Deformed mesh of a block under dynamic loading conditions [3]

The main result of the analysis is that the higher the impact velocity the less crack growth there is before branching. Focusing on the crack pattern, we can note that the model can capture the crack branching phenomena accurately, and although the crack can only propagate in parallel and 45° direction with respect to the axes, the overall branching angle is noticeably less than 45°, as demonstrated by experimental results. In addition, considering a pre-cracked block, a study of the orientation effect of the cohesive surface elements on the crack path was carried out. Four mesh configurations were built by varying the orientation angle of diagonal elements. The crack pattern of the different configurations with diagonal elements inclined by 15°, 30°, 45°, and 60° respect to the x-axis are depicted in the following figures.

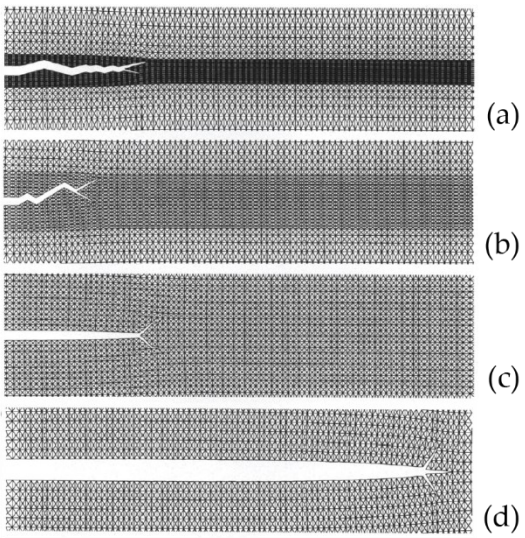

Fig. 6 Mesh orientation sensitivity analysis performed by [3].

A zig-zag crack growth is predicted by the configurations with angles of 15° and 30°, even though the meshes and boundary condition are symmetric, while a crack propagation in the horizontal direction is obtained by the other configurations. It is worth noting that, also the onset of the crack branching phenomena is also strongly influenced by discretization.

The above-discussed diffuse cohesive formulation, consisting of cohesive surface elements inserted along all the mesh boundaries, is one of the first applications of the cohesive approach within the finite element method. In this model, the use of a structured triangulation highlighted the well-known mesh dependency issues of the inter-element fracture approaches, in terms of lack of spatial convergence for arbitrary crack paths or patterns, as shown in the Fig. 6.

Furthermore, it has been largely demonstrated that unstructured meshes with very good isotropic properties, i.e. Delaunay mesh, can reduce such artificial mesh effects, especially in terms of sensitivity to the mesh orientation, even if the question of energy convergence remains an open issue.

1.1.1.4 Adaptive cohesive volumetric finite element model proposed by Camacho and Ortiz

In the inter-element discrete fracture framework, an alternative cohesive volumetric FE model to predict the propagation of dynamic fracture and fragmentation in brittle materials subjected to impact load is developed by Camacho and Ortiz [40]. The proposed model, based on an extrinsic cohesive approach, adaptively creates new cohesive surfaces as a brittle fracture criterion is satisfied, duplicating nodes along boundaries of the coherent finite elements. In this way, the nucleation and propagation of the single or multiple cracks as well as the branching and fragmentation phenomena can be easily simulated Fig. 7.

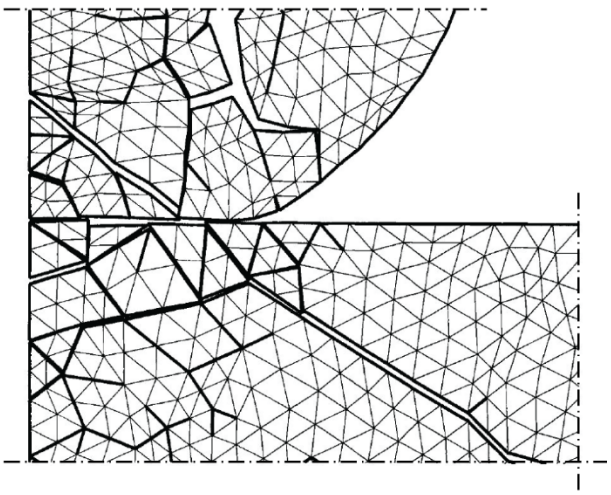

Fig. 7 Adaptive cohesive volumetric finite element model [40]: Crack phenomena.

An advancing front algorithm to mesh generation is used to discretize the domains of the analyzed body involving six-node triangular elements finite elements (Fig. 8) and also useful to defining the contact surfaces.

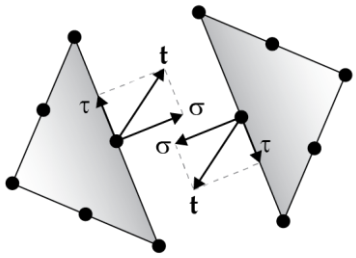

Fig. 8. Six-node triangular element with representation of the cohesive traction vector and its component.

Such an algorithm modifies the computational information of boundaries and nodes during the creation of crack surfaces and adds new domains to the system if complete fragmentation occurs. In this model, which also employs a contact/friction algorithm for the self-contact across crack faces, the dynamic equilibrium problem is written in weak form by the virtual work principle at the time t_{n+1}, as follows:

$$\int_V \mathbf{P} : \nabla \boldsymbol{\eta} dV - \int_V (\mathbf{f} + \rho \mathbf{a}) \cdot \boldsymbol{\eta} dV - \int_S \mathbf{t} \cdot \boldsymbol{\eta} dS = 0 \tag{15}$$

where $\mathbf{P}$ and ∇ are the first Piola-Kirchhoff stress and the material gradient, respectively. The body forces, accelerations, and boundary traction are denoted as $\mathbf{f}$, $\mathbf{a}$, and $\mathbf{t}$, respectively. The symbol $\boldsymbol{\eta}$ represents an admissible virtual displacement field. The normal σ and tangential τ components of the cohesive traction $\mathbf{t}$, calculated at each load step and at each node of the strain six-node triangular elements, are used to verify mixed-mode fracture criteria proposed by several authors [41,42]:

$$\begin{aligned} &\sqrt{\sigma^2 + \beta\tau^2} \geq \sigma_{fr} \quad \text{if } \sigma \geq 0 \\ &\sqrt{\beta}\left\langle |\tau| - \mu|\sigma| \right\rangle \geq \sigma_{fr} \quad \text{if } \sigma < 0 \end{aligned} \tag{16}$$

where β, μ, and σ_{fr} are the shear stress factor, friction coefficient, and the critical fracture stress of the material, respectively. When one of the fracture conditions of (16) is satisfied, a new cohesive surface is introduced into the mesh by the interested nodes duplication. The new cohesive surface elements are equipped with an irreversible extrinsic-type linear softening law for each fracture mode, as depicted in Fig. 9.

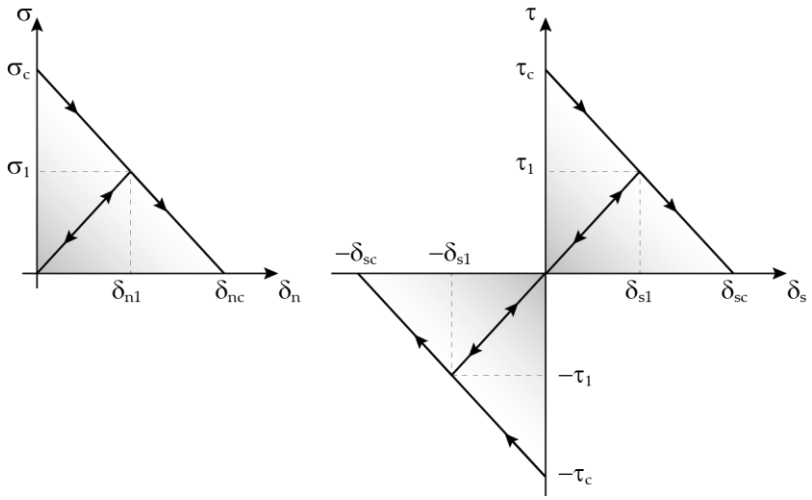

Fig. 9 Normal and tangential cohesive law defined by [40].

The relations between the components of cohesive traction and the displacement jump are the following:

$$\sigma = \sigma_c \left(1 - \frac{\delta_n}{\delta_{nc}}\right)$$
$$\tau = \tau_c \left(1 - \frac{|\delta_s|}{\delta_{sc}}\right) \mathrm{sgn}(\delta_s) \tag{17}$$

where δ_n and δ_s are the normal opening and sliding displacements, respectively. The subscript c denotes the critical value of the quantity. As soon as the cohesive stresses reach the corresponding critical values of the material (σ_c and τ_c), they are ramped down linearly as a function of the displacement jump. The critical opening displacement δ_{nc}, can be obtained by the fracture energy, which represents the area under the tensile cohesive law, and it can be measured in fracture tests. If unloading occurs, the crack begins to close, and the stresses follow an unloading path towards the origin.

1.1.1.5 Intra-element cohesive models

To model crack initiation and propagation along unknown crack paths without involving any remeshing operations, intra-element cohesive fracture approaches are widely used. Such approaches allow the propagation of the cracks within the finite elements of a given mesh by introducing kinematic enrichment either at the element level, as in the strong discontinuity approach (SDA), or at the node level, as in the extended finite element method (XFEM). Here, two of the main intra-element fracture models will be explained, highlighting their advantages and/or potential drawbacks in the failure analysis.

1.1.1.6 XFEM

Recently, the cohesive crack approaches have been implemented in fracture models using alternative finite element frameworks, such as the well-known extended finite element method. The basic concept of the XFEM, is to enrich the approximation space so that it becomes capable of reproducing discontinuities such as cracks or interfaces. In contrast to PUFEM and other generalized FEMs, where the enrichments are usually employed on a global level and over the entire domain, the extended finite element method adopts the same procedure but at local level. Such a method uses the standard finite element mesh, but once the discontinuity takes place, a few degrees of freedom are added to the classic finite element model in selected nodes near to the discontinuity to provide a higher level of accuracy. In this way, the model is able to simulate arbitrary cracks, independently by the mesh, and crack propagation without remeshing procedure.

Considering a discretized domain with a discontinuity, the approximation $\mathbf{u}^h(\mathbf{x})$, used by the XFEM to calculate the displacement field for a point **x** locating within the domain, can be written as the sum of two terms: the classical displacement approximation term related to finite elements without the discontinuity $\mathbf{u}^{\mathrm{FE}}$, and the enriched approximation term for the cracked finite elements $\mathbf{u}^{\mathrm{enr}}$:

$$\mathbf{u}^h(\mathbf{x}) = \mathbf{u}^{\mathrm{FE}} + \mathbf{u}^{\mathrm{enr}} = \sum_{i \in I} N_i(\mathbf{x})\mathbf{u}_i + \sum_{m \in M} N_m(\mathbf{x})\phi(\mathbf{x})\mathbf{a}_m \tag{18}$$

where $\mathbf{u}_i$ is the vector of regular degrees of nodal freedom in the finite element method, and $\mathbf{a}_m$ is the set of degrees of freedom added to enrich the domain of interest. $N_i(\mathbf{x})$ are the classical iso-parametric finite element shape functions, and $\phi(\mathbf{x})$ the enrichment functions defined for the set of nodes included in the influence domain of the discontinuity. I and M are the node-set related to finite elements without the discontinuity and with the discontinuity, respectively. In a work of Moës and Belytschko [43], the additional term of the displacement approximation is further divided in two contributions, one related to the finite elements completely cut by the discontinuity and one that describes the approximation displacement field of the element containing the crack tip, thus obtaining the following enriched approximation:

$$\mathbf{u}^h(\mathbf{x}) = \sum_{i \in I} N_i(\mathbf{x})\mathbf{u}_i + \sum_{j \in J} N_j(\mathbf{x})H(f(\mathbf{x}))\mathbf{b}_j + \sum_{k \in K} N_k F(\mathbf{x})\mathbf{c}_k \tag{19}$$

where the Heaviside jump function $H(\cdot)$ is used to enrich the nodes of the elements cut into two parts by the crack. These nodes form the set *J* and are depicted with circles in Fig. 10.

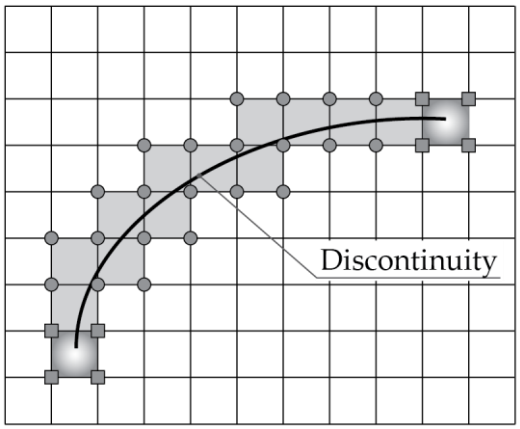

Fig. 10. Discontinuity within a structured mesh.

The function $f(\mathbf{x})$ is the signed distance function, that identifies the location of the point **x** with respect to the discontinuity, while $F(\mathbf{x})$ is the branch function used to model the displacement field in the elements containing the crack tip. $\mathbf{b}_j$ and $\mathbf{c}_k$, similar to the $\mathbf{a}_m$ in eq. 18, represent additional degrees of freedom to model the presence of the crack. The nodes around the tip of the discontinuity, depicted with squares in Fig. 10, form the set *K*, so that $J \cup K = M$. The most conventional form of branch functions, recently used in a cohesive crack model [44–46] and expressed in the local crack tip polar coordinate system, are defined as:

$$F(r,\theta) \equiv r\sin\left(\frac{\theta}{2}\right) \quad \text{or} \quad r^{3/2}\sin\left(\frac{\theta}{2}\right) \quad \text{or} \quad r^{2}\sin\left(\frac{\theta}{2}\right) \tag{20}$$

Introducing the XFEM approximation (Eq. 19) in the equilibrium equation, expressed by means of a weak form, we obtain the discrete variational principle weighted with a test function $\mathbf{v}$: find $\mathbf{u}^h \in \Re^h$ (with $\Re^h$ the discrete displacement space) so that:

$$\int_V \boldsymbol{\sigma}(\mathbf{u}^h) : \boldsymbol{\varepsilon}(\mathbf{v}) dV - \int_{S_{int}} \mathbf{t}(\mathbf{u}^h) \cdot \mathbf{w}(\mathbf{v}) dS = \int_{S_{ext}} \mathbf{F} \cdot \mathbf{v} dS \quad \forall \mathbf{v} \in \Re^h \tag{21}$$

where the integration over the volume V, involves the stress tensor $\boldsymbol{\sigma}$ and the function test of the deformation gradient $\boldsymbol{\varepsilon}$, while the integration over internal S_{int} and external S_{ext} surface involve the traction cohesive $\mathbf{t}$ and external load $\mathbf{F}$ vectors, respectively. The symbol $\mathbf{w}$ represents the displacement jump vector along the crack faces.

The fracture process in failure analysis, simulated by an intra-element cohesive model based on XFEM, develops on a discontinuity located in any zone of the discretized domain. Such a discontinuity is introduced in an element when a certain failure criterion is satisfied. Usually, when an equivalent stress exceeds the tensile strength of the material, the crack discontinuity is introduced as a straight line, and it is enforced to be geometrically continuous. The actual orientation of this discontinuity is determined by LEFM-based methods such as the principle of local symmetry [46] and the maximum hoop stress criterion [47]. The latter is the most used orientation criterion in this

type of analysis and defines the direction of propagation to be along a direction normal to the maximum hoop stress. The angle of crack growth θ is expressed in terms of the external stress intensity factors (SIFs) at the current tip through the formula:

$$\theta = 2\arctan\frac{1}{4}\left(\frac{K_I^{\text{ext}}}{K_{II}^{\text{ext}}} \pm \sqrt{\left(\frac{K_I^{\text{ext}}}{K_{II}^{\text{ext}}}\right)^2 + 8}\right) \tag{22}$$

where the sign is chosen so that the hoop stress is positive. The XFEM combined with the cohesive crack model has been widely used in the literature to simulate crack propagation in several homogeneous and heterogeneous materials. Recently, Gee and coauthors [48] have used a valid cohesive-zone XFEM model to predict the structural response, in terms of loading curve and crack path, of a thin rectangular PMMA specimen with an angled initial crack subjected to compression, resulting in a mixed-mode loading condition. The numerically predicted curved crack path is in an excellent agreement with that experimentally found throughout the entire loading history, thus showing the capability of the proposed model to capture, in a very realistic manner, all the main features of mixed-mode crack propagation (Fig. 11).

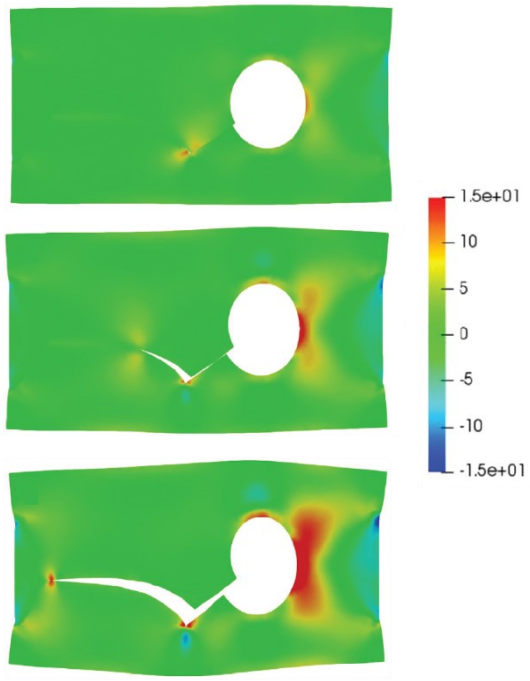

Fig. 11. Maximum principal stresses of deformed configurations at three different loading steps obtained by cohesive zone XFEM model [49].

The crack pattern has been well predicted by the intra-element fracture models also in concrete fracture analysis. Many numerical results, obtained by several authors [50–52] further confirm the accuracy of these models and demonstrate adequately the effectiveness of the combination of the

XFEM and the cohesive crack model in the crack growth simulation in concrete structures. Unlike the above-illustrated inter-element cohesive model, in which the crack is forced to propagate along the boundaries of the finite element, the intra-element approach, by virtue of the extended finite element scheme, is able to inject the discontinuity wherever this crack can be located with respect to the mesh. These models have been proved to provide more reliable numerical results, especially in the crack path predictions, but usually require a high implementation effort. As a matter of fact, the generalization of XFEM for arbitrary crack propagation problems also required implementation of tracking techniques, such as the level set method (LSM) and the fast marching method (FMM), to re-establish the geometric continuity of the crack line and for determining the location of crack tips [53,54].

1.1.1.7 Embedded cohesive crack model

A simple and successful intra-element cohesive model for the failure analysis of concrete and other quasi-brittle materials, is the embedded cohesive crack model elaborated by Sancho et al. [55]. Based on the well-known strong discontinuity approach (SDA) [56], in which the displacement jump caused by the geometric discontinuity is embedded in the corresponding finite element displacement field, such a fracture model simulates the crack initiation and propagation processes by means of a simple cohesive crack approach. The typical crack locking problems of the SDA approach, usually caused by the kinematical incompatibility between the cracks in the adjacent elements, are here circumvent by introducing a local crack adaptability algorithm, without resort to the well-known tracking procedures to re-establish the geometric continuity of the crack line [57,58].

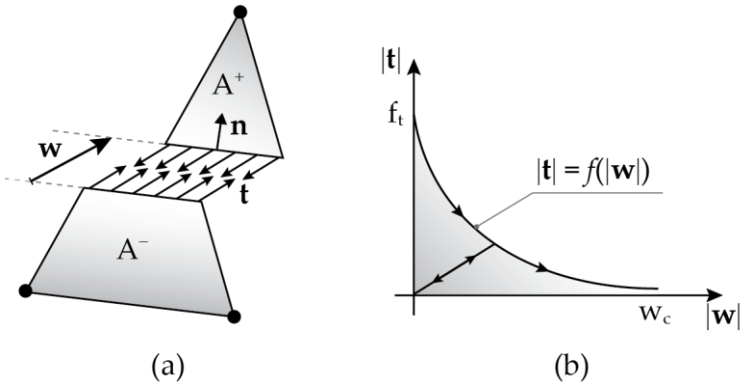

Fig. 12. Representation of the embedded crack model.

The basic concept of the embedded finite element formulation is that, once the principal stress reaches the tensile strength of the material, a straight crack, characterized by a displacement jump vector $\mathbf{w}$, is inserted in the element in the direction normal $\mathbf{n}$ to the maximum principal stress (Fig. 12(a)). Thus, the crack modifies the kinematics of the element and the new displacements field, can be written as follows:

$$\mathbf{u}(\mathbf{x}) = \sum_{\alpha \in A^- \cup A^+} N_\alpha(\mathbf{x})\mathbf{u}_\alpha + \left[H(\mathbf{x}) - \sum_{\alpha \in A^+} N_\alpha(\mathbf{x}) \right] \mathbf{w} \tag{23}$$

where N_α and $\mathbf{u}_\alpha$ are the shape function and nodal displacement associated to the node α, respectively. The Heaviside jump function $H(\mathbf{x})$ has a null value in the region A^- and a value of 1 in the region A^+. In a similar manner, the strain field in the continuum, denoted as ε^c, that determines the stress field of the element on both sides of the crack, is also modified, so that:

$$\varepsilon^c(x) = \underbrace{\sum_{\alpha \in A^- \cup A^+} \left[\mathbf{b}_\alpha(\mathbf{x}) \otimes \mathbf{u}_\alpha \right]^S}_{\varepsilon^a} - \left[\left(\sum_{\alpha \in A^+} \mathbf{b}_\alpha(\mathbf{x}) \right) \otimes \mathbf{w} \right]^S \tag{24}$$

where $\mathbf{b}_\alpha(\mathbf{x})$ is the gradient of the shape function associated to node α. The first summation, according to the finite element method theory, represents the apparent strain ε^a, i.e. the strain field without the discontinuity. The corresponding stress tensor in the element, which follows the hypothesis of elastic bulk material behavior, results to be:

$$\sigma(\mathbf{x}) = \mathbf{E} : \left[\varepsilon^a(\mathbf{x}) - \left[\mathbf{b}^+(\mathbf{x}) \otimes \mathbf{w} \right]^S \right] \tag{25}$$

where $\mathbf{E}$ is the tensor of the elastic moduli and $\mathbf{b}^+(\mathbf{x}) = \sum_{\alpha \in A^+} \mathbf{b}_\alpha(\mathbf{x})$. However, along the geometric discontinuity, the stresses are governed by a softening curve according to the adopted cohesive crack approach. This approach is based on a central forces model in which the traction vector $\mathbf{t}$, transmitted across the crack faces, is parallel to the crack displacement jump vector $\mathbf{w}$. The relation between the cohesive traction vector and displacement jump (Fig. 12(b)) is:

$$\mathbf{t} = f(\tilde{\mathbf{w}}) \frac{\mathbf{w}}{\tilde{\mathbf{w}}} \tag{26}$$

where the variable $\tilde{\mathbf{w}}$ represents the maximum value attained by the effective displacement jump over the entire loading history. Finally, by prescribing the equilibrium between the traction cohesive vector (eq. 26) and the stress tensor (eq. 25) projected in the normal direction $\mathbf{n}$, we obtain:

$$f(\tilde{\mathbf{w}}) \frac{\mathbf{w}}{\tilde{\mathbf{w}}} = \left(\mathbf{E} : \left[\varepsilon^a(\mathbf{x}) - \left[\mathbf{b}^+(\mathbf{x}) \otimes \mathbf{w} \right]^S \right] \right) \mathbf{n} \tag{27}$$

Once the stress reaches the strength of the material and a straight crack is introduced in the element perpendicular to the principal stress direction, $\mathbf{n}$ is computed as a unit eigenvector of the stress equation. After this, the corresponding vector $\mathbf{b}^+$ is obtained so that the angle between $\mathbf{b}^+$ and $\mathbf{n}$ is the smallest possible. In other words, the geometric discontinuity must be parallel to one of the sides of the triangular finite element.

In the literature, many fracture models based on SDA use crack tracking algorithms to re-establish the geometric continuity of the crack line across the elements. In this model, instead, in order to avoid

such types of numerical inconvenience during the simulations and possible crack locking, a simple method, based on a crack adaptability procedure within the element, is introduced. In particular, the model allows the geometric discontinuity to adapt itself to subsequent variations of the maximum principal stress direction until the effective displacement reaches the threshold value (Fig. 13).

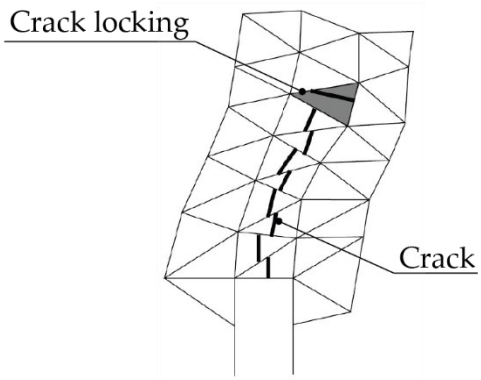

Fig. 13. Sketch of numerical crack-locking phenomena [59]

In this way the crack direction is recomputed at each step as if the crack were freshly created.

The embedded crack model is used by the authors for the failure analysis of plain concrete specimens subjected to mode-I and mixed-mode loading conditions [60]. The comparisons with experimental results have demonstrated the capability and versatility of the model to predict the global structural response and the crack pattern in an accurate manner without any additional complicated remeshing procedure (Fig. 14).

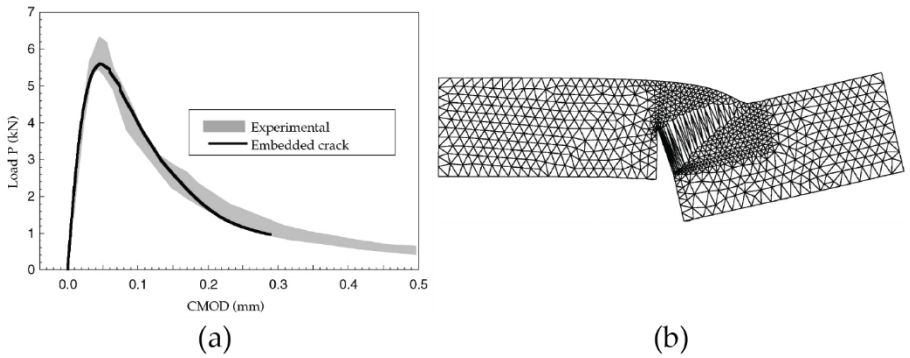

(a) (b)

Fig. 14. Numerical results obtained by the embedded crack model in [59]: loading curve (a) and deformed mesh (b).

In particular, the above-discussed model is able to predict a smoother crack path compared to that jagged obtained by inter-element cohesive models, consequently obtaining a loading curve more consistent with the experimental data. Additionally, from a computational point of view, the embedded strong discontinuity model proposed by Sancho et al. does not require a great implementation effort, unlike the X-FEM technique and other sophisticated intra-element approaches.

However, the model would to be tested in more complicated fracture cases, where multiple cracking, crack branching phenomena, and/or coalescence between cracks occur.

1.1.2 Smeared crack model

In contrast to discrete fracture models, in which cracks are modeled as geometric discontinuities, smeared crack models, used almost exclusively in the design practice and that have obtained wide popularity in the finite element analysis, simulate damage processes as a progressive loss of the material integrity due to the propagation and coalescence of micro-cracks and micro-voids [61]. The smeared crack models [62–64] consider constitutive relations in which the mechanical effect of the cracking and void growth is introduced with internal state variables which act on the degradation of the elastic stiffness of the material and involve strain softening in order to describes the post-peak gradual decline of stress at increasing strain. Such models can be relatively simple, as the isotropic damage models [65–67] or more complex as the anisotropic ones [68–70]. However, these models usually adopt different regularization techniques able to prevent the well-known ill-posedness of the associated BVPs, such as those based on strain gradient and micropolar [39] formulations [66,71].

1.1.2.1 Continuum damage mechanics

To introduce the basic concepts of the continuum damage mechanics, we analyze the mechanical behavior of a material idealized as set of perfectly brittle strips parallel to the loading direction, as depicted in the following figure.

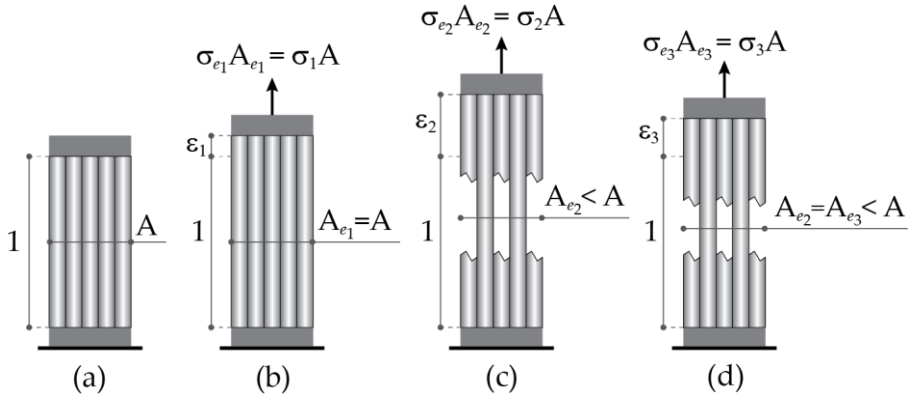

Fig. 15. Schematic representation of a uniaxial damage model as a bundle of parallel perfectly brittle strips breaking at different strain levels.

Initially, all the strips respond elastically, and the entire section maintains the applied load (Fig. 15(b)). As the load increases some strips start breaking (Fig. 15(c)) and the *effective area* A_e, that is the area of the unbroke strips that can still carry stress, gradually decreases. Now, it is possible to distinguish a nominal stress σ, defined as the force of unit initial area of the cross section, and an *effective stress* σ_e related to the unit effective area. By the equivalence condition $\sigma A = \sigma_e A_e$ we obtain:

$$\sigma = \frac{A_e}{A}\sigma_e \tag{28}$$

in which the ratio A_e / A is a scalar that characterize the integrity of material used in the damage mechanics to define the so-called *damage variable* as follows:

$$D = 1 - \frac{A_e}{A} = \frac{A - A_e}{A} = \frac{A_d}{A} \tag{29}$$

with A_d the damaged area. Therefore, for an intact material, i.e. $A_e = A$, the damage variable is equal to $D = 0$, contrariwise during the degradation process due to the micro-defects propagation, the damage variable asymptotically approaches to the limit value $D = 1$.

Consequently, the nominal stress, governed by Hooke's law, can be expressed as:

$$\sigma = (1 - D)E\varepsilon \tag{30}$$

and the damage process is characterized by the dependence of the D on the applied strain as:

$$D = g(\varepsilon) \tag{31}$$

with g a function that describe the stress-strain curve and can be directly identified from a uniaxial tensile test. In the case represented in Fig. 15(d) when the material is first stretched up to a strain level ε_2, inducing a damage $D_2 = g(\varepsilon_2)$ and then a strain decrease occurs until ε_3, the damage area remain constant but the material respond elastically with a reduction of Young's modulus $E_2 = (1 - D_2)E$. In this case, during the unloading and reloading condition, the damage variable must be evaluated from the largest previously reached strain:

$$\kappa = \max_{History}(\varepsilon) \tag{32}$$

and the damage evolution law is then replaced by equation:

$$D = g(\kappa) \tag{33}$$

Now, we can introduce a new function $f(\varepsilon, \kappa) = \varepsilon - \kappa$ and the loading-unloading conditions can be expressed in the Kuhn-Tucker form as follows:

$$f \le 0, \quad \dot{\kappa} \ge 0, \quad \dot{\kappa} f = 0 \tag{34}$$

in which it is imposed that κ can never be smaller than ε, κ cannot decrease and can increase only if the current values of ε and κ are equal. Therefore, $f = 0$ and $\dot{\kappa} > 0$ during damage growth, $f < 0$ and $\dot{\kappa} = 0$ during unloading condition.

The above-explained uniaxial damage test can be extended to general multiaxial stress states by means of an isotropic damage model with a single scalar variable. The fundamental assumptions of

the isotropic model are: (i) stiffness degradation is isotropic, i.e. the stiffness moduli, corresponding to different directions, decrease proportionally independently of the loading direction; (ii) the Poisson's ratio is not affected by the damage, i.e., the relative reduction of all stiffness coefficients is the same. Consequently, the damage stiffness tensor is expressed as:

$$\boldsymbol{E}_s = (1-D)\boldsymbol{E} \tag{35}$$

where $\boldsymbol{E}$ is the elastic stiffness tensor of the intact material and $\boldsymbol{E}_s$ is the secant stiffness that relates the total strain to the total stress, according to the formula:

$$\boldsymbol{\sigma} = \boldsymbol{E}_s\varepsilon = (1-D)\boldsymbol{E}\varepsilon \tag{36}$$

Finally, the effective stress tensor is defined as:

$$\boldsymbol{\sigma}_e = \boldsymbol{E}\varepsilon \tag{37}$$

and the total multidimensional stress can alternatively be written as:

$$\boldsymbol{\sigma} = (1-D)\boldsymbol{\sigma}_e \tag{38}$$

As in the uniaxial stress test, we there introduce a loading function f depending on the strain tensor ε, and on a variable κ that controls the evolution of the elastic domains. A state for which $f(\varepsilon,\kappa) < 0$ is supposed to be below of the critical damage level. Then, a generalization of Kuhn-Tucker form for the unloading condition can be written as:

$$f(\varepsilon,\kappa) = \tilde{\varepsilon}(\varepsilon) - \kappa \tag{39}$$

where the $\tilde{\varepsilon}$ is a scalar measure of the strain level called *equivalent strain*. This damage loading function, similar to the yield function in plasticity, does not depend on σ_e and describe the shape of elastic domains. For instance, a customary definition of equivalent strain for materials as metals is the Euclidean norm of the strain tensor.

1.2 Multiscale modelling of fracture

As is widely known, fracture and failure in heterogeneous materials are inherently multiscale phenomena since the processes that are triggered at the microscopic scale (e.g. damage initiation due to defects or voids) evolve at the macroscopic scale (e.g. formation of cracks or appearance of areas with localized deformation) and influence and determine the overall properties of the materials and the global behavior of the structure. The most suitable and most widely used tools for studying the response of heterogeneous materials are those provided by *multiscale* models. Such models are capable of considering the interaction that takes place between the various phenomena at different scales and are therefore very effective for the accurate analysis of strongly heterogeneous structures and materials.

Multiscale models are also able to overcome some of the shortcomings of purely macroscopic models, such as the lack of the possibility of explicitly incorporating the numerous microscopic damage mechanisms of the material, and some of the limitations of purely microscopic models, such as the high computational cost. In fact, in the context of microscopic modelling (e.g. using the finite element method), the smallest dimension of the elements used for the discretization of the domain cannot be larger than the smallest of the defects present in the microstructure. This, therefore, leads to too complex models and too costly analyses, with reference to the calculation tools currently available.

The use of multiscale methods therefore combines the advantages of microscopic models (excellent accuracy) and macroscopic models (good computational efficiency) at the same time. To this end, it is crucial to describe the micromechanical behavior of materials in the presence of damage and nonlinear phenomena. The most commonly used models, which are also incorporated in more general and complex multiscale approaches, are homogenization models. Within these models, it is then possible to predict the overall mechanical properties of the materials by establishing relationships between micro variables (strain and stress at the microscopic levels) and their macroscopic counterparts.

Since the homogenized properties must be representative of the whole microscopic heterogeneities, any homogenization technique requires the definition of a specific volume on which these properties are assumed to be known, i.e. a *Representative Volume Element* (RVE) or a *Repeating Unit Cell* (RUC), the latter concept being strictly valid for heterogeneous media with periodic microstructure.

Different definitions of RVE have been introduced in the technical literature [1,72–76], but, according to the description provided by Hill [77] the RVE is "*a sample that (a) is structurally entirely typical of the whole mixture on average, and (b) contains a sufficient number of inclusions for the*

apparent overall moduli to be independent of the surface values of traction and displacement, so long as these values are macroscopically uniform".

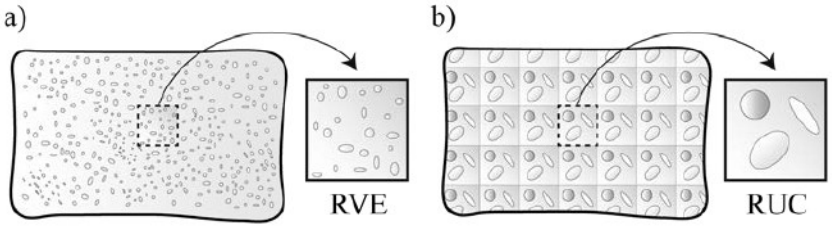

Fig. 16. Geometric representation of solid microstructures adopted in micromechanical analyses: statistically representative sample characterized by an RVE (a) and periodic samples characterized by an RUC (b).

In order to rigorously quantify the dimensions of an RVE, three different types of scale must be defined: the first is the scale of the continuum, known as macro-scale and defined as L_{macro}, by which the infinitesimal surroundings of the material point can be measured; the second scale, on the other hand, is the so-called micro-scale L_{micro}, which corresponds to the smallest micro-constituent within the microstructure, whose properties are assumed to have a direct influence on the global properties of the macro-element; the last one, referred to as mesoscale, it the intermediate scale denoted by L_{RVE}, corresponding to the size of the Representative Volume Element. The following inequalities link these three different scales, according to the principle of scale separation introduced by [78]:

$$L_{\text{micro}} \ll L_{\text{RVE}} \ll L_{\text{macro}} \tag{40}$$

1.2.1 Theoretical formulation of the homogenization problem

Under the assumption of small displacements and quasistatic loading, let us consider the representative volume element (RVE) depicted in Fig. 17, whose domain is associated with an infinitesimal neighborhood of a material point $\bar{\boldsymbol{x}}$ of the homogenized continuum and is formed by a solid portion S and a hole portion H that includes microscopic discontinuities like cracks and interface debonding:

$$V = S \cup H \tag{41}$$

The boundary of the hole ∂H represents the union of micro-void and micro-crack surfaces. Let $\boldsymbol{u}(\boldsymbol{x})$ and $\boldsymbol{\varepsilon}(\boldsymbol{u}(\boldsymbol{x}))$ be the microscopic displacement and strain field of the micro-structure at the material point $\boldsymbol{x}$ of the microstructure, respectively. Tractions can be applied on the surface ∂V of the RVE, and the microscopic traction field is assumed to vanish on the surfaces of holes and cracks in the interior of the RVE $\boldsymbol{t}=\boldsymbol{0}$ on ∂H.

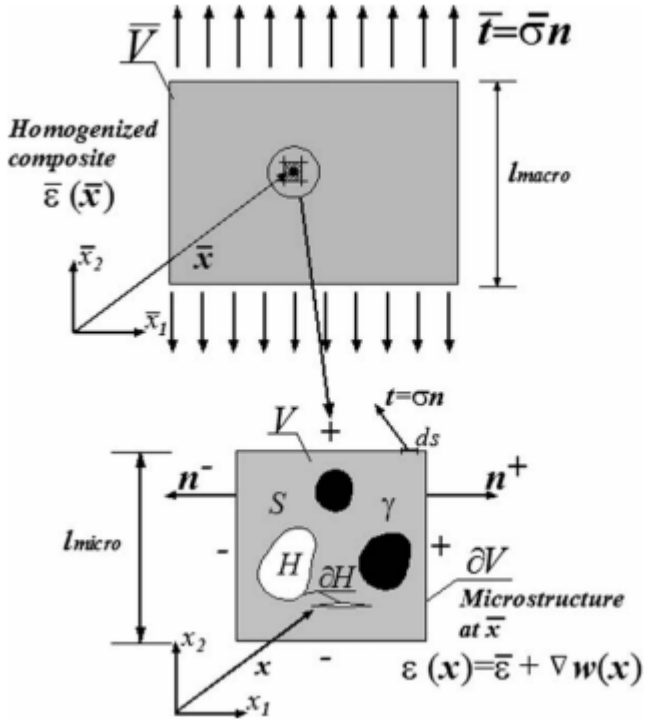

Fig. 17. Representative volume element of a heterogeneous microstructure containing micro-cavities, micro-cracks, and inclusions, associated with an infinitesimal neighborhood of a material point [79].

As a consequence of the principle of scale separation previously introduced, the macroscopic constitutive response of the micro-structure is based on an equilibrium state neglecting volume forces, implying that the local stress field is divergence-free, $\mathrm{Div}(\boldsymbol{\sigma})=\boldsymbol{0}$ in S.

The macroscopic stress and strain fields are defined as:

$$\bar{\boldsymbol{\sigma}}=\frac{1}{|V|}\int_{\partial V}\boldsymbol{t}\otimes\boldsymbol{x}dA,\quad \bar{\boldsymbol{\varepsilon}}=\frac{1}{|V|}\int_{\partial V}\boldsymbol{u}\otimes_s\boldsymbol{n}dA \tag{42}$$

where $\otimes_s$ is the symmetric part of the tensor product $\otimes$ and $\boldsymbol{n}$ is the outward normal at $\boldsymbol{x}\in\partial V$. It is important to note that the volume average over V for the macrostrain field is valid only for micro-structures without discontinuities and holes. Indeed, the general definition of the macroscopic strain field is the following:

$$\bar{\boldsymbol{\varepsilon}}=\frac{1}{|V|}\int_{S}\boldsymbol{\varepsilon}dV+\frac{1}{|V|}\int_{\partial H}\boldsymbol{u}\otimes_s\boldsymbol{n}dA \tag{43}$$

where $\boldsymbol{n}$ is the outward normal at $\boldsymbol{x}\in\partial H$. By virtue of the previous equations, the microscopic displacement and strain fields are defined as:

$$\boldsymbol{u}(\boldsymbol{x})=\bar{\boldsymbol{\varepsilon}}\boldsymbol{x}+\boldsymbol{w}(\boldsymbol{x}),\quad \boldsymbol{\varepsilon}(\boldsymbol{x})=\bar{\boldsymbol{\varepsilon}}+\nabla_s\boldsymbol{w} \tag{44}$$

We can see that the microscopic displacement field is defined as a function of the macroscopic strain $\bar{\boldsymbol{\varepsilon}}$, expressed as the sum of the part related to the homogeneous deformation $\bar{\boldsymbol{\varepsilon}}\boldsymbol{x}$, and the

correction part refers to a non-homogenous deformation $\boldsymbol{w}(\boldsymbol{x})$. In equation 44 ∇_s is the symmetric part of the gradient with respect to $\boldsymbol{x}$.

1.2.2 Admissible kinematic boundary conditions

The linear part of the displacement field of the microstructure, represented by in equation 44, would be the actual displacement field if the deformation was homogeneous and therefore represents the fluctuation of the microscopic displacement $\boldsymbol{u}(\boldsymbol{x})$ about that linear part, and it is known as the fluctuation field. The constraint in terms of this fluctuation field, by virtue of the application of equation 42, conducts to:

$$\frac{1}{|V|}\int_{\partial V} \boldsymbol{w}\otimes_s \boldsymbol{n}dA=\boldsymbol{0} \tag{45}$$

The three boundary conditions that satisfy the above equation are:

- Linear displacements $\boldsymbol{w}=\boldsymbol{0}$, which implies homogenous deformation on the boundary;
- Periodic fluctuations $\boldsymbol{w}(\boldsymbol{x}^+)=\boldsymbol{w}(\boldsymbol{x}^-)$, mean that all the components of $\boldsymbol{w}(\boldsymbol{x})$ are identical on the opposite sides of the boundary;
- Uniform tractions $\boldsymbol{t}=\bar{\boldsymbol{\sigma}}\boldsymbol{n}$.

Fig. 18 reports the schematic representation of the three boundary conditions here described.

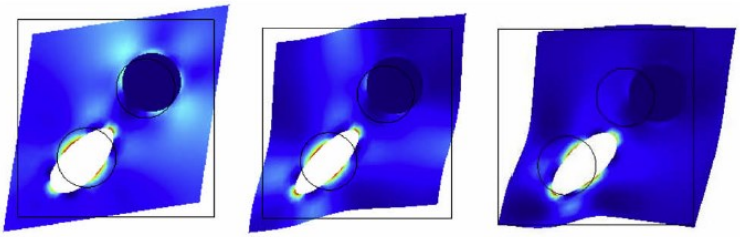

Fig. 18. Representation of the three boundary conditions: 1) linear displacements; 2) periodic fluctuations; 3) uniform tractions [79].

1.2.3 Overview of multiscale methods

According to the taxonomy of multiscale methods [80] there are three different classes of multiscale modeling approaches:

- Hierarchical multiscale methods;
- Concurrent multiscale methods;
- Semi-concurrent multiscale methods.

As inferred from the technical literature (see [81] and reference therein), the first are known as classical non-linear homogenization approaches, in which only one-way coupling between micro- and macro-scales is defined. They are computationally efficient but not suitable for handling strain localization, unless special scale transition schemes are used.

The concurrent methods are characterized by the presence of a fine-scale embedded into the coarse-scale model, which is directly and strongly coupled to it. The main advantages are that they do not require periodicity assumptions for regions undergoing damage and the strain localization and boundary effects can be accounted for in a unified manner. On the other hand, they exhibit a high computational cost in the presence of diffuse damage.

The semi-concurrent methods, based on a two-way weak coupling between micro- and macro-scales, are more accurate for strongly nonlinear problems, but they are not suitable for studying the coalescence of several micro-cracks into a single macro-crack. To overcome these drawbacks, more advanced approaches have been proposed including higher-order [82], coupled volume [83], micropolar [84,85], and continuous/discontinuous homogenization [73,86–89].

1.2.3.1 Hierarchical methods

The hierarchical multiscale methods, also known as unit cell methods, are able to develop the so-called micromechanically informative constitutive models that can be used in structural computations. This makes them particularly appropriate for studying the behavior of composite materials.

In hierarchical models, the following step must be performed:

- Identification of the representative volume element (RVE) or the repeating unit cell (RUC);
- Definition of the microscopic boundary conditions;
- Computation of the output macroscopic variable from the results of the microscopic boundary value problem associated with the RVE (micro-to-macro transition of homogenization);
- Determination of the numerical constitutive law, relating each other the input and the output macroscopic variables.

1.2.3.2 Concurrent methods

The main feature of concurrent multiscale methods consists in embedding a microscopic model into the macroscopic one, leading to a strong coupling between different length scales; thus, two main issues must be addressed in the practical application of these methods:

- suitable handling the coupling between the fine-scale and the coarse-scale models;
- finding efficient strategies for adding adaptivity during the fine-scale additions to the principal model, in order to reduce the computational costs.

Several concurrent methods have been proposed, based on different theoretical approaches and numerical strategies. According to the length scales involved in the considered physical problem, different choices can be made about the nature of the fine-scale models: on one hand, the microscopic model can be a discrete (molecular or atomistic) model, as in the macroscopic-atomistic-ab initio dynamics (MAAD) approach [90], the quasi-continuum (QC) method [91], the atomistic-to-continuum (AtC) coupling technique [92], and the bridging domain method [93]; on the other hand, the fine-scale model can be described as a continuum [94–96]. Concurrent multiscale methods can be regarded as falling within the class of domain decomposition methods (DDMs), since the numerical model describing the composite structure is decomposed into a fine and coarse-scale sub-models, which are simultaneously solved, thus establishing a strong "two-way" coupling between different resolutions. In classical domain decomposition methods, the computational domain is divided into smaller subdomains to be simultaneously solved, and a computational strategy is required to make sure that the solutions on different subdomains match each other. Most of concurrent multiscale methods can be classified in overlapping and non-overlapping methods.

In most multiscale models, two or more continuum models are strongly coupled to each other, allowing us to perform accurate simulations at the microscopic scale within the so-called zone of interest, which is usually adaptively updated during calculations. A heterogeneous multiscale model consisting of several subdomains describing the material at different length scales is considered. Mesoscale models, characterized by a nonlinear material behavior, are only used in those zones of the structure in which damage or instabilities take place; on the contrary, undamaged regions of the structure are simulated at the macroscale assuming a linear elastic material behavior characterized by effective material parameters. Such an approach combines the advantages of both scales, i.e. the numerical efficiency of macroscale models and the accuracy of microscale models. Moreover, concurrent multiscale methods are able to deal with boundary layer effects in a natural way, by replacing the coarse-scale model with a fine-scale one where periodicity conditions are no longer valid, as in the vicinity of free edges or applied loads or constraints.

The critical aspect of the concurrent multiscale methods is denoted by the connection between critical and the noncritical domains. Hence, to connect subdomains with nonmatching finite element

discretization, two alternative methods are commonly adopted. The first one, known as collocation method, is based on the enforcing the displacement compatibility in a strong sense, i.e.

$$\boldsymbol{u}_M(\boldsymbol{x})-\boldsymbol{u}_m(\boldsymbol{x})=\boldsymbol{0} \qquad \forall \boldsymbol{x}\in\Gamma_c=\Omega_M\cap\Omega_m \tag{46}$$

where $\boldsymbol{u}_M$ and $\boldsymbol{u}_m$ are the displacements of the subdomains Ω_M and Ω_m, respectively.

The second one, known as the mortar method [97], is based on the enforcing the coupling condition in a weak way. Hence, equation 46 is only satisfied in an average sense:

$$\int_{\Gamma_c}(\boldsymbol{u}_M(\boldsymbol{x})-\boldsymbol{u}_m(\boldsymbol{x}))d\boldsymbol{x}=\boldsymbol{0} \qquad \Gamma_c=\Omega_M\cap\Omega_m \tag{47}$$

1.2.3.3 Semiconcurrent methods

When dealing with microscopic nonlinear phenomena a “two-way” coupling between micro- and macrovariables is required, i.e. the homogenized properties have to be updated during the microstructural evolution. In semiconcurrent multiscale methods, also referred to as computational homogenization methods, the macroscopic constitutive response of a heterogeneous material is determined “on the fly” during simulation; these methods have been widely used to predict the mechanical behavior of microstructured materials, due to their flexibility. The most important approaches are those proposed by Guedes and Kikuchi [98], Miehe et al. [8], Kouznetsova et al.[99], and Feyel and Chaboche [100].

The last one, known as multilevel finite element (FE^2) method, has been a reference work for the scientific community and inspired a lot of works from other researchers. The key idea of such approaches is to associate a microscopic boundary value problem to each integration point of the macroscopic boundary value problem, after discretizing the underlying microstructure. The macroscopic strain provides the boundary data for each microscopic problem (macro-to-micro transition or localization step). The set of all microscale problems is then solved, and the results are passed back to the macroscopic problem in terms of overall stress field and tangent operator (micro-to-macro transition or homogenization step). Localization and homogenization steps are carried out within an incremental-iterative nested solution scheme; thus, the two-scale coupling remains of a weak type. An advantage of semiconcurrent methods over hierarchical methods is that a framework for storing the macroscopic constitutive response is not needed.

In the original formulation of the method, based on a classical first-order homogenization, the large spatial gradients in macroscopic fields cannot be resolved due to the supposed validity of the principle of scale separation, therefore they are not suited for studying strain localization phenomena which commonly affect the macroscopic behavior of composites; moreover, softening behaviors cannot be properly analyzed because of the mesh dependence at the macroscopic scale due to the ill-posedness of the macroscopic boundary value problem, as shown in [72].

In order to overcome such limitations, other homogenization paradigms have been proposed in the literature, such as the higher-order computational homogenization schemes and the coupled volume multiscale method in sections 1.2.3.4 and 1.2.3.5, respectively.

The FE^2 method has been introduced in [100] and consists of describing the mechanical behavior of heterogeneous structures. After choosing two relevant mechanical scales (referred to as microscale and macroscale), the FE^2 method can be adopted, based on three main ingredients:

i. The identification of a representative volume element (RVE);

ii. A localization rule able to obtain the local solution inside the RVE, for any given macroscopic strain;

iii. A homogenization rule giving the macroscopic stress tensor, starting from the micromechanical stress state.

In this setting, macroscopic phenomenological relationships are not required, even in the case of nonlinear behaviors; indeed, the macroscopic response arises directly from the calculation at the microscopic level.

The FE^2 method is applied by means of a nested solution scheme sketched in Fig. 19; for each step of the macroscopic incremental iterative procedure, and for each macroscopic integration point, the macroscopic strain $\bar{\boldsymbol{\varepsilon}}$ is computed based on the current (iterative) macroscopic displacement field.

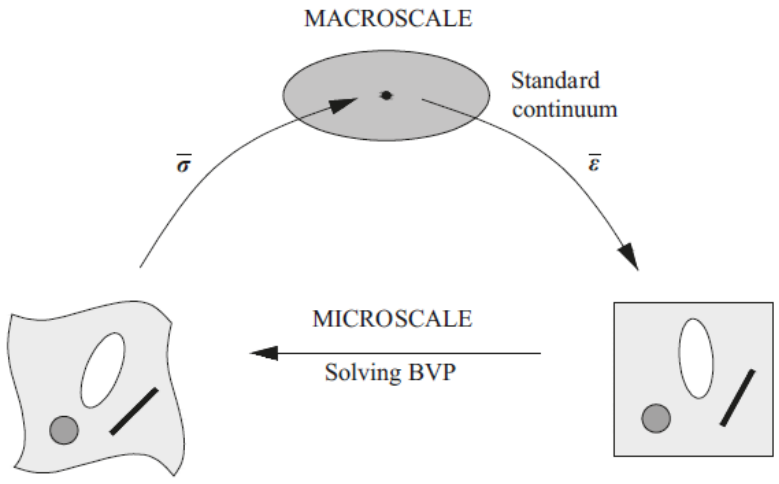

Fig. 19. First-order computational homogenization scheme.

Then, $\bar{\boldsymbol{\varepsilon}}$ is passed to the microscopic level and used to define the boundary conditions to be applied to the RVE attached to the respective macroscopic integration point. After solving every RVE problem, the macroscopic stress tensor $\bar{\boldsymbol{\sigma}}$ is obtained in a post-processing step. Thus, the macroscopic equilibrium can be evaluated, and the next iterations are performed until equilibrium is achieved; after this, the calculations can be continued for the next load increment.

The multilevel finite element method is intrinsically parallel; indeed, all RVE calculations for one macroscopic iteration can be performed simultaneously without any exchange of information between them. Thus, even if this method is computationally costly, the use of parallel processors for the RVE analyses would significantly reduce the total calculation time.

1.2.3.4 Higher-order computational homogenization

In this section the second-order computational scheme, proposed by Kouznetsova et al. [101] to extend the classical computational techniques, is illustrated. This technique adopts not only the macrostrain tensor (as in first-order schemes) but also its gradient to prescribe the essential boundary conditions on the representative volume element of the given microstructure, leading to a second-order continuum macroscopic model.

For each step of the macroscopic incremental-iterative procedure, and for each macroscopic integration point, the macroscopic deformation gradient tensor and its gradient are computed based on the current (iterative) macroscopic displacement field. Then, these macroscopic quantities are passed to the microscopic level and used to define the boundary conditions to be applied to the RVE attached to the respective macroscopic integration point. After solving every RVE problem, the macroscopic stress tensor and the higher-order stress tensor are obtained. Thus, the macroscopic internal nodal forces can be computed, the higher-order equilibrium can be evaluated, and the next iterations are performed until equilibrium is achieved; after this, the calculations can be continued for the next load increment.

The inclusion of strain gradients and higher-order stresses automatically results in the introduction of a length scale parameter in the macroscopic response; this allows to overcome the dependence on the macroscopic discretization but does not solve the RVE size dependence in the case of softening behaviors, as shown in [72].

1.2.3.5 Coupled volume multiscale method

A different approach has been proposed by Gitman et al. [72], referred to as the coupled volume multiscale method, able to resolve simultaneously the macroscale discretization sensitivity and the RVE size dependence. The main feature of this method is that an RVE is not linked to an infinitely small macroscopic material point, but associated with a macro-element whose size equals the RVE size.

The coupled volume approach abandons the principle of scale separation, and a model parameter (the RVE size) is linked to a numerical parameter (the mesh size); since this approach does not rely upon the existence of an RVE, it can also be used in the presence of softening behaviors. By linking the mesh size to the RVE size, the macroscopic mesh dependence is balanced by different constitutive

behaviors arising from different RVE sizes; as a consequence, the macroscopic response shows neither macroscopic mesh dependency nor RVE size dependency.

1.2.3.6 Continuous/discontinuous computational homogenization

Continuous-discontinuous homogenization methods refer to computational homogenization models in which the bulk and discontinuities at the macroscale are coupled to RVE problems. These approaches arise directly from the discontinuous homogenization schemes, developed in the context of computational homogenization to obtain the behavior of cracks at the macroscopic level from nested microscale computations performed on a sample representing the fully resolved microstructure of a thin layer.

Homogenization towards intrinsic cohesive laws has been introduced by Matouš et al. [102], where microscopic failure is described by a continuum damage model; a similar work has been presented by Alfaro et al. [103], where microscopic failure is modeled by using discrete cohesive microcracks.

On the other hand, homogenization towards extrinsic cohesive laws has been adopted by Verhoosel et al. [88] and Nguyen et al. [89], to model random heterogeneous materials exhibiting discrete cracking and band localization, respectively.

The main scope of continuous-discontinuous homogenization approaches consists in performing the transition from diffusive microcracks to localized macrocracks as usually observed; generally speaking, a macrocrack is injected at the macrocontinuum point associated with a certain representative volume element (RVE), when a material instability (a crack and/or a shear band) is detected within this RVE.

One of the first computational homogenization models able to deal with strain localization problems is that by Massart et al. [86] in the context of masonry cracking; other approaches have been proposed by Belytschko et al. [87] for composite materials, by Souza and Allen [104] for random viscoelastic materials, and by Nguyen et al. [105] for random heterogeneous solids. These approaches share some common features, but they differ in the description of failure at both the microscopic and macroscopic scales: in [86] localization bands are used to model microscopic failure, whereas embedded crack bands are employed to describe macroscopic failure; in [104] both microscopic and macroscopic failure is simulated by using cohesive zone models; in [106] macroscopic failure is described by traction-free cracks, whereas one cohesive crack is used to model microscopic failure; in [105] cohesive zone models are used to describe macroscopic failure, whereas for the microscopic failure a diffuse localization band is employed.

2. A diffuse interface model for the failure analysis of heterogeneous materials and structures

This chapter contains a detailed description of the proposed diffuse cohesive interface model, as well as details and specific formulations for the application of the model to different heterogeneous materials involved in several case studies.

In particular, in the first section, the theoretical formulation of the model is given regarding the case of planar elasticity. Subsequently, the different formulations proposed for the numerical applications will be presented, with a particular focus on the incorporation of the concrete plasticity and the friction effects in the cohesive law. Furthermore, the proposed model is employed to describe the bond behavior between the concrete and nano-enhanced reinforcement system.

Moreover, in the last part of this chapter, the embedded truss model and the single interface model will be briefly recalled. They will be implemented in the finite element framework for the interaction between concrete and steel reinforcement and for the analysis of the debonding phenomena between FRP reinforcements and concrete substrates, respectively.

2.1 Theoretical background of the adopted diffuse interface method

2.1.1 Variational formulation

The theoretical approach of the adopted crack model relies on a variational formulation written for a discretized solid consisting of linearly elastic bulk elements, representing the undamaged phase, and zero-thickness interface cohesive elements representing the only nonlinearity source of the adopted fracture approach. In particular, considering a cracked body $\Omega \in \mathbb{R}^2$ with a geometric discontinuity Γ_d, subjected to surface forces $\bar{\boldsymbol{p}}$ and prescribed displacement $\bar{\boldsymbol{u}}$ on its Newman Γ_{N} and Dirichlet Γ_{R} boundaries, respectively, and volume forces $\bar{\boldsymbol{f}}$, the associated BVP is expressed in the following weak form: find $\boldsymbol{u} \in U$ such that:

$$\int_{\Omega \setminus \Gamma_d} \boldsymbol{C}\boldsymbol{\varepsilon}(\boldsymbol{u}) \cdot \boldsymbol{\varepsilon}(\delta \boldsymbol{u}) \, \mathrm{d}\Omega + \int_{\Gamma_d} \boldsymbol{t}_{coh}(\boldsymbol{u}) \cdot \delta \boldsymbol{u} \, \mathrm{d}\Gamma - \int_{\Omega \setminus \Gamma_d} \bar{\boldsymbol{f}} \cdot \delta \boldsymbol{u} \, \mathrm{d}\Omega - \int_{\Gamma_{\mathrm{N}}} \bar{\boldsymbol{p}} \cdot \delta \boldsymbol{u} \, \mathrm{d}\Gamma = 0 \quad \forall \delta \boldsymbol{u} \in \delta U \quad (48)$$

where $\boldsymbol{u}$ and $\delta \boldsymbol{u}$ are the unknown displacement field and the arbitrary virtual displacement, respectively, belonging to the set of kinematically admissible displacement and variations U and δU, respectively. The second term of Eq. 48 represents the virtual work of the cohesive tractions $\boldsymbol{t}_{coh}(\boldsymbol{u})$ acting along the discontinuity Γ_d and $\boldsymbol{u}$ the displacement jump between the two crack faces. The mechanical behavior of these cohesive tractions for monotonic and cyclic tensile loads, i.e., without sign inversion of the normal stresses, is described by a traction-separation law of the kind $\boldsymbol{t}_{coh} = (1-D)\boldsymbol{K}^0 \boldsymbol{u}$, depending on an isotropic scalar damage variable D with exponential evolution [107]:

$$D=\begin{cases}0 & \text{for } \delta_m^{\max}\le\delta_m^0\\ 1-\dfrac{\delta_m^0}{\delta_m^{\max}}\left\{1-\dfrac{1-\exp\left[-\alpha\left(\dfrac{\delta_m^{\max}-\delta_m^0}{\delta_m^f-\delta_m^0}\right)\right]}{1-\exp(-\alpha)}\right\} & \text{for } \delta_m^0<\delta_m^{\max}\le\delta_m^f\\ 1 & \delta_m^f<\delta_m^{\max}\end{cases} \tag{49}$$

That involves the effective displacement jump $\delta_m=\sqrt{\langle\delta_n\rangle^2+\delta_s^2}$, with δ_n and δ_s, being the normal and tangential components of the displacement jump vector $\boldsymbol{u}$. The superscript $\max$ refers to the maximum value recorded over the entire deformation history attained by the considered quantity; δ_m^0 and δ_m^f are the effective displacement jumps at the onset and total decohesion, respectively; and the symbol α is a dimensionless material parameter influencing the rate of damage evolution and set equal to 5 for quasi-brittle materials [108]. A schematic representation of the cohesive crack model with related notations and the adopted cohesive law is reported in the following figure.

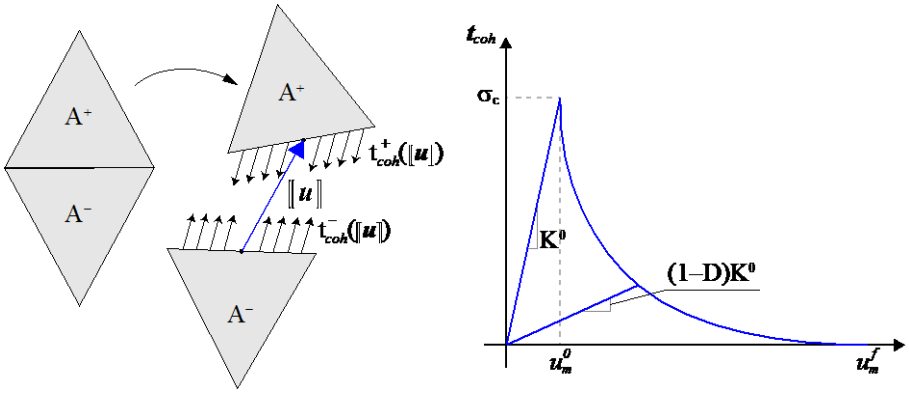

Fig. 20. Schematic representation of the cohesive/volumetric FE approach together with the adopted traction-separation law for the cohesive interface elements.

The expression of δ_m^0 and δ_m^f [109] are obtained by the following mixed-mode crack initiation and propagation criteria:

$$\left(\frac{\langle t_{coh,n}\rangle}{\sigma_c}\right)^2+\left(\frac{\langle t_{coh,s}\rangle}{\tau_c}\right)^2=1\,,\quad \frac{G_I}{G_{Ic}}+\frac{G_{II}}{G_{IIc}}=1 \tag{50}$$

where σ_c and τ_c are the normal and tangential material strengths, respectively, while G_I and G_{II} are the mode-I and -II energy release components, respectively, with the subscript c denoting the critical values of the considered quantities. It is worth noting that the initial stiffness $\boldsymbol{K}^0$ of cohesive elements plays an important role as a penalty parameter (without having a precise physical meaning) and must be suitably set to enforce the inter-element continuity. The stiffness parameters have been calibrated by a micromechanics-based calibration criterion [109], which involves dimensionless

parameters κ and ξ obtained by an elastic homogenization procedure, leading to the following relationship:

$$K_n^0 = \kappa \frac{E'}{L_{mesh}} , \quad K_s^0 = \xi K_n^0 \tag{51}$$

where E' is the reduced Young's modulus of the material, being equal to E or $E/(1+\nu^2)$ for plane stress or plane strain conditions, while L_{mesh} is the average size of the computational mesh.

2.1.2 An improved numerical formulation for loading/unloading processes

In order to analyze the damage phenomena in structures subjected to cyclic loading conditions, an accurate numerical formulation that incorporates concrete damage plasticity is necessary. Such a behavior is taken into account by introducing normal δ_n^p and tangential δ_s^p plastic contributions, in the normal δ_n and tangential δ_s components of the displacement jump $\boldsymbol{u}$ as follows:

$$\begin{bmatrix} \delta_n \\ \delta_s \end{bmatrix} = \begin{bmatrix} \left(\delta_n - \delta_n^p\right) \dfrac{\delta_n^{\max}}{\delta_n^{\max} - \delta_n^p} \\ \left(\delta_s - \delta_s^p\right) \dfrac{\delta_s^{\max}}{\delta_s^{\max} - \delta_s^p} \end{bmatrix} \tag{52}$$

being $\delta_n^{\max}$ and $\delta_s^{\max}$ the maximum values of the normal and tangential displacement jump components over the entire load history, respectively.

During the unloading phase, the plastic contribution is computed as a fraction of the maximum normal displacement jump, i.e., $\delta_n^p = \gamma_n \delta_n^{\max}$.

It follows that the normal and tangential stiffnesses during the unloading phase take into account the residual plastic deformations as follows:

$$K_i^p = \frac{\left(1-D\right) K_i^0 \delta_i^{\max}}{\delta_i^{\max} - \delta_i^p} \quad \text{with} \quad i = n, s \tag{53}$$

where K_n^0 and K_s^0 denote the initial normal and tangential stiffnesses under tensile and compression stresses. The contact behavior between two crack faces has been simulated by an adaptive formulation of the tangent stiffness at the point in which the cohesive stresses change from tensile to compressive, considering the effect of the concrete aggregates that obstruct the complete crack closure. To this end, the partial closure of the cracks is described by the following cohesive normal stress:

$$t_n^c = \begin{cases} K_n^c \left(\delta_n - \delta_n^p\right) & \text{for} \quad \delta_{n0}^p \le \delta_n \le \delta_n^p \\ K_n^0 \delta_n & \text{for} \quad \delta_n < \delta_{n0}^p \end{cases} \tag{54}$$

The normal stiffness, i.e., K_n^c, at the intermediate condition of partial contact assumes the following relation:

$$K_n^c = \frac{K_n^0 + (1-\gamma_n)\beta K_n^p}{1+\beta} \tag{55}$$

according to which the initial compression stiffness K_n^0 is gradually reduced as the damage level increases by means of a scalar factor β. A unilateral contact constraint enforced by a penalty method to prevent the interpenetration phenomenon is active when the actual displacement reaches the value of δ_{n0}^p, expressed as:

$$\delta_{n0}^p = -\frac{\delta_n^p K_n^c}{K_n^c + K_n^0} \tag{56}$$

The crack initiation is governed by a quadratic nominal stress criterion:

$$\left(\frac{\langle t_n \rangle}{\sigma_{\max}}\right)^2 + \left(\frac{t_s}{\tau_{\max}}\right)^2 = 1 \tag{57}$$

where $\sigma_{\max}$ and $\tau_{\max}$ are the critical normal and tangential stresses, respectively. The equivalent displacement jump δ_m^0 has been defined as follows, and it is valid only for $\delta_n > 0$:

$$\delta_m^0 = \delta_n^0 \delta_s^0 \sqrt{\frac{1+\beta_m^2}{(\delta_s^0)^2 + (\beta_m \delta_n^0)^2}} \tag{58}$$

The complete traction-separation laws for mode-I and mode-II fracture processes, are reported in Fig. 21.

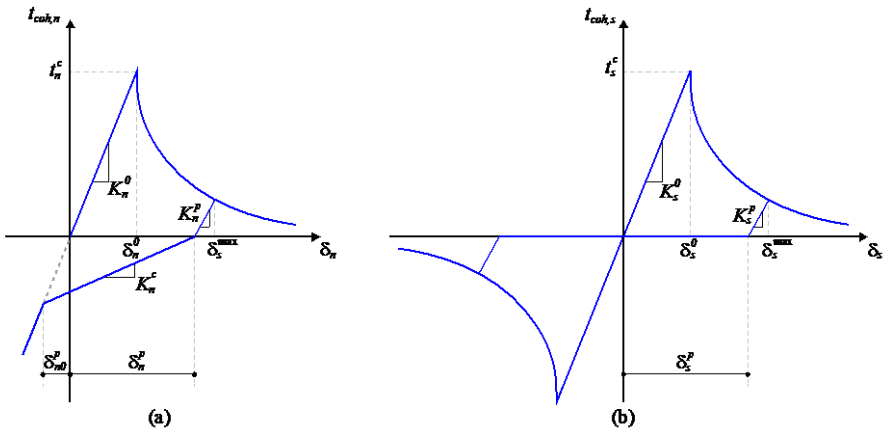

Fig. 21. Traction-separation laws adopted for mode I (a) and mode II (b) fracture.

2.1.3 Nano-modified FRP Reinforcement modeling

The modeling strategy adopted for the nano-modified FRP reinforcement system is based on a cohesive interface approach that takes into account the reinforcing effect of the nanomaterials by adopting bond–slip relations suitably calibrated from experimental results. In particular, the reinforcement system, consisting of the adhesive and FRP sheets, is modeled by four-node quadrilateral finite elements with a linearly elastic behavior, while the physical interface between concrete and FRP is modeled by zero-thickness cohesive elements equipped with a bond–slip law. From a computational point of view, the reinforcing effect provided by the nanomaterials embedded in the epoxy resin has been taken into account by increasing the fracture energy and tangential critical stress of the adopted bond–slip law. As a matter of fact, nano-modified materials, such as nano-reinforced concrete and composites, provide greater strength and fracture toughness than the corresponding unmodified materials [110–112].

Here, a trapezoidal bond–slip law, proposed by [113] to investigate ductile adhesives in laminate structures, has been modified and employed to describe the bond behavior between the concrete and nano-enhanced FRP system. It is expressed as

$$\tau = \begin{cases} \dfrac{\tau_{\max}}{s_1} s & 0 < s \le s_1 \\ \tau_{\max} & s_1 < s \le s_2 \\ \tau_{\max} \dfrac{s_f - s}{s_f - s_2} & s_2 < s \le s_f \\ 0 & s_f < s \end{cases} \tag{59}$$

where $\tau_{\max}$ is the maximum tangential strength, while s_1 and s_2 are the relative slip identifying the length of the plateau branch. The complete detachment of the reinforcement system occurs at the final slip s_f where the tangential stress drops to zero. The values of these parameters have been chosen to better fit the results of a standard shear test. Moreover, similarly to what was proposed by [113], relationships between the bond–slip parameters and the material properties of the nano-modified adhesive can be proposed. In particular, the s_1 parameter, coinciding with the onset of the plateau branch, results in a very small value and is unchanging with the mechanical properties of the adhesive, and it is set equal to $s_1 = 0.01\ \text{mm}$. On the other hand, the slips s_2 and s_3 strongly depend on the fracture energy of the materials, and, as reported in [113], can be computed as $s_2 = G_f / \tau_{\max}$ and $s_3 = s_1 + s_2$, respectively. It follows that the shear strength at the concrete–FRP interface immediately reaches its critical values, remaining mainly constant up to the complete separation. The maximum tangential stress $\tau_{\max}$ and fracture energy G_f will be suitably calibrated by fitting the available experimental results. Such a bond–slip law is also employed for standard adhesives without the incorporation of nanomaterials, showing a smaller plateau length due to the lower value of the fracture energy with respect to the nano-modified epoxy resin. The cohesive elements inserted along the

physical interface are also able to predict potential normal separations, through the same cohesive law reported in Equation 59, but as a function of the normal displacement jump occurring along the interface. Moreover, both tangential and normal cohesive laws consider unloading to the origin. Numerical details, including the adopted cohesive law, are reported in the following figure.

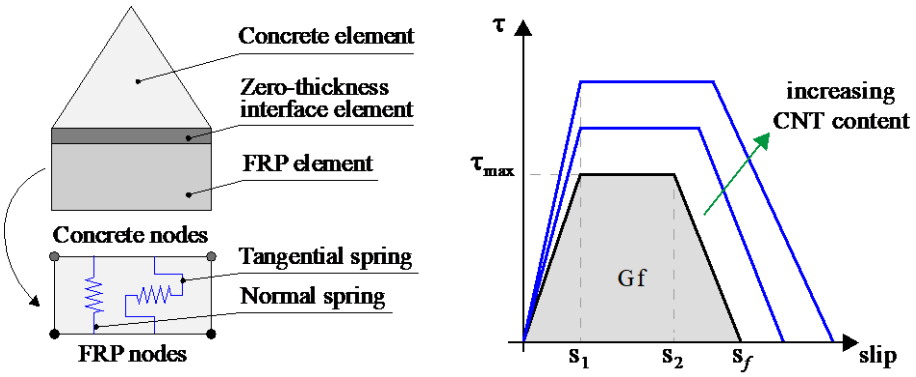

Fig. 22. Computational details of the proposed normal/tangential cohesive model together with the adopted bond-slip law.

2.1.4 Mixed-mode cohesive frictional interface model

The study of more complex problems, in terms of stress states acting on structural elements, requires an appropriate calibration and adaption of the previously introduced cohesive model. In particular, if the aim is to reproduce the non-linear behavior of elements subjected to combined compression/shear stress, i.e. the usual loading conditions in masonry structures, it is essential to incorporate a friction model that is able to simulate such stress states adequately. To this end, the numerical formulation previously introduced has been further improved, by incorporating the friction effects in the mode II traction-separation law, in order to adequately model the constitutive behavior of the cohesive elements during the unloading phase characterized by compression states, especially when a mixed-mode fracture condition is analyzed. In detail, according to the Coulomb-type frictional model, the total cohesive tangential stress is defined as follows:

$$t_s^{tot} = t_s + t_s^{fric} \tag{60}$$

where t_s and t_s^{fric} represent the cohesive and friction contribution, respectively.
General speaking, the total cohesive tangential stress can be expressed as in the following expression, with the friction contribution that acts when a compression state is reached:

$$t_s^{tot} = \begin{cases} t_s^c - \mathrm{sgn}\left(\delta_s\right)\mu_f t_n^c & \delta_n \le \delta_{np} \\ t_s & \delta_n > \delta_{np} \end{cases} \tag{61}$$

according to the nomenclature introduced in section 2.1.2. The term t_n^c represents the cohesive contribution in the mode I traction-separation law.

the friction coefficient μ_f, according to [114], assumes the following expression:

$$\mu_f = \begin{cases} \mu_0\left(\left|\delta_s\right|/\delta_s^0\right) & \delta_m^{\max} \le \delta_m^f \\ \mu_0 & \delta_m^{\max} > \delta_m^f \end{cases} \tag{62}$$

where δ_s^0 and $\delta_m^{\max}$ are the tangential displacement jump at the damage initiation and the maximum value of the displacement jump all over the loading history. Eq. 62 involves the initial friction coefficient μ_0, set equal to 0.3. In the following figure, the mode II frictional traction separation law, as well as the mode I contribution, are presented.

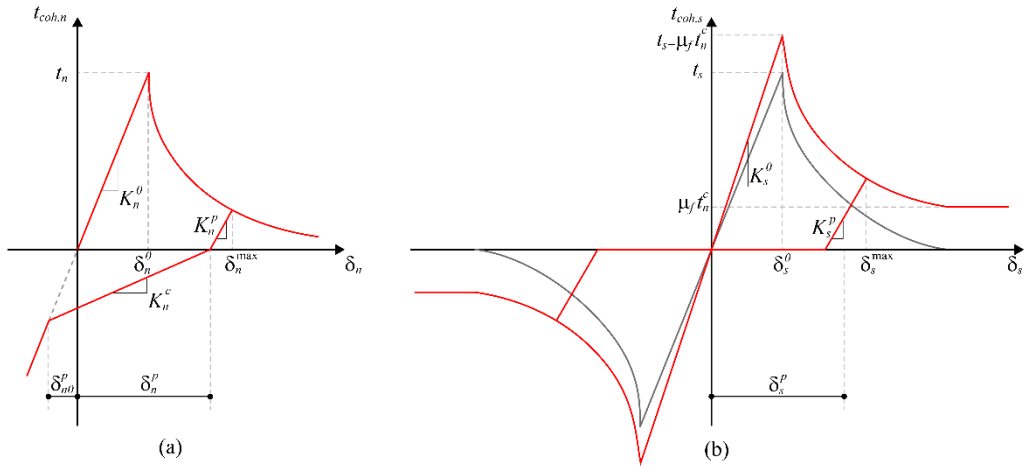

Fig. 23. Traction-separation law for mode I (a) and mode II fracture conditions (b).

2.2 An embedded truss model for the interaction between concrete and steel reinforcement

The modeling approach of the steel reinforcement relies on the embedded truss model recently introduced in [115] and schematically represented in Fig. 24. In particular, longitudinal rebars and stirrups have been modeled by axially loaded 1D truss elements with elastoplastic constitutive behavior and linear hardening to describe the steel yielding stage (see Fig. 24). These elements are embedded into the concrete mesh by means of zero-thickness interface elements equipped with the following bond-slip relation proposed by the CEB-FIP model Code [116]:

$$\tau = \begin{cases} \tau_{\max}\left(s/s_1\right)^{\alpha} & \text{for } 0 \le s \le s_1 \\ \tau_{\max} & \text{for } s_1 \le s \le s_2 \\ \tau_{\max} - \left(\tau_{\max} - \tau_{\text{res}}\right)\dfrac{s - s_2}{s_3 - s_2} & \text{for } s_2 \le s \le s_3 \\ \tau_{\text{res}} & \text{for } s_3 \le s \end{cases} \tag{63}$$

The parameters of this relation depend on the type of employed rebars, i.e. plain or ribbed bars. Specifically, in this work, ribbed bars with good bond conditions have been adopted and the slip parameters are taken equal to $s_1 = 1$ mm, $s_2 = 3$ mm, and $s_3 = 10$ mm while the maximum and residual tangential stresses are taken equal to $\tau_{\max} = 2.5\sqrt{f_c}$ and $\tau_{\text{res}} = 0.4\tau_{\max}$, respectively, with f_c the compression strength of the concrete.

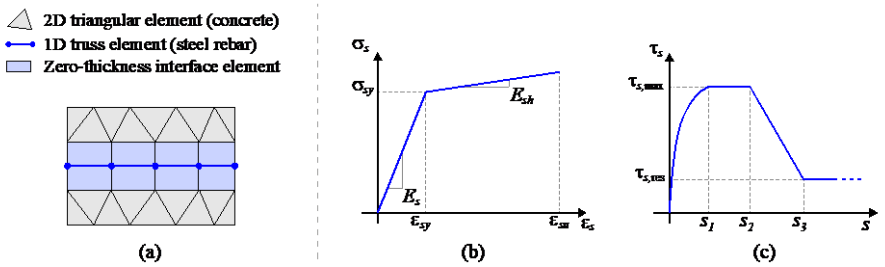

Fig. 24. Schematic representation of the embedded truss model (a) with the adopted constitutive (b) and bond-slip relations (c).

In this way, the interaction between rebars and surrounding concrete is simulated in a simplified discrete form avoiding a detailed representation of the rebars including reinforcement ribs and concrete lugs. Moreover, the 1D truss elements, in which all the individual steel rebars and stirrups at a given depth are concentrated, possess an equivalent section which is different from the concrete one and equal to the sum of the cross-section of each steel reinforcement bar. Finally, the slip is the

only displacement allowed in the rebar/concrete interface elements since the nodes of the truss and volumetric elements are constrained in the normal direction.

2.3 A single interface model for capturing debonding phenomena in FRP-strengthened structures

It is widely known that, for FRP-strengthened structures, one of the damage phenomena on which greater attention must be paid, especially to adequately account for it in structural models (i.e. Finite Element Models), is debonding. This phenomenon may occur between the adhesive and the FRP sheet or at the material interface between the adhesive and substrate to which it is applied.

In order to consider both of the aforementioned damage modes, and in order to appropriately simulate the initiation and propagation of the debonding phenomena, a single interface model (SIM) has been proposed. Such a model is based on the cohesive formulation previously introduced in section 2.1, but considers a priori known crack path (see Fig. 25).

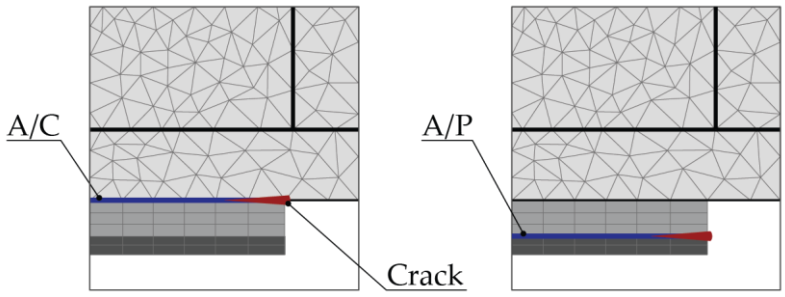

Fig. 25. Potential crack patterns predicted by the single interface model: adhesive/concrete (A/C) interfacial debonding (a) and adhesive/pate interfacial debonding (b).

2.4 A hybrid cohesive/volumetric nonlinear homogenization strategy for failure analysis of heterogeneous materials

In this section, the cohesive/volumetric finite element model, introduced in the previous sections, has been used in conjunction with a nonlinear homogenization strategy for the failure analysis of heterogeneous materials. In the following, the theoretical background of the proposed formulation is reported, while numerical results obtained on fiber-reinforced composite structures will be presented in section 3.2.

As is widely known, classical micromechanical approaches present some limitations (i.e. mesh sensitivity issues) in the presence of strain localization, related to the ill-posedness of the macroscopic boundary value problem. Several models can be found in the technical literature that are able to overcome this drawback [73,82,84,85,88,89,106,117], one of which is the continuous/discontinuous homogenization approach.

In this work, a continuous/discontinuous multiscale model for periodic microstructures, based on a hybrid cohesive/volumetric hierarchical homogenization is presented. The micro- and macro-scale are one-way coupled. Using a novel FE framework, two different and independent homogenized responses are deduced:

- a homogenized anisotropic damage evolution law;
- a homogenized mixed-mode traction-separation law.

It is easy to understand that the first extracted response is valid until the occurrence of strain localization.

The principal improvement of this multiscale approach is that the microscopically informed traction-separation law for the cohesive interfaces embedded in the volumetric mesh at the macroscopic scale, can be extracted in an “off-line” computation from the nonlinear homogenization response of a Repeating Unit Cell (RUC) or Representative Volume Element (RVE) for periodic and random microstructures, respectively. Moreover, this kind of approach is computationally efficient compared to semi-concurrent computational homogenization approaches like FE^2 methods [118,119].

In the present strategy, general nonlinear constitutive laws at either bulk or interface level are allowed to be adopted at the microscopic scale, whereas the Diffuse Interface Model (DIM) introduced earlier in this thesis, is used for representing arbitrary cracks at the macroscopic scale.

2.4.1 Theoretical background of the cohesive/volumetric homogenization approach

A discretized 2D macroscopic solid Ω_M is considered here (the subscript M denoting the macro-scale), subjected to external tractions $\bar{\boldsymbol{t}}_M$ and imposed displacements $\bar{\boldsymbol{u}}_M$ on its Neumann and Dirichlet boundaries, respectively (see Fig. 26(a)). This solid is damageable, so that fracture is represented via a Diffuse Interface Modeling (DIM) approach, according to which cohesive interfaces, denoted by Γ_M^{coh}, are placed along all the internal mesh boundaries. Given the periodic nature of the considered microstructure, a suitable Repeating Unit Cell (RUC) is defined to microscopically derive the bulk and interface constitutive relations, which are valid before and after strain localization, respectively (see Fig. 26(b) and Fig. 26(c)).

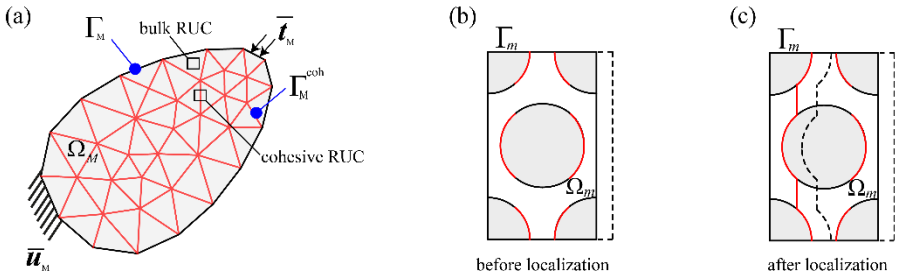

Fig. 26. Schematic representation of the cohesive/volumetric homogenization approach: homogenized macroscopic problem (a), bulk microscopic model (b), and cohesive microscopic problem (c).

Under the assumptions of scale separation and local periodicity, the macro-stress and strain fields, indicated by $\boldsymbol{\sigma}_M$ and $\boldsymbol{\varepsilon}_M$ respectively, are defined in a standard manner as functions of boundary tractions $\boldsymbol{t}_m$ and displacements $\boldsymbol{u}_m$:

$$\boldsymbol{\sigma}_M = \frac{1}{|\Omega_m|}\int_{\Gamma_m} \boldsymbol{t}_m \otimes \boldsymbol{x}_m dS, \qquad \boldsymbol{\varepsilon}_M = \frac{1}{|\Omega_m|}\int_{\Gamma_m} \boldsymbol{u}_m \otimes_s \boldsymbol{n}_m dS \tag{64}$$

In Eq. 64, Ω_m and Γ_m represent the RUC and its external boundary, respectively, whereas $\boldsymbol{x}_m$ is a generic material point inside the RUC, and $\boldsymbol{n}_m$ is the outer unit normal at the RUC boundary. The micro-to-macro transition based on the use of Eq. 64 is no longer objective if applied after strain localization has appeared. The resulting localization band, whose width goes to zero in a cohesive model, is described as a zero-thickness interface, equipped with a homogenized traction-separation law, which can be extracted from the homogenized bulk response by using the following relations:

$$\boldsymbol{t}_M^{\text{coh}} = \boldsymbol{\sigma}_M \boldsymbol{n}_M, \qquad \frac{1}{h}\,\boldsymbol{u}_M \otimes_s \boldsymbol{n}_M = \boldsymbol{\varepsilon}_M \tag{65}$$

$\boldsymbol{n}_M$ being the normal to the macro-crack (supposed to be a priori known coherently with the Diffuse Interface Model adopted at the macro-scale), and h is the RUC size measured parallel to $\boldsymbol{n}_M$. The homogenized traction-separation law, as computed via Eq. 65, is subsequently depurated from the hardening contribute, associated with the early crack propagation prior to strain localization. In order

to exclude this contribution and, thus, to consider only the softening branch of this law, an energy-based split of the total homogenized traction-separation law is proposed (shown in Fig. 27(a)), leading to a proper definition of the localized macroscopic crack opening displacement $[\![\boldsymbol{u}_M^{\text{loc}}]\!]$, as depicted in Fig. 27(b).

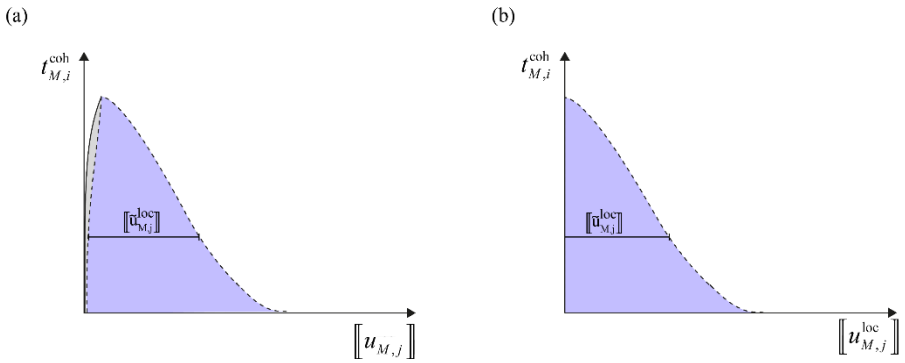

Fig. 27. Derivation of the homogenized traction-separation law: energy-based split of the total homogenized traction-separation law (a), and purely softening portion of the homogenized traction-separation law.

Using this procedure, the proposed model is able to overcome the typical drawbacks of standard homogenization approaches.

In particular, how highlighted by Gitman et al [72] and represented in Fig. 28 and Fig. 29, a non-objective overall stress-strain response are typically found by considering different sizes of the Representative Volume Element.

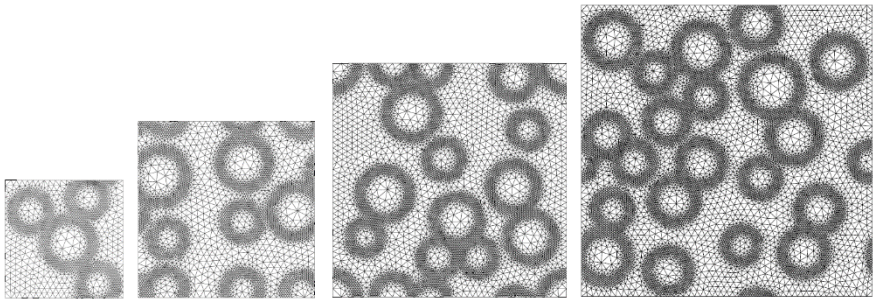

Fig. 28. Different sizes of the Representative Volume Element (RVE), adapted from [72]. From 10x10 mm^2 to 25x25 mm^2 (from left to right).

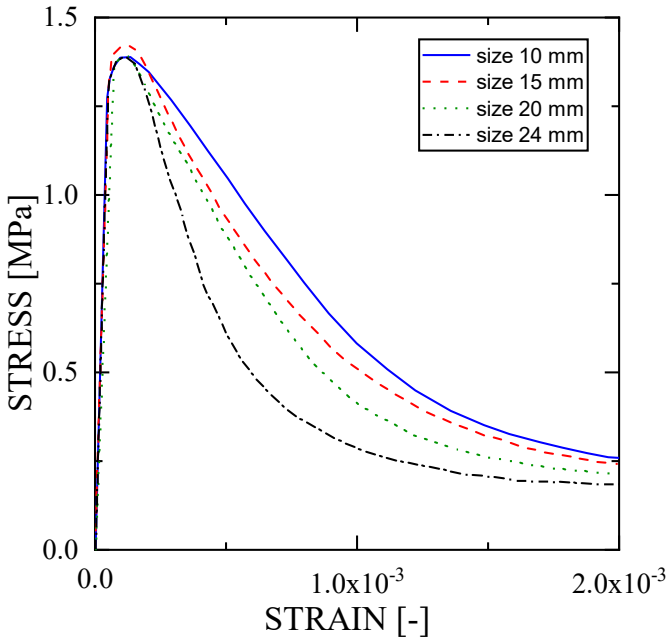

Fig. 29. Non-objective overall stress-strain response for softening materials by considering different sizes of the Representative Volume Element (RVE).

The interface homogenization, defined after that strain localization has been observed, overcome this issue and as depicted in Fig. 31, objective overall responses are found for different RVE sizes.

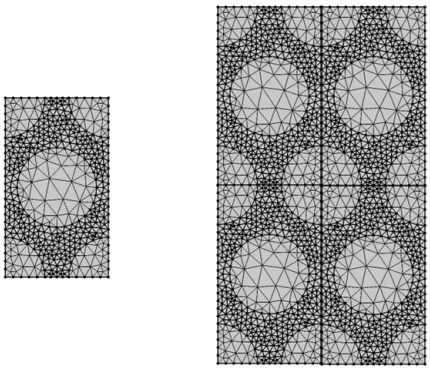

Fig. 30. Different RVE sizes: 1x1 cell and 2x2 cells (from left to right).

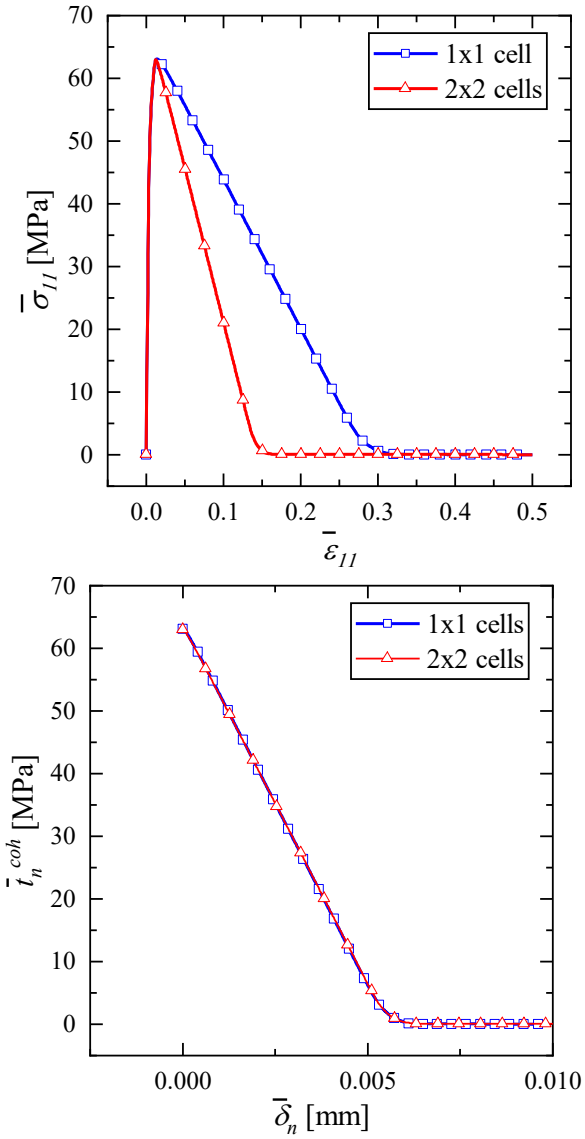

Fig. 31. Objective overall response due to the proposed interface homogenization step.

The proposed hybrid cohesive/volumetric nonlinear homogenization can be numerically implemented by considering three operational step:

- Computation of the undamaged elasticity tensor by means of the solution of linear boundary value problems for the RUC subjected to different pure macro-strain paths;
- Computation of the homogenized damage evolution law, extracted from the stress-strain relations obtained via a non-linear bulk homogenization along different paths;
- Derivation of the homogenized traction-separation law, obtained by projecting the previous nonlinear stress-strain relations along $\boldsymbol{n}_M$ (which varies depending on the actual orientation of the embedded cohesive interfaces for the macro-scale problem).

3. Numerical results: Failure analysis of heterogeneous materials

This chapter is devoted to the application of the proposed numerical model, widely explained in Chapter 2 of this work, to the failure analysis of heterogeneous materials. In particular, section 3.1, reports a numerical investigation of the reinforcing effect of nano-modified epoxy resin on the structural response of fiber-reinforced polymer (FRP)-plated reinforced concrete (RC) components. In detail, an integrated model, based on the cohesive crack approach previously introduced, is employed in combination with a bond-slip model to perform a failure analysis of strengthened structures.

In Section 3.2, instead, the numerical model has been used to predict the nonlinear response of masonry structures subjected to in-plane loading conditions. According to the Diffuse Interface Model, material nonlinearities caused by fracture phenomena at mortar joints are reproduced by means of zero-thickness interface elements placed between all brick/mortar and mortar/mortar interfaces comprised into the volumetric finite element mesh. The main novelty is the adoption of a cohesive-frictional interface model for reproducing the inelastic response under combined shear/compression stresses.

3.1 Effect of nano-modified epoxy resin on the behaviour of FRP-plated RC structures

A double lap shear test, experimentally analyzed by [110], has been simulated to calibrate the bond parameters required by the bond–slip law of the cohesive elements inserted along the interface between the concrete and nano-modified FRP plate. The geometry and boundary conditions of the tested specimen are depicted in Fig. 32. In particular, as reported in the experimental work [110], concrete blocks were cast into special wooden forms, and then the concrete surfaces were roughened using a diamond grinding disk and cleaned using a vacuum cleaner. After this, the fiber sheets were cut to the desired sizes and were bonded to the two opposite sides of a 150-mm-thick concrete prism using either neat or CNT-modified epoxy resin. The bonding length of the FRP sheet was 100 mm, leaving a length of 25 mm from the top edge of the prism un-bonded. The concrete Young's modulus and its compressive strength were equal to 30 GPa and 34 MPa, respectively, as reported in the reference experimental work [110]. The reinforcement system consists of an FRP sheet with a thickness of 1 mm. Two types of FRP have been employed: the first one is based on carbon fibers, while the second one is based on glass fibers, with an elastic modulus of 230 GPa and 73 GPa, respectively, and tensile strength of 4900 MPa and 3400 MPa, respectively, as reported in the reference experimental work [110]. These FRP sheets are bonded on the concrete prisms by neat or

nano-modified epoxy resin, adopting a concentration of CNTs in the nano-modified epoxy equal to 3.4 wt%.

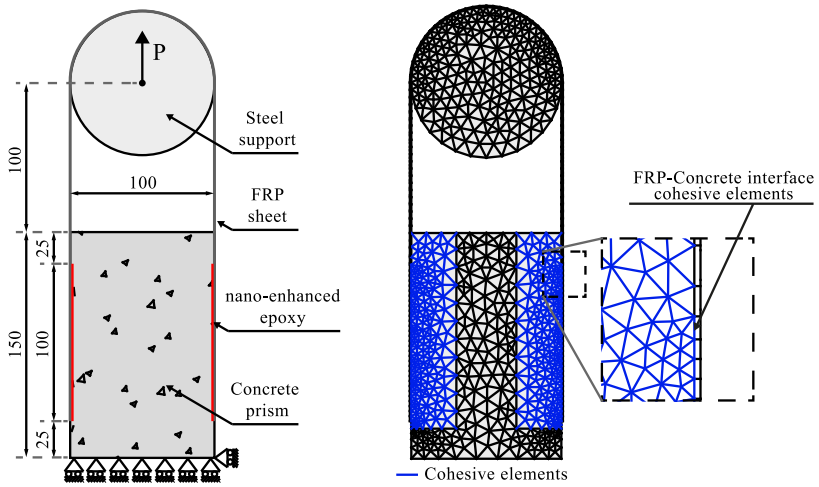

Fig. 32. Simulated double lap shear test: geometry and boundary conditions (a) and finite element discretization (b).

An unstructured mesh is employed to discretize both the concrete prism and the circular steel support where the load is applied, while a mapped mesh is used for the FRP sheet (see Fig. 32). A mesh refinement is performed in the critical zone near the FRP layer, prescribing a number of 30 elements with a length of 3.33 mm along the FRP–concrete interface. In this zone, according to the proposed numerical strategy explained in Section 2.1, zero-thickness cohesive elements are inserted along the mesh boundaries to simulate damage phenomena, including potential detachments of the concrete substrate. The main cohesive parameters required by the adopted traction–separation law for concrete, illustrated in section 2.1.1, are the tensile strength σ_c and fracture energy G_{Ic}, and are here chosen equal to 3.1 MPa and 100 N/m, as reported in the reference experimental work [110]. The corresponding mode-II cohesive parameters, i.e., τ_c and G_{IIc}, difficult to derive from experimental tests, have been set by following the numerical calibration proposed in [120], as $\tau_c = \sqrt{2}\sigma_c$ and $G_{IIc} = 10G_{Ic}$. Additional zero-thickness cohesive elements are inserted along the physical interface, between the concrete and the FRP system, in order to simulate interfacial debonding initiation and propagation. These interface elements are equipped with a bond–slip law, explained in Section 2.1.3, able to predict the reinforcing effect of the nanomaterials embedded in the epoxy resin, whose required parameters for neat and CNT-modified adhesives are chosen to better fit the experimental results and reported in Table 1.

Table 1. Parameters required by the bond-slip law for the FRP-reinforced concrete prisms.

Epoxy Resin	s_1 [mm]	s_2 [mm]	s_f [mm]	τ_{max} [MPa]	G_f [N/m]
Neat	0.01	0.34	0.35	2	680
CNT-modified	0.01	0.695	0.705	3.6	2500

3.1.1 Numerical Results of the Double Lap Shear Test

Fig. 33 shows the average bond stress versus slip relationships of the tested specimens. The average bond stress has been computed as the ratio between the predicted load and the area where the FRP sheet is bonded. In particular, the structural responses reported in Fig. 33(a) refer to the specimens with neat (N) and nano-modified (CNT) carbon–FRP sheets, i.e., C-N and C-CNT specimens, while those reported in Fig. 33(b) refer to the corresponding glass–FRP sheets, i.e., G-N and G-CNT.

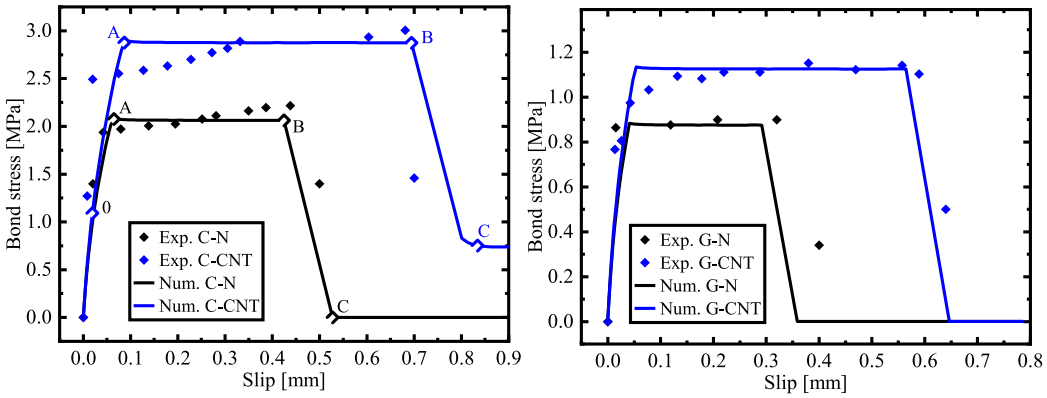

Fig. 33. Bond stress versus slip relationship of the tested specimens: carbon-FRP strengthened specimens (a) and glass-FRP strengthened specimens.

The numerical results, obtained by the proposed model, are in good agreement with the experimental ones. All numerical curves immediately exhibit non-linear behavior until the peak in the shear stress. Subsequently, the shear stress remains constant while the slip increases, and drops to zero once debonding phenomena occur. As observed in the experimental test, the CNT content embedded in the epoxy resin improves the bond stress and the energy absorption capacity, with respect to the specimens with neat epoxy resin. Fig. 33 shows how the specimens equipped with the nano-additive resin exhibit higher ultimate shear stress and slip values than the non-additive prisms used in the control test. Specifically, bond stress increases of 28% and 22% have been obtained from the numerical simulations of the C-CNT and G-CNT specimens, respectively, with respect to the C-N and G-N specimens. Such behavior is due to the reinforcing effect of the incorporation of CNTs in the epoxy resin, which prevents the early onset and propagation of cracks at the FRP–concrete interfaces. As a result, this led to the modification of the failure mechanism of the specimen. In

particular, the classical peeling failure obtained by the C-N specimen is not observed in the C-CNT specimen, where the debonding of the FRP sheet is accompanied by the detachment of the adjacent concrete substrate (see Point C of Fig. 34(b)). Such a failure mode is mainly due to the higher shear strength, provided by the nanomaterials, than the tensile strength of the concrete. The deformed configurations together with the related concrete stress maps for the neat and the nano-modified FRP-strengthened specimens at different slip values, highlighted in Fig. 33 with Points A, B, and C, are reported in Fig. 34.

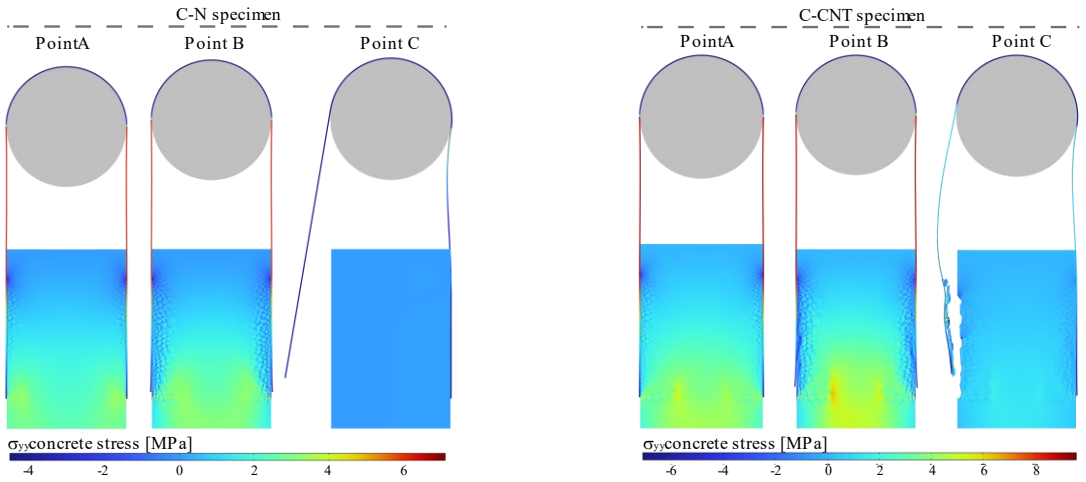

Fig. 34. Deformed configurations (magnified by a scale factor of 15) of the tested specimen: neat carbon-FRP-strengthened specimen (a) and nano-modified-carbon-FRP-strengthened specimen (b).

High stress values are predicted near the concrete–FRP interface, for both tested specimens, from the earliest load levels (Point A). Subsequently, significant slips are observed in the deformed configuration of Point B, especially for the C-CNT specimen. After this, two different failure modes are predicted by the tested specimens (see Point C of both specimens). The C-N specimen exhibits a purely debonding failure mode, whereas the C-CNT specimen shows a debonding that involves the adjacent concrete substrate. These different failure phenomena have been well predicted by the proposed model, able to simulate the damage in both the concrete–FRP interface and concrete phase, with respect to the common numerical models mainly focused on the non-linear processes occurring in the physical concrete–FRP interface.

The reinforcing effect induced by the incorporation of nanomaterials in the epoxy resin can be also observed in the numerically predicted strain of the FRP layer. In particular, Fig. 35 shows the FRP strain predicted at different slip values (Points 0, A, B, and C highlighted in Fig. 35) concerning the specimens with neat (Fig. 35(a)) and nano-modified (Fig. 35(b)) carbon–FRP layers. We can note that, after the elastic stage (Point 0), where the strains are similar in both tested specimens, the nano-modified FRP-layered sample predicts higher strain values (Points A and B), of approximately 38.9% in the final part of the bonded zone, with respect to the neat FRP-layered specimen. Moreover, after

the brittle failure occurs (Point C), the strains of both specimens drop to zero. However, the nano-modified FRP-strengthened sample, characterized by a failure mode with concrete substrate detachments, shows no zero strain values in the contact zones between the concrete prism and FRP system.

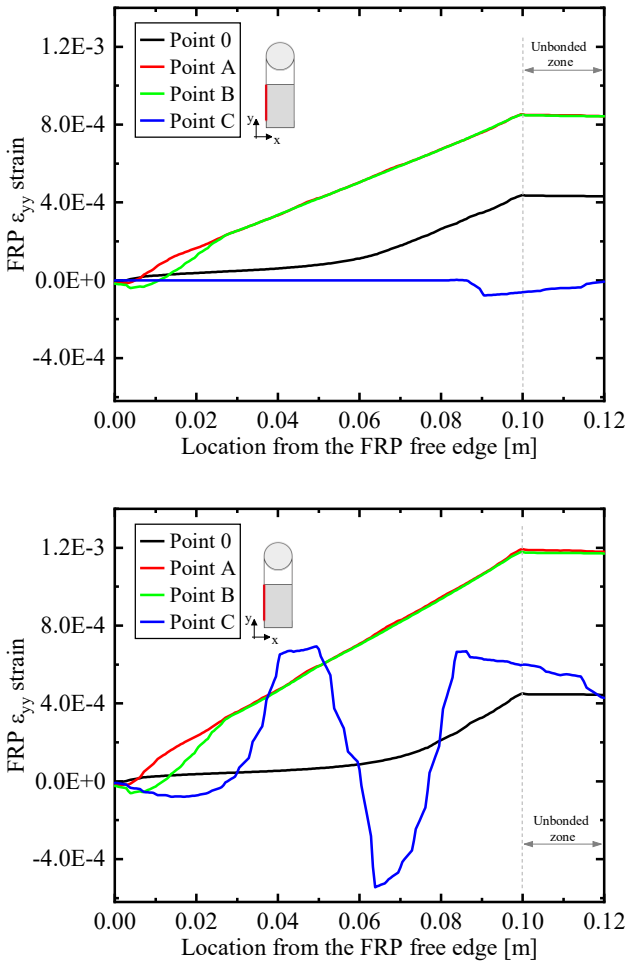

Fig. 35. FRP strain predicted by the proposed model in the neat Carbon-FRP-strengthened specimen (a) and nano-modified Carbon-FRP strengthened specimen (b).

3.1.2 Analysis of RC structures strengthened with Nano-modified FRP plate

The proposed model has been here employed to investigate the structural responses of RC beams externally strengthened with an FRP plate bonded on the concrete surface by either neat or nano-modified epoxy resin, subjected to a four-point bending test experimentally performed by [121]. In particular, as reported in the experimental work [121], the tested beams were cast into wooden molds, and, after 28 days, the beams were cleaned before the resin was applied. A layer of epoxy or CNT-modified epoxy was directly applied on the beam surface. Specifically, the simulated test involves a control beam (without FRP reinforcement); an FRP-plated RC beam with neat epoxy resin, denoted as the "N-E Beam"; and an FRP-plated RC beam with nano-modified epoxy resin, denoted as the "CNT-E Beam". Both the geometric details and boundary conditions are reported in Fig. 36.

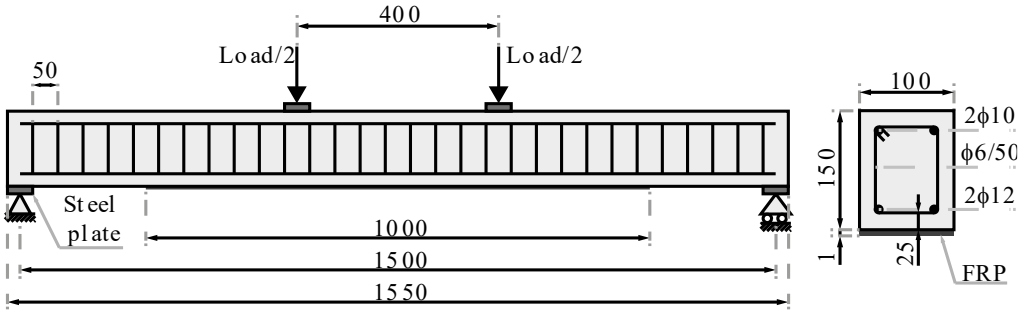

Fig. 36. Geometry and boundary condition of the tested FRP-plated RC beam.

The main material properties are taken from the experimental work [121]. In particular, the adopted Young's modulus and Poisson's ratio are equal to 20 GPa and 0.2 for concrete, and 200 GPa and 0.3 for rebar steel, respectively. The compressive and tensile strengths of the concrete are set equal to 42.7 MPa and 2 MPa, respectively, while the steel yielding strength is reached at 418 MPa for the longitudinal rebars and 290 MPa for the stirrups. The external reinforcing system consists of a 1-mm-thick carbon fiber plate, already employed in the calibration test (Section 3.1.1), whose Young's modulus and tensile strength are equal to 28 GPa and 4900 MPa, respectively. The C-FRP plate is bonded to the concrete surface by either neat or nano-modified epoxy resin. In particular, the concentration of carbon nanotubes (CNTs) in the nano-modified epoxy resin was equal to 3.4 wt%.

The numerical analyses have been performed adopting the discretization illustrated in Fig. 37.

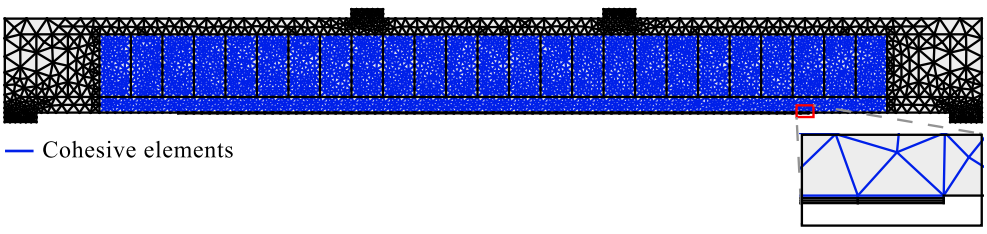

Fig. 37. Adopted FE discretization.

According to the numerical strategy illustrated in Section 2.1 of the present thesis, the cohesive parameters required by the adopted traction–separation law are the following: tensile strength σ_c and fracture energy G_{Ic} equal to 2.0 MPa and 100 N/m, as reported in the reference experimental work [121]. The corresponding mode-II cohesive parameters, i.e., τ_c and G_{IIc}, have been set by following the numerical calibration proposed in [120], as $\tau_c = \sqrt{2}\sigma_c$ and $G_{IIc} = 10G_{Ic}$. On the other hand, the cohesive elements placed along the physical interface between the concrete and FRP system are equipped with a trapezoidal bond–slip law, whose required material parameters, depending on the employed epoxy resin, are taken by the calibration analysis performed in the previous Section 3.1.1 (see Table 1).

3.1.2.1 Numerical Results of the Four-Point Bending Test

The numerically predicted loading curves are reported in Fig. 38. All beams exhibit the classical trilinear behavior of the reinforced concrete elements, consisting of the initial elastic stage, the subsequent main crack propagation stage, and, finally, the rebars' yielding, occurring at a load value of approximately 38.5 kN for the control beam and 44.2 kN for the FRP-plated beams.

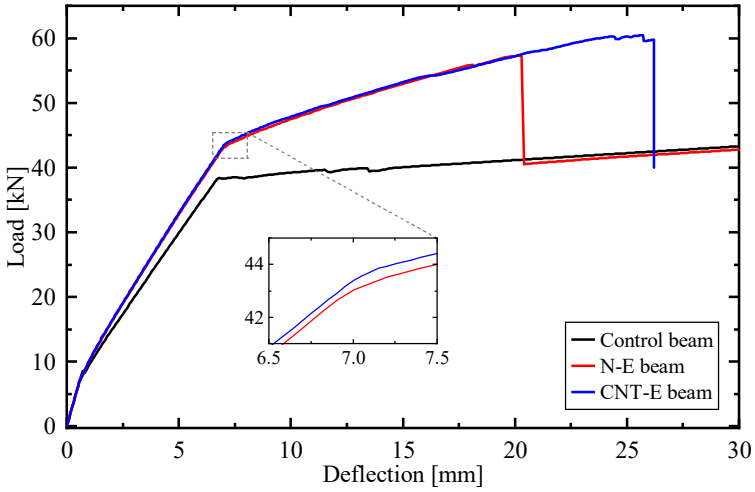

Fig. 38. Loading curves of the tested beams.

We can see that, as expected, the FRP-plated beams provide a stronger structural response with respect to the control beam, mainly due to the reinforcing effect induced by the externally bonded FRP system.

Concerning the FRP-plated beams, it is worth noting that the incorporation of carbon nanotubes in the epoxy resin of the CNT-E beam does not provide a significant improvement in the load-carrying capacity with respect to the FRP-plated beam without nanomaterials (N-E beam). This behavior seems to be in contrast with the results obtained in the previous Section 3.1.1, where the concrete prism reinforced with the nano-enhanced FRP sheet shows a higher peak load, energy absorption capacity, and final slip than the concrete sample with plain epoxy resin. As a matter of fact, the mechanical behavior of reinforced concrete beams is characterized by different stiffness factors, such

as tension-stiffening phenomena, concrete compressive behavior, and shear/bending strength offered by rebars and stirrups, and, therefore, the nanomaterial reinforcing effect is not clearly visible as that which occurs in the concrete prisms previously tested, whose mechanical response mainly relies on the bond–slip behavior offered by the nano-enhanced interface between the concrete and FRP sheet. However, an increment in the peak load and final deflection, of approximately 5.53% and 26.34%, respectively, is predicted by the CNT-E beam with respect to the N-E beam.

A comparison with the experimental results obtained in [121] has been carried out in terms of peak load and failure deflection of the FRP-plated beams with plain (B-S-NE beam) and nano-modified epoxy resin and is reported in Table 2. The compared values are in good agreement with each other, highlighting the good prediction capabilities of the proposed model to investigate nano-enhanced reinforced structures and validate the proposed model.

Table 2. Peak load and failure deflection obtained by the proposed model and experiment.

	Peak Load [kN]		Failure deflection [mm]	
	Model	Experiment	Model	Experiment
N-E beam	57.3	60.6	20.3	19.8
CNT-E beam	60.4	62.7	25.6	26.1

Similar to the results obtained in previous simulations on concrete prisms, different failure modes are predicted by the FRP-plated beams. In particular, the nanomaterial incorporation in epoxy resin provides better adhesion and shear strength between FRP and concrete, leading to debonding failure by ripping off the concrete cover. In Fig. 39, the final deformed configurations of the tested beams, i.e., the control beam, N-E beam, and CNT-E beam, are reported. It is worth noting that the FRP-plated beams exhibit crack patterns characterized by diffuse damage, with many cracks having smaller widths than the control beam. Moreover, the N-E beam, whose FRP plate is bonded with standard epoxy resin, collapses due to the intermediate crack-induced debonding of the FRP system, while the CNT-E beam, reinforced with a nano-modified FRP system, shows the well-known concrete cover separation failure.

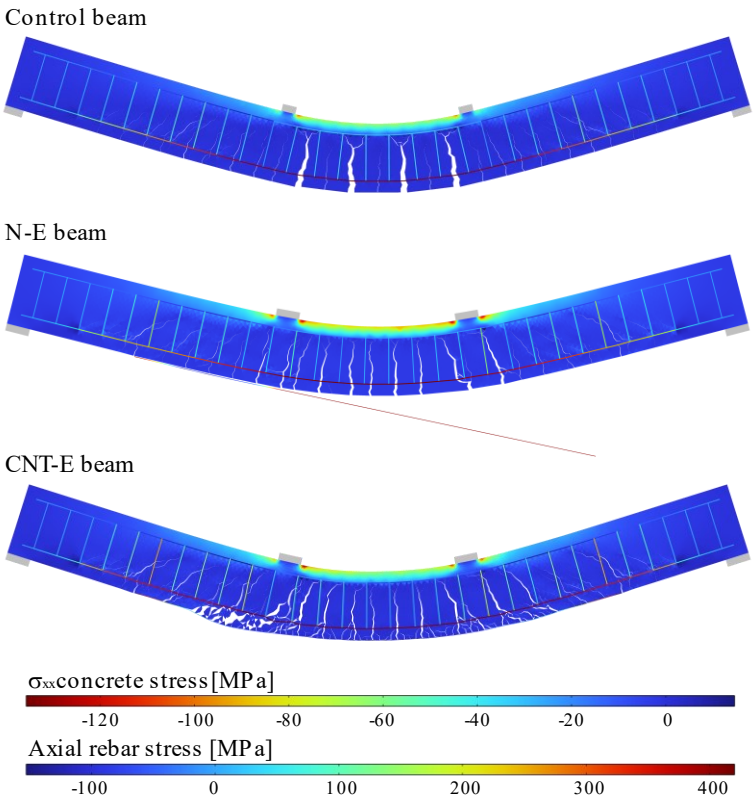

Fig. 39. Final deformed configurations and concrete stress maps of the tested beams.

An interesting comparison between the crack patterns of the FRP-plated beams with (CNT-E beam) and without (N-E beam) the incorporation of nanomaterials in the epoxy resin, at different deflection values, is reported in Fig. 40. Similar crack patterns are obtained for both beams at low deflection levels (4 mm and 7 mm). However, the CNT-E beam shows diffuse cracking within the concrete substrate between the lower rebars and the FRP system. As a matter of fact, the magnification of the crack pattern (Fig. 40(b)) of the CNT-E beam, at a deflection value of 15 mm, highlights the evolution of microcracks in the concrete cover, thus obtaining lower widths of the main cracks with respect to the N-E beam.

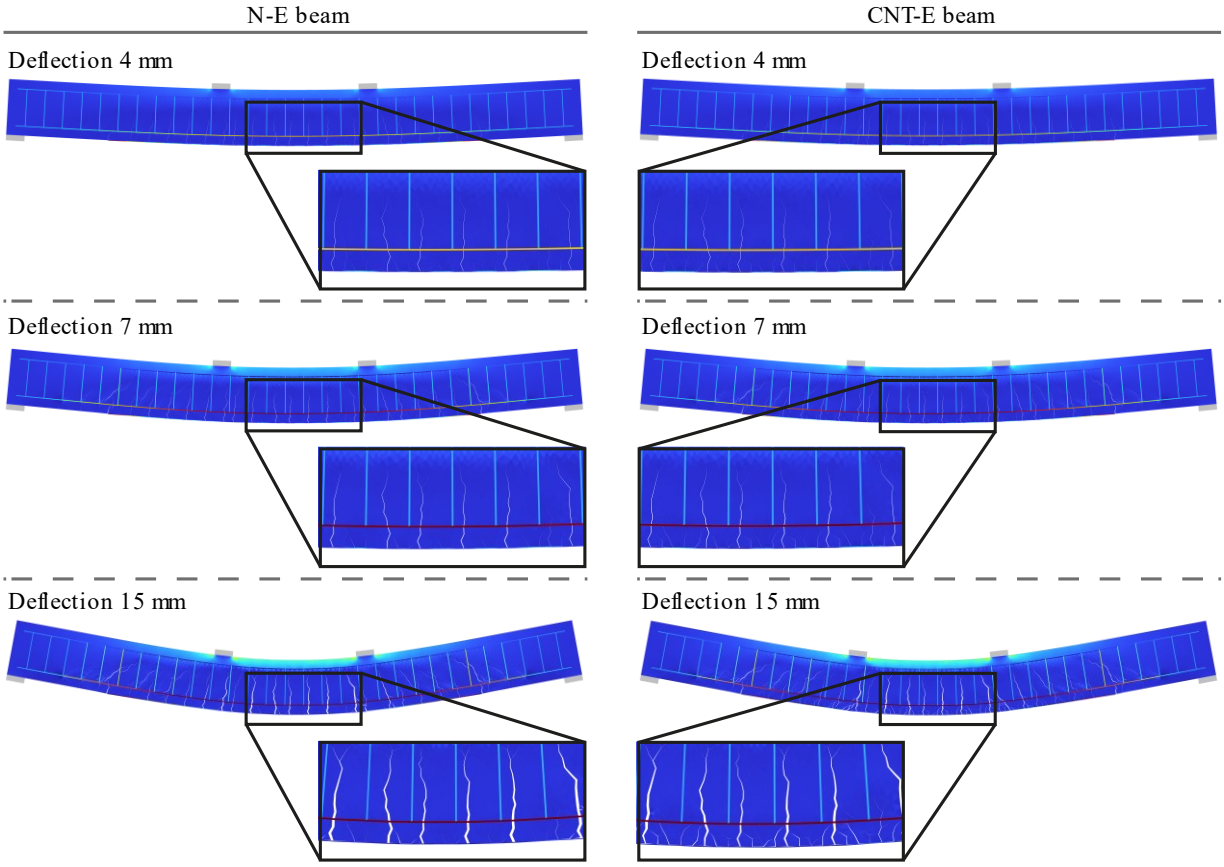

Fig. 40. Crack patterns of the N-E beam (a) and the CNT-E beam predicted by the proposed model at different deflection values.

This behavior is confirmed by the numerically predicted slips along the FRP–concrete interface reported in Fig. 41. High slip values are computed in correspondence with the main cracks for both tested beams; however, the CNT-E beam predicts the highest slip value of around 0.07 mm at the 15 mm deflection, and a reduction of approximately 76% with respect to the highest slip value recorded in the N-E beam equal to 0.31 mm. This result highlights the role of the carbon nanotubes, embedded in the epoxy resin, in providing better shear strength along the FRP–concrete interface, and it is well predicted by the proposed model.

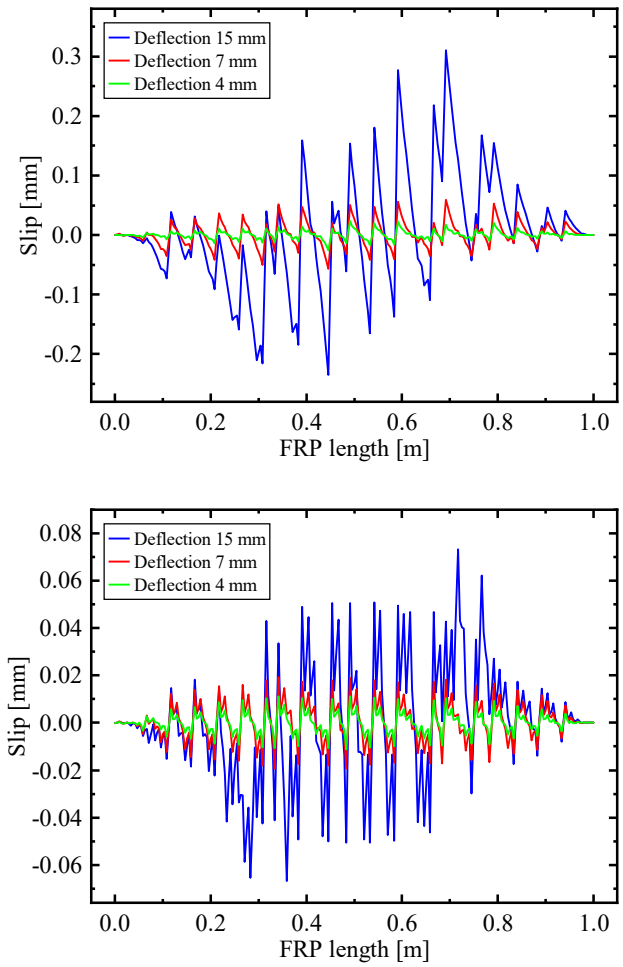

Fig. 41. Slip values along the FRP/concrete interface predicted by the proposed model for N-E beam (a) and CNT-E beam at different deflection values.

As it shown in the previous results, the novel numerical model based on a cohesive zone approach and an embedded truss model is employed for simulating the mechanical behavior of reinforced concrete elements retrofitted with nano-enhanced FRP systems by adopting a suitable bond–slip law to describe the bond behavior of the FRP–concrete interface. The conclusions of this work can be summarized in the following points:

The proposed bond–slip law has been carefully calibrated to match the experimental results of a concrete prism reinforced with nano-modified FRP sheets, and then employed to analyze FRP-plated RC beams.

The numerical results obtained by the simulation of concrete prisms externally reinforced with FRP sheets show an increment of 28% in the bond strength between the concrete and nano-modified FRP system with respect to the standard one.

Concerning the results obtained by the simulations of nano-modified FRP-plated RC beams, an increment in the peak load and final deflection, of around 5.53% and 26.34%, respectively, is predicted by the CNT-E beam with respect to the N-E beam. Moreover, a reduction in the slip between concrete and FRP, of around 76%, is obtained by the nano-modified FRP-plated beam with respect

to the beam without the nanomaterial incorporation, thus highlighting an improvement in the crack pattern.

As a future perspective of this work, the proposed model could be incorporated into a multiscale strategy in order to analyze damage phenomena at different length scales, as proposed in [122,123].

3.2 Application of the hybrid cohesive/volumetric homogenization strategy to fiber-reinforced composite beam

This section is devoted to the numerical experiments carried out to assess the reliability of the proposed multiscale model introduced in Section 2.4, which adopts a hierarchical continuous/discontinuous multiscale model and an inter-element fracture approach in a combined way. In particular, two tests have been simulated, both involving transverse cracking in fiber-reinforced composite specimens. In the first experiment, a three-point bending test on a composite beam is simulated, here used to validate the proposed methodology under global pure Mode-I fracture conditions. The second experiment is devoted to the numerical simulation of an L-shaped composite panel subjected to global mixed-mode boundary conditions.

3.2.1 Three-point bending test on a composite beam

The first case study here considered is a three-point bending test performed on fiber-reinforced composite beam, already analyzed from both experimental and numerical point of view by Canal et al. [124]. Assuming a plane-strain state, different numerical simulations have been performed on a notched beam (see Fig. 42) with a span s of 11.2 mm and a rectangular cross-section having a thickness t of 2 mm and a height of 2.8 mm. The notch has a length of 1.4 mm and a diameter of about 30 mm.

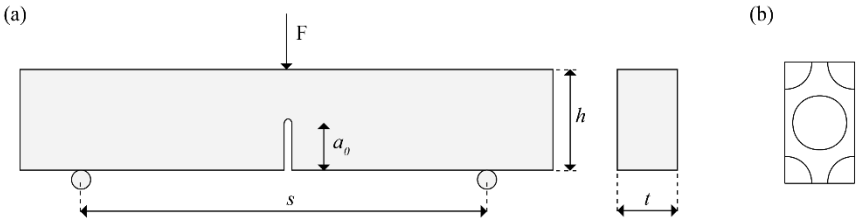

Fig. 42. Three-point bending test on a composite beam: geometry configuration and boundary conditions of the macroscopic specimen (a); geometry configuration and boundary conditions of the Repeating Unit Cell (b).

The composite beam possesses a periodic microstructure, placed in a hexagonal arrangement, made with an epoxy matrix and glass fibers, having a diameter of 15 μm and volume fraction of 54%. It is important to note that the homogenized material is also isotropic at the macroscopic scale. As already explained in Section 2.4, matrix cracking is represented by a Diffuse Interface Model, whereas fiber/matrix debonding is described by a Single Interface Model (see section 2.4.1 for more details). All the embedded microscopic interfaces are equipped with a phenomenological mixed-mode cohesive traction-separation law, characterized by two stiffness parameters, in normal and tangential directions (indicated as K_n and K_s, respectively) two strengths, in the normal and tangential directions (indicated as σ_{nc} and σ_{sc}, respectively), and two fracture energies (i.e., the Mode-I and Mode-II toughness, indicated as G_{Ic} and G_{IIc}).

In Table 3 and Table 4, the elastic properties (i.e., the Young's modulus E and the Poisson's ratio v) of the micro-constituents are reported, as well as all the parameters (i.e. stiffnesses, strengths, and fracture energies) of the embedded cohesive interfaces, including the (physical) fiber/matrix interfaces (capable to simulate fiber/matrix debonding), and the (mathematical) matrix/matrix interfaces (able to capture matrix cracking).

Table 3. Elastic parameters of the constituents.

Component	E **[GPa]**	υ **[-]**
Matrix	3.5	0.35
Fiber	74.0	0.20

Table 4. Elastic and inelastic parameters of the fiber/matrix interfaces.

K_n^0	K_s^0	t_n^c	t_s^c	G_I^c	G_{II}^c
[N/m^3]	**[N/m^3]**	**[MPa]**	**[MPa]**	**[N/m]**	**[N/m]**
1.000e8	1.000e8	50.0	75.0	150	150

The nonlinear behavior of the given composite beam has been extracted by means of the proposed multiscale approach, after defining a proper Repeating Unit Cell (RUC), which is depicted in Fig. 42(b). According to the three different operational steps reported in Section 2.4.1, the following computations have been performed.

Firstly, the nine components of the undamaged in-plane moduli tensor have been computed, by means of a classical linear homogenization step, involving three macro-strain paths, i.e., two uniaxial and a shear path (see Fig. 43).

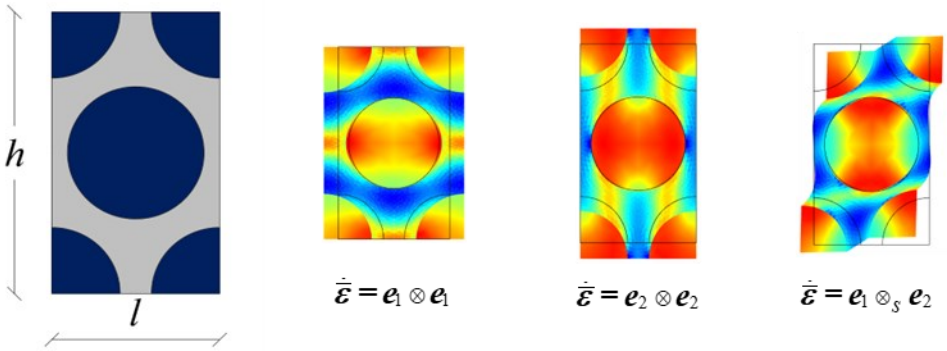

Fig. 43. Three macro-strain paths for classical linear homogenization step.

The values of the undamaged moduli are reported in the following table.

Table 5. Undamaged moduli.

$\bar{C}^{(0)}_{1111}$	$\bar{C}^{(0)}_{1122}$	$\bar{C}^{(0)}_{1112}$	$\bar{C}^{(0)}_{2222}$	$\bar{C}^{(0)}_{2212}$	$\bar{C}^{(0)}_{1212}$
[MPa]	**[MPa]**	**[MPa]**	**[MPa]**	**[MPa]**	**[MPa]**
13218	5828	0	13218	0	3692

Secondly, the nonlinear homogenized response of the microstructure has been derived, in terms of macro-stress σ^M_{11} vs macro-strain ε^M_{11} curve along the horizontal uniaxial macro-strain path direction, inducing a pure Mode-I macro-crack propagation, as depicted in Fig. 44(a). After this, the complete damaged moduli tensor has been derived by assuming an isotropic macroscopic damage evolution function $d_M = d_M\left(\varepsilon^M_{11}\right)$, which is directly extracted from the homogenized uniaxial stress-strain curve obtained from the principal path solution imposed on the RUC, as shown in Fig. 44(b).

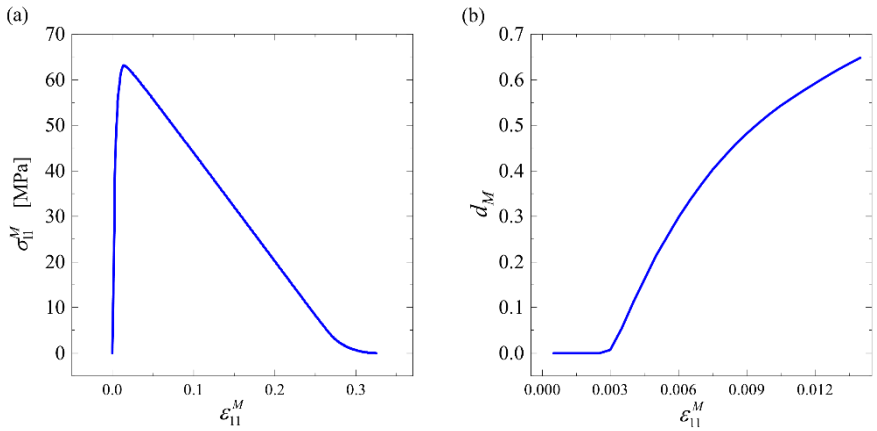

Fig. 44. Numerical outcomes of the nonlinear bulk homogenization step: homogenized uniaxial response of the Repeating Unit Cell (a), and homogenized damage evolution function (b).

Finally, a pure Mode-I homogenized traction-separation law, $t^{\text{coh}}_{M,n} = t^{\text{coh}}_{M,n}\left(\left[\!\left[u_{M,n}\right]\!\right]\right)$, n denoting the normal component of the relevant vectors, is extracted from the previously derived uniaxial stress-

strain relation, as shown in Fig. 45(a). This law is properly split in a purely hardening and softening portion, by virtue of the energy-based procedure presented in Section 2.4.1, so that a localized traction-separation law is extracted (see Fig. 45(b)).

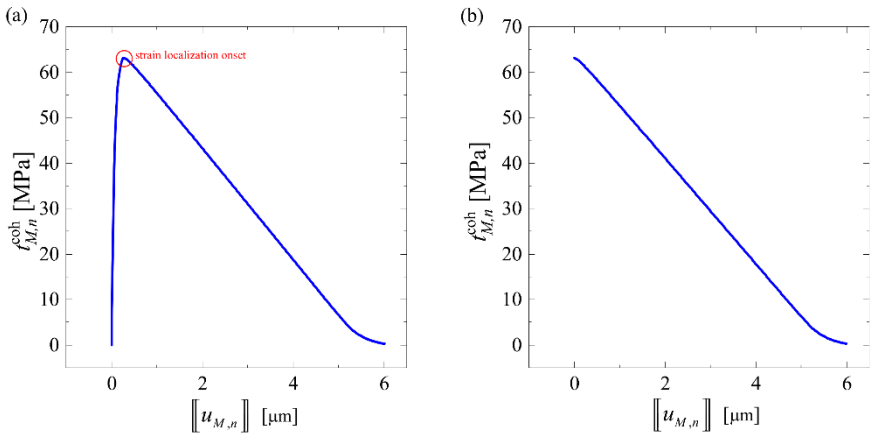

Fig. 45. Numerical outcomes of the nonlinear interface homogenization step: total homogenized traction-separation law (a), and localized homogenized traction-separation law (b).

The numerical outcomes of these three different steps have been obtained exclusively through off-line computations, and their validity is independent of the particular geometry and boundary conditions of the considered macroscopic problem. Therefore, both the macroscopic damage evolution function and the macroscopic traction-separation law may be regarded as material properties (for bulk and interface elements, respectively) to be used for performing general structural analyses of different specimens made of the same composite material.

After performing all these off-line computations involving the considered RUC, a macro-scale analysis of the composite beam, here referred to as Multiscale Numerical Simulation, is performed by using the previously derived databases (i.e., the aforementioned damage evolution and traction-separation laws) as material inputs. The macro-scale response is here reported in terms of relations between the applied force, F, and the Crack Mouth Opening Displacement, CMOD.

In order to investigate the influence of the mesh topology on the predicted overall structural behavior, two triangular mesh configurations have been considered for the Diffuse Interface Model (DIM), i.e., a cross-triangle quadrilateral (mapped) mesh and a Delaunay-type (random) mesh, shown in Fig. 46(a) and Fig. 46(b), respectively. For comparison purposes, an additional Single Interface Model is considered, in which the macro-crack path is assumed to be known in advance, as depicted in Fig. 46(c). All these models have been equipped with the previous micromechanically derived bulk and interface properties.

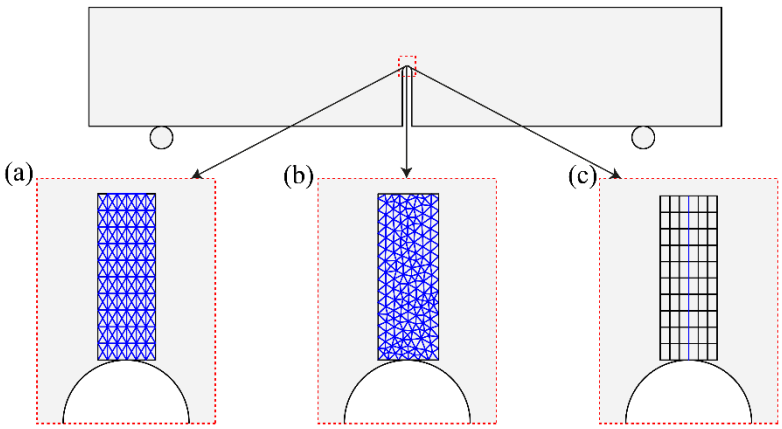

Fig. 46. Different finite element models for the Multiscale Numerical Simulations (MNS): Diffuse Interface Model with a mapped mesh (a), Diffuse Interface Model with a random mesh (b), and Single Interface Model (c).

As a validation step, the results of these multiscale analyses, here called Multiscale Numerical Simulations (MNSs), have been compared with the outcomes of a fully microscopic analysis, here denoted as Direct Numerical Simulation (DNS). In this analysis, taken as the reference, all the microstructural details are explicitly modelled.

As shown in Fig. 47(a), the MNS results obtained with a cross-triangle quadrilateral mesh are in perfect agreement with the (reference) DNS results, as confirmed by the little error for the peak load predicted by the two models (less than 1%). Conversely, the comparison between the MNS results with an unstructured mesh and the DNS results, shown in Fig. 47(b), highlights a little overestimation of the peak load (with an error of about 3%). Finally, Fig. 47(c) shows the MNS results obtained via a Single Interface Model, here considered for validating the adopted homogenization scheme in the frequent case of a priori known single crack path. The comparison with the DNS results highlights again a perfect agreement.

Therefore, it is important to note that the strength overestimation occurring in the case of unstructured meshes is not due to the adopted homogenization scheme, whose accuracy is fully validated by the outcomes reported in Fig. 47(a) and Fig. 47(c), but rather to the artificial crack path tortuosity induced by the DIM approach used at the macro-scale (please note the jagged crack path reported in Fig. 47(b)).

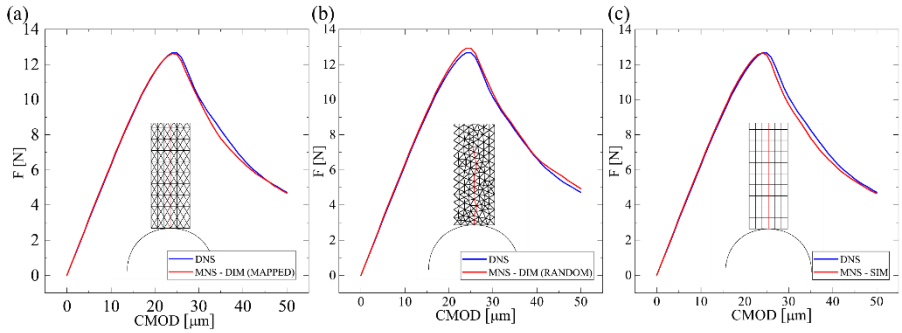

Fig. 47. Comparison between Direct Numerical Simulation (DNS) and Multiscale Numerical Simulation (MNS): Diffuse Interface Model with a mapped mesh (a), Diffuse Interface Model with a random mesh (b), and Single Interface Model (c).

3.2.2 Mixed-mode fracture test on an L-shaped composite panel

The second case study considered here is a mixed-mode fracture test performed on an L-shaped composite panel, widely studied in the literature for both homogeneous (see, for instance [125] and therein references) and heterogeneous [126] materials. The geometry and boundary conditions of this test are reported in Fig. 48, together with the unstructured mesh adopted for the Multiscale Numerical Simulations (MNSs). The same microstructure considered in the previous case study is assumed, and the same elastic and inelastic parameters reported in Table 3 and Table 4 are used.

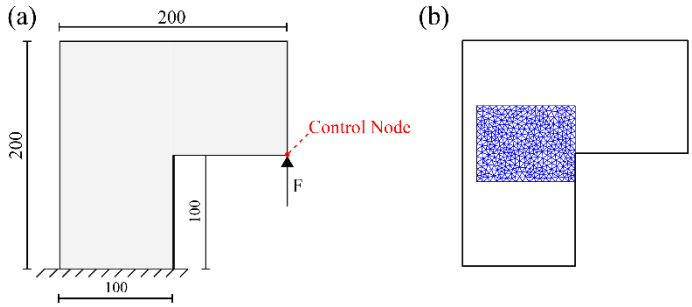

Fig. 48. L-shaped composite panel subjected to a mixed-mode fracture test: geometry and boundary conditions (a) and unstructured mesh used for Multiscale Numerical Simulation (b). All the dimensions are expressed in μm).

Fig. 49 shows the results of the Multiscale Numerical Simulation in terms of deformed configuration and first principal stress map at the final simulation step (Fig. 49 (a)) as well as of force-displacement curve (Fig. 49 (b)). Fig. 49(b) also shows a comparison with a Direct Numerical Simulation (DNS), performed on a fully meshed specimen. In particular, an overestimation of the peak strength and an underestimation of the post-peak strength are experienced. These discrepancies are probably due to a combined effect of the two following sources of error: (i) the mixed-mode fracture is totally neglected in the proposed nonlinear homogenization scheme; and (ii) the boundary layer effects, although being important in the considered geometry configuration, are not captured in the proposed multiscale approach. However, the resulting overall error on the peak load is fully acceptable from an engineering point of view, being of about 4%. These results confirm the reliability

of the proposed multiscale modeling approach also in the case of mixed-mode fracture conditions, at least in terms of global structural response.

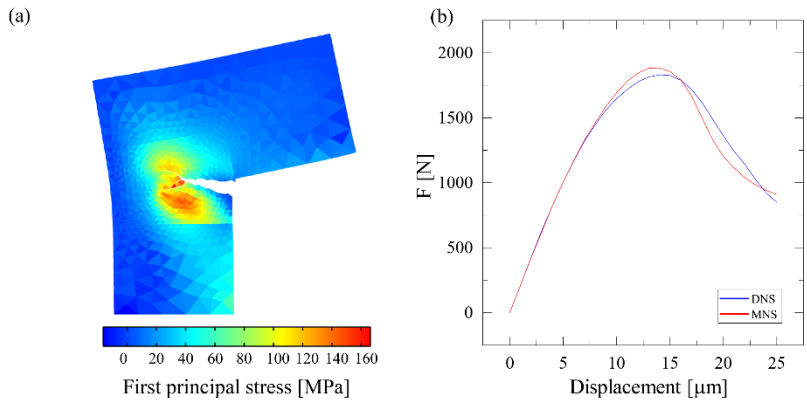

Fig. 49. Multiscale Numerical Simulation of the mixed-mode fracture test on a L-shaped composite panel: deformed configuration and first principal stress map at the final simulation step (a), and force vs displacement curve (b).

This novel hybrid cohesive/volumetric multiscale finite element model is proposed for performing efficient failure analyses of fiber-reinforced composite structures. Such a strategy adopts a Diffuse Interface Model (for the numerical simulation of multiple cracking at both micro- and macro-scales) used in conjunction with a continuous/discontinuous nonlinear homogenization scheme. The main advantage of this multiscale approach over more sophisticated ones is the adoption of very efficient operational steps to be performed within an off-line simulation stage.The present model has been applied for analyzing the failure of fiber-reinforced structures subjected to transverse cracking (including matrix cracking and fiber/matrix debonding). In particular, two case studies have been presented in this work, referring to Mode-I and Mixed-Mode fracture conditions, in order to demonstrate the versatility and the generality of the proposed approach. Furthermore, suitable comparisons with a fully detailed model have shown that the proposed multiscale strategy is very efficient from the computational point of view, while preserving a high numerical accuracy, in terms of both overall load-carrying capacity and average cracking pattern. In particular, the errors reported on the peak load were always less than 4%, thus being fully acceptable for engineering purposes.

Finally, in order to better understand the strength of the proposed multiscale approach, some details about the computational efficiency of the model, with reference to both the Mode-I and Mixed-Mode tests, are reported in Table 6, Table 7, Table 8.

Table 6. Comparison in terms of DOFs number for the Three-Point Bending (TPB) test

	DOFs number	Ratio
DNS (reference)	388,782	-
MNS (mapped)	2,492	0.64%

Table 7. Comparison in terms of DOFs number for the Mixed-Mode fracture test

	DOFs number	Ratio
DNS (reference)	1,266,126	-
MNS	8,753	0.69%

Table 8. Comparison in terms of simulation time for the Mixed-Mode fracture test

	Simulation time	Ratio
DNS (reference)	10h 56min 45s	-
MNS	7min 37s	86

In particular, Table 6 and Table 7 show the differences in terms of DOFs (Degrees of Freedom) number between the multiscale and the direct simulation, that has been took as reference, for the Three-Point Bending (TPB) and the Mixed-Mode (MM) test, respectively. Table 8, instead, highlights the differences in terms of simulation time for the Mixed-Mode fracture test performed on the L-shaped composite panel. These results clearly prove that the proposed model not only provides an accurate response in terms of load-deflection curves, but it is also computationally efficient. In fact, it can be seen that the present multiscale model leads to a significant reduction in the number of degrees of freedom, and, at the same time, to a notale increase in computational speed, thus resulting in a very effective prediction of the overall fracture responses under general loading conditions.

4. Non-linear analysis of load-induced degradation of vibration characteristics in structural elements

4.1 Numerical applications to RC beams

An investigation of the static and dynamic behavior of a reinforced concrete beam was performed comparing the numerical results with the experimental ones described by [127]. Based on the combination of DIM and ETM models, a numerical model is proposed and implemented using the finite element software COMSOL Multiphysics®. The proposed approach incorporates nonlinear springs to simulate the bond-slip mechanism between steel reinforcement bars and concrete and diffuse interface elements to simulate the nucleation of diffuse fractures in reinforced concrete structures. The geometry configuration, the material parameters and the cohesive law parameters were reported in Fig. 50, Table 9 and Table 10, respectively. The beam is restrained at both ends by supports consisting of highly stiffened plates used to spread the stress from the constraint reactions and by linear elastic springs simulating the elastomeric pads whose stiffness is equal 1.1x107 N/m.

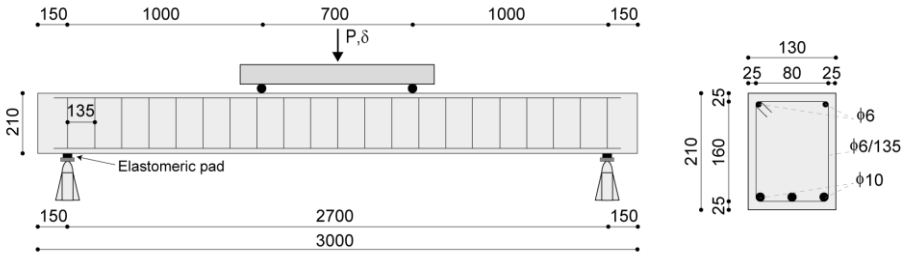

Fig. 50. Geometry configuration and boundary conditions of the four-point bending test investigated (all dimensions are expressed in mm).

Table 9. Material mechanical properties

Material	Young's modulus [GPa]	Poisson's ratio	Yield strength [MPa]	Compressive strength [MPa]	Traction strength [MPa]
Concrete	40.3	0.2	-	36.5	2.10
Plain steel ø6	210	0.30	393.6	-	-
Ribbed steel ø10	210	0.30	490	-	-

Table 10. Parameters of the proposed cohesive law.

K_n^0	K_s^0	t_n^c	t_s^c	G_I^c	G_{II}^c	β
[N/m³]	**[N/m³]**	**[MPa]**	**[MPa]**	**[N/m]**	**[N/m]**	
1.3162e14	1.3162e14	2.1	4.2	150	1500	225

As a numerical result of the proposed nonlinear model, the load-deflection curve (Fig. 51) during the loading process (blue curve) exhibits a typical trilinear behavior, in which two slope variations are markedly observed, coinciding with the beginning of the main fractures in concrete (point A) and the yielding of the tension reinforcing longitudinal bars (point B). We observed a slight variation between the numerical and experimental results from 0 to 4 mm of deflection, where the numerical model highlighted a slightly stiffer structural response due to the common toughening effect induced by the DIM which is discussed in depth in the following scientific papers [128–130].

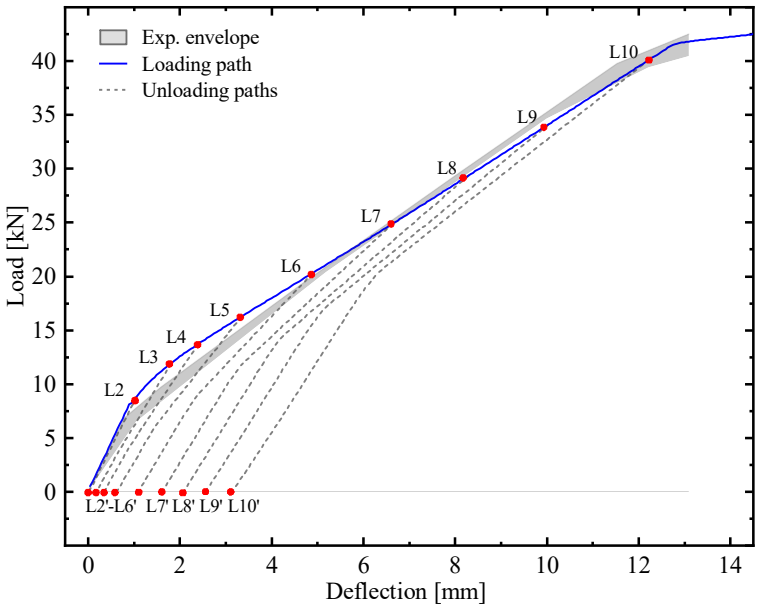

Fig. 51. Load versus mid-span deflection curves compared with the envelope of the experimental results during the loading and unloading phase.

In addition, ten damage levels, corresponding to a percentage of the maximum load level which is equal to 42.1 kN, were identified and listed in Table 11 based on the data reported in [127]. For each level of damage, an unloading process was performed, and the obtained load-deflection curve is reported in Fig. 51 by means of a gray dashed line with the exception of the first level of damage L1 corresponding to the undamaged configuration.

Table 11. Percentage of maximum load ("Max Load %") associated with the investigated damage levels ("damage level").

Damage level	L1	L2	L3	L4	L5	L6	L7	L8	L9	L10
Max. Load %	0	15.90	22.73	27.87	35.10	47.27	59.17	71.13	83.43	95.07
Load [kN]	0	6.69	9.58	11.6	14.7	19.9	24.9	29.9	35.1	40

Subsequently, a modal analysis was carried out by superimposing a linearized eigenvalue problem over the solution of the quasi-static analysis. The modal analysis, giving the natural vibration frequencies of the damaged beam, was superimposed on the static solution at the unloading phase (Points L1'-L10') to consider the effects of partially closed cracks caused by contact phenomena. As can be seen in Fig. 52, the obtained natural vibration frequencies, expected to be influenced by the presence of diffuse damage, were normalized with respect to the frequencies related to the undamaged configuration. The normalized frequencies were plotted as a function of the levels of damage and compared with the experimental envelope reported in [127]. For the first and fourth natural vibration modes, the numerical and experimental results are in perfect agreement. However, a slight difference was detected in high-order natural vibration modes (6^{th} and 7^{th} modes), because they are typically most affected by measurement and dispersion errors. The highest deviation is less than 5% and it has been detected at highest damage level for the 7^{th} modes, but considering the experimental uncertainties given by the high-order natural vibration mode, is still an acceptable deviation. The curve trends highlighted that the investigated natural vibration modes show a decreasing trend with three different slopes: the slope that occurs between the percentage failure load 0% and 15% is slight, the slope that occurs between 15% and 50% is considerable, and the slope that occurs between 50% and 95% remains similar to the first.

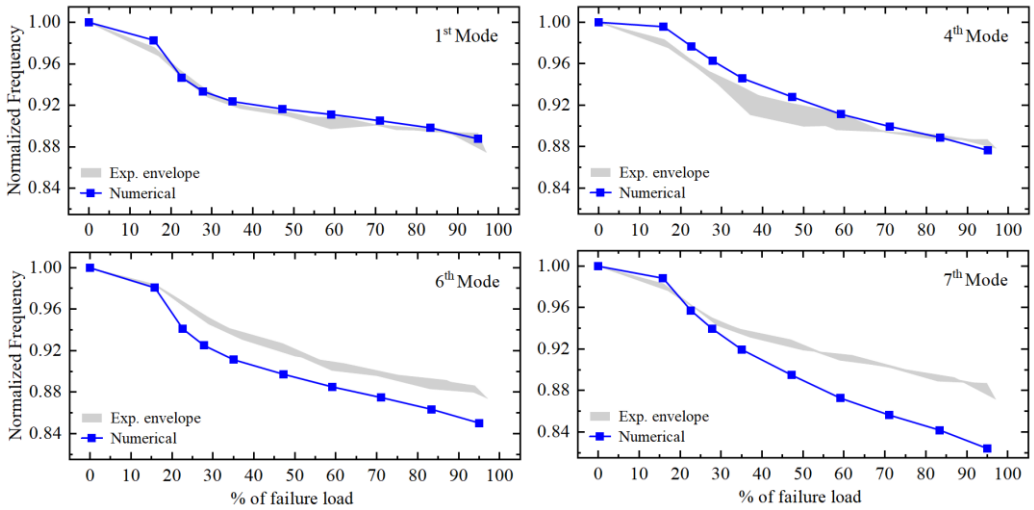

Fig. 52. Normalized natural vibration frequencies of the modes 1, 4, 6, and 7 compared with the envelope of the experimental data.

In order to evaluate the correlation between the modal shapes in the undamaged configuration L1' with those in damaged ones L2'-L10', the MAC coefficients [131] were evaluated and reported in Table 12. The coefficients were determined by using the following expression:

$$MAC_{ij} = \frac{\left(\boldsymbol{\varphi}_{i,0}^{T}\boldsymbol{\varphi}_{j,d}\right)^{2}}{\left(\boldsymbol{\varphi}_{i,0}^{T}\boldsymbol{\varphi}_{i,0}\right)\left(\boldsymbol{\varphi}_{j,d}^{T}\boldsymbol{\varphi}_{j,d}\right)} \tag{66}$$

It has been applied to mode shapes normalized with respect to the mass matrix and evaluating the displacements relating to mode 1, 4, 6, 7 and 8 along the top of the beam at 51 points equally spaced to each other 60 mm. It is worth noting that, as the level of damage increases, the correlation between the mode in the undamaged configuration and that relating to the damaged configuration decreases, as a consequence of the fact that the values of the diagonal coefficients of the MAC matrix (MAC_{ii}), deviate more from the unit value as the damage level increases. These deviations are not particularly relevant, in fact, the relative maximum percentage deviation measured is equal to 2.11% corresponding to the level of damage L10 ' for the 8th mode.

Table 12. MAC indicator evaluated for the different damage levels and with reference to the undamaged configuration.

L1'-L1'				
1.0000	0.0128	0.0000	0.0010	0.0024
0.0128	1.0000	0.0234	0.0047	0.0264
0.0000	0.0234	1.0000	0.0976	0.0320
0.0010	0.0047	0.0976	1.0000	0.4032
0.0024	0.0264	0.0320	0.4032	1.0000

L1'-L2'

0.9999	0.0123	0.0000	0.0008	0.0026
0.0145	0.9997	0.0208	0.0052	0.0290
0.0000	0.0254	0.9998	0.1039	0.0398
0.0011	0.0037	0.0942	0.9990	0.3801
0.0024	0.0261	0.0347	0.4161	0.9985

L1'-L3'

0.9989	0.0109	0.0000	0.0006	0.0024
0.0180	0.9973	0.0166	0.0054	0.0341
0.0000	0.0262	0.9981	0.1235	0.0441
0.0011	0.0018	0.0869	0.9945	0.3524
0.0025	0.0240	0.0418	0.4001	0.9933

L1'-L4'

0.9984	0.0102	0.0000	0.0007	0.0022
0.0191	0.9959	0.0159	0.0047	0.0357
0.0000	0.0253	0.9972	0.1339	0.0389
0.0011	0.0013	0.0849	0.9919	0.3577
0.0025	0.0231	0.0448	0.3740	0.9924

L1'-L5'

0.9980	0.0096	0.0000	0.0007	0.0020
0.0199	0.9952	0.0162	0.0034	0.0363
0.0000	0.0242	0.9966	0.1436	0.0315
0.0012	0.0011	0.0834	0.9877	0.3717
0.0026	0.0227	0.0476	0.3432	0.9919

L1'-L6'

0.9977	0.0091	0.0000	0.0008	0.0019
0.0204	0.9952	0.0169	0.0021	0.0364
0.0000	0.0235	0.9965	0.1497	0.0270
0.0012	0.0011	0.0834	0.9836	0.3792
0.0027	0.0228	0.0484	0.3231	0.9906

L1'-L7'

0.9975	0.0089	0.0000	0.0008	0.0019
0.0208	0.9956	0.0173	0.0017	0.0357
0.0000	0.0239	0.9969	0.1471	0.0262
0.0012	0.0014	0.0854	0.9839	0.3690
0.0027	0.0232	0.0468	0.3264	0.9887

L1'-L8'

0.9972	0.0086	0.0000	0.0008	0.0019
0.0215	0.9953	0.0168	0.0017	0.0356
0.0000	0.0247	0.9969	0.1455	0.0260
0.0012	0.0014	0.0863	0.9839	0.3594
0.0027	0.0232	0.0460	0.3298	0.9858

L1'-L9'

0.9968	0.0083	0.0000	0.0009	0.0019
0.0221	0.9948	0.0162	0.0018	0.0352
0.0000	0.0253	0.9965	0.1465	0.0242
0.0012	0.0014	0.0858	0.9825	0.3552
0.0028	0.0230	0.0466	0.3267	0.9829

L1'-L10'

0.9962	0.0077	0.0000	0.0009	0.0019
0.0231	0.9937	0.0161	0.0021	0.0350
0.0000	0.0258	0.9960	0.1439	0.0225
0.0012	0.0012	0.0855	0.9805	0.3489
0.0028	0.0228	0.0478	0.3253	0.9789

In Fig. 53, the Curvature Damage Factor (CDF) [132] normalized with respect to the CDF which is related to the highest damage level (L10') has been investigated. Such indicator was determined by summing the absolute variations of the Modal Curvatures (evaluated in fifty points placed on the whole length of the top beam and equally spaced) between the undamaged configuration L1' and the other investigated damage levels L2' - L10' over all the investigated mode shapes. The expression used for the CDF is the following one:

$$CDF_i = \frac{1}{N}\sum_{j=1}^{N}\left|\varphi_{ij,0}'' - \varphi_{ij,d}''\right| \tag{67}$$

where the modal curvature is defined by means of the central difference method:

$$\varphi_{ij}'' = \frac{\varphi_{(i+1)j} - 2\varphi_{ij} + \varphi_{(i-1)j}}{h^2} \tag{68}$$

It will be noted that, at the undamaged configuration (L1'), the CDF is equal to zero, but it oscillates for the subsequent damage levels, indicating the presence of damage localization. The obtained curves show several peaks in the center of the steel-reinforced concrete beam whose intensity is related to the damage level and therefore to the fracture length. Furthermore, the CDF indicator was shown to be heavily affected by the local effect caused by the loads and stiff plates. In fact, we can see noise in the oscillatory trend of the CDF in these beam zones.

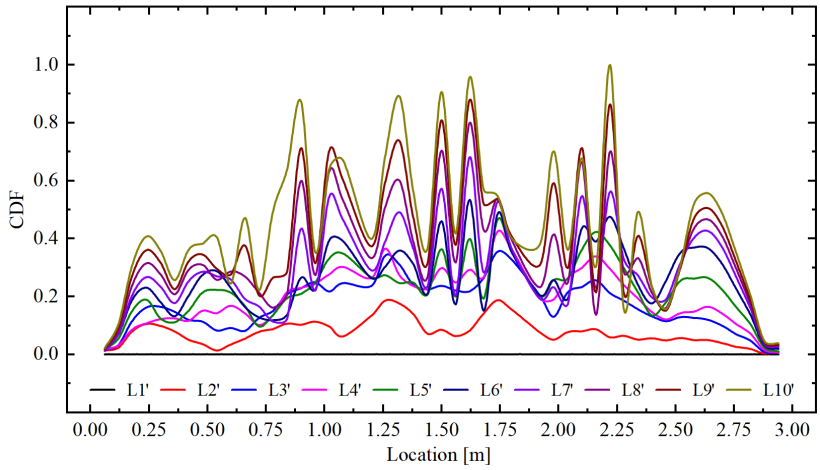

Fig. 53. Curvature Damage Factor (CDF) evaluated for the mode shapes 1, 4, 6, and 7 for all the investigated damage levels during the unloading phase.

4.2 Damage effects on FRP-strengthened RC elements

In this section, the proposed model has been employed to analyze the static and dynamic structural response of FRP-plated RC beams whose geometry and material properties have been illustrated in Section 4.1.

From a computational point of view, the adopted theoretical approach described in Chapter 2 of this thesis, has been implemented in a commercial finite element software COMSOL Multiphysics® [133] and needs a preprocessing operation aimed to build a cohesive/volumetric FE mesh. To this end, after generating an unstructured 2D mesh, consisting of three-node triangular elements arranged according to a Delaunay tessellation, the planar bulk elements must be separated by duplicating every common node shared by each pair of bulk elements. Such operation requires a nodal connectivity updating and explicit slit conditions must be imposed on the displacement field along the interior boundaries of the FE mesh. Finally, four-node zero-thickness cohesive elements can be inserted between the opposite faces of all neighboring bulk elements, allowing them to be interconnected. The numerical 2D model adopts a plane stress condition allowing to predict accurate numerical results compared to a full 3D analysis when a relatively small thickness (with respect to the other dimensions), and free lateral boundary conditions are involved. Moreover, linear shape functions for the displacement field have been adopted for the analyses. It is worth noting that, the FRP reinforcement system, consisting of composite plate and adhesive layer, has been modeled by means of four-node quadrilateral elements which behave in a linearly elastic isotropic manner, meaning that the FRP rupture is not considered.

The model has been first validated by performing a numerical analysis of the control RC beam (beam without the FRP reinforcement). A comparison between the numerically obtained results and the experimental ones, in terms of loading curves, crack patterns, and natural frequency degradation was reported in Section 4.1. Secondly, the model is adopted to perform static and dynamic analyses of an FRP-plated RC beam. The numerically obtained results, reported in the following, have allowed an accurate damage detection, in terms of damage magnitude and location, by using the most common dynamic damage indicators.

4.2.1 Geometric and material properties

The numerical analyses involved an FRP-strengthened RC beam subjected to a four-point bending test whose geometry and boundary conditions are depicted in Fig. 54(a). The same beam but without the FRP reinforcement, denoted in this work as “control beam”, has been experimentally analyzed by [134] and will be numerically simulated to validate the proposed strategy for damage identification. The mechanical properties of concrete and steel rebars are taken from [134]. In particular, the RC beam is made up of concrete with a compressive strength of 36.5 MPa, Young’s

modulus of 40.3 GPa, and tensile strength of 2.1 MPa. The steel reinforcement consists of 10 mm ribbed bars and 6 mm plain bars used in the tension and compression side of the beam, respectively, and 6 mm plain stirrups diffuse over the whole beam length with a uniform spacing of 135 mm (further details in Fig. 54(a)). The adopted steel possesses Young's modulus of 210 GPa and yield strength of 490 MPa for ribbed bars and 393.6 MPa for plain bars. The strengthening system adopts a carbon FRP (CFRP) plate made of four composite layers with an overall thickness equal to 0.44 mm, externally bonded to the soffit surface of the beam by using a 2 mm thick epoxy adhesive (see the cross-section of the beam reported in Fig. 54(a). The Young's modulus of the employed CFRP plate and epoxy is equal to 235 GPa and 1 GPa, respectively. A high tensile strength equal to 4200 MPa is experimentally obtained by the CFRP plate.

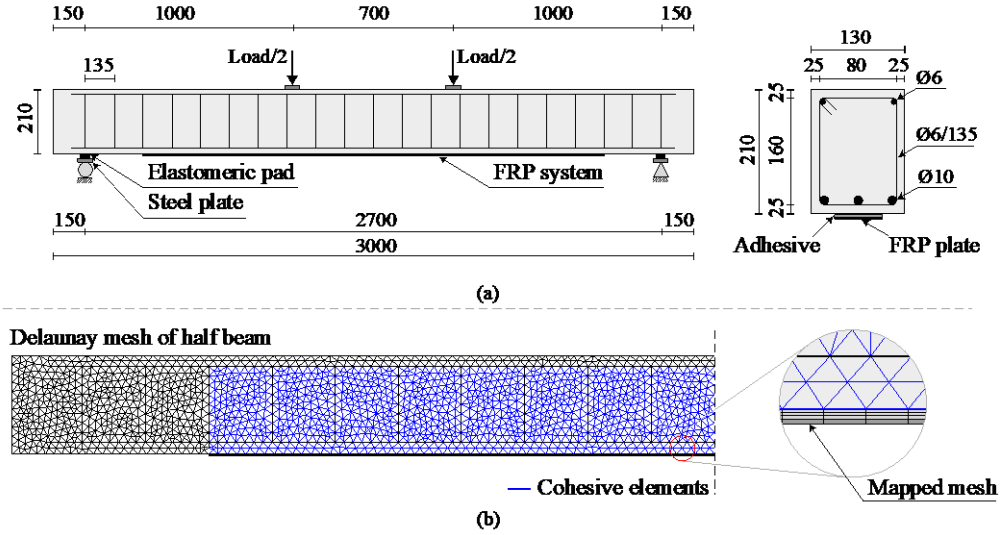

Fig. 54. Tested beam: geometry and boundary conditions (a) and adopted discretization (b).

The concrete beam is discretized by 2D three-node triangular elements arranged by means of a Delaunay tessellation, while 1D two-node elements are employed to steel rebars. A mapped mesh, with four-node quadrilateral elements, is performed to discretize the strengthening system. All adopted finite elements have a maximum size of 20 mm (Fig. 54(b)). It is worth noting that, the supports of the tested beam are characterized by square steel plates ($200 \times 200 \times 20$ mm), useful to spread the stress of the constraints reactions, and by elastomeric pads ($180 \times 50 \times 25$ mm) located between the plates and the beam. Such elastomeric pads are modeled by linear elastic springs with stiffness equal to 1.1×10^7 N/m derived by a linear fit performed on the experimental load–displacement compression relationship reported in [134]. Fig. 54(b) shows the cohesive interface elements (highlighted by blue lines) located along the mesh boundaries within the wide zone dominated by the flexural/shear stress state. As explained in Section 2.1 of the present thesis, such

interface elements are equipped by a traction-separation law whose cohesive parameters are taken in accordance with the data reported in [134] and listed in Table 13.

Table 13. Cohesive parameters required by the adopted traction-separation law.

K_n^0	K_s^0	t_n^c	t_s^c	G_I^c	G_{II}^c	β
[N/m³]	**[N/m³]**	**[MPa]**	**[MPa]**	**[N/m]**	**[N/m]**	
1.3162e14	1.3162e14	2.1	4.2	150	1500	225

However, the Mode-II fracture parameters, i.e. critical tangential stress t_n^c and fracture energy G_{II}^c, are not available in the reference work [134] and therefore calibrated according with the numerical work of [120]. Moreover, the cohesive parameters of the elements inserted along the FRP/concrete interface are assumed equal to those employed in the concrete phase, implicitly assuming that the debonding failure occurs at the concrete side of the material interface.

4.2.1.1 Validation of the proposed model

In this section, the results of the static and dynamic tests performed on the control beam (without FRP reinforcement) have been reported and compared with the experimental outcomes of [134] in order to assess the validity of the proposed fracture model.

4.2.1.2 Static analysis of the control beam

Quasi-static numerical simulations have been performed under a plane stress state and adopting a Newton-Raphson solution algorithm in combination with a displacement control scheme with increments of 5E-2 mm. According to the experimental test, the analysis is stopped after which the yielding phase of the steel rebars has been reached, considering the corresponding load level, of about 42.5 kN, as the ultimate load of the beam. At predefined load levels, expressed as a percentage of the ultimate load and denoted as L_n (with n the load level number), an unloading process has been simulated until the applied force system reaches a value close to 0. The percentage values of the different load levels as taken in accordance with the experimental ones reported in [134]. The related loading and unloading equilibrium paths together with the experimental envelope have been depicted in Fig. 55(a). The loading phase is characterized by the well-known trilinear behavior of an RC beam, consisting of the linearly elastic, the crack propagation, and the rebars yielding stages, and results to be coherent with the experimental outcomes. Residual plastic deformations are observed after performing unloading processes (dashed red lines in Fig. 55(a)) for each predefined load level, showing, especially for high values of damage (from L6 to L10), two different slopes in the equilibrium path mainly induced by the combined effect of the concrete plasticity and the partial

contact between crack faces which cannot completely close due to the presence of the aggregates and the sliding phenomena occurring at the concrete/rebar interface. Such a result was confirmed by the deformed configurations reported in Fig. 55(b) which show the crack pattern and σ_{xx} concrete stresses at the initial and final point of the last unloading path corresponding to the L9 load level. As a matter of fact, the deformed configurations show cracks partially closed with respect to those observed at the initial point of the unloading path, thus highlighting the good capabilities of the proposed model to predict the complex mechanical behavior, including crack propagation, concrete plasticity, and contact effect of reinforced concrete beams subjected to loading and unloading cycles.

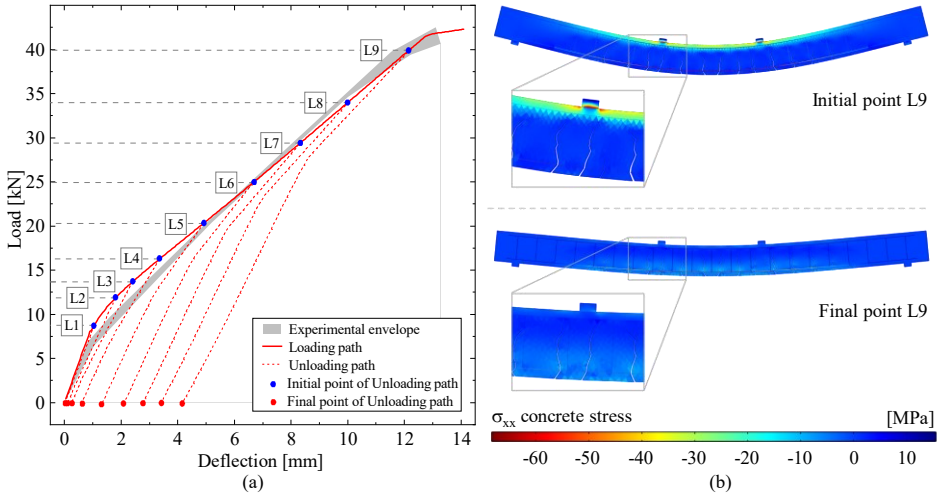

Fig. 55. Numerical results of the quasi-static analysis: loading curve (a) and deformed configurations of the last damage level L9 (b).

4.2.1.3 Dynamic analysis of the control beam

Subsequently to the static analysis, which allowed the diffuse damage in the RC control beam to be correctly simulated, a linearized eigenvalue problem of the structure has been solved by performing the analysis of small amplitude free oscillations superimposed on the damage scenarios previously obtained at the final points of each unloading path (see Fig. 55(a)), thus allowing to take into account the damage and plasticity effects of the concrete as well as the contact phenomena effect due to partial closure of the fully developed cracks.

Fig. 56 reports the outputs of the performed modal analysis, in terms of natural frequencies and modal shapes.

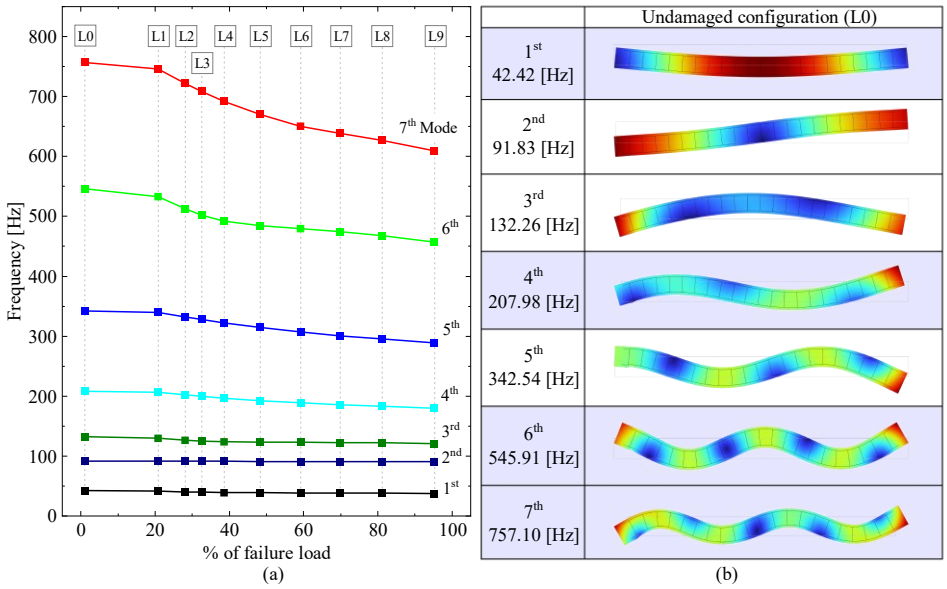

Fig. 56. Numerical results of the modal analysis: degradation of the natural frequencies as the damage level increases (a) and the first seven modal shapes of the undamaged configuration (b).

In particular, Fig. 56(a) shows the damage-induced degradation of the first seven natural frequencies for the different percentage values of the ultimate load, defined in Section 4.2.1.2, with respect to the natural frequencies numerically obtained in the undamaged configuration (L0). We can note that the natural frequencies of the high-order modal shapes are most affected by the damage evolution, showing higher percentage variations of the frequencies than the low-order ones. Moreover, for each modal shape order, the typical trilinear trend consisting of three different slopes is observed. In particular, from 20% to up to 60% of the ultimate load, a considerable reduction of the natural frequencies is predicted by the numerical model, due to the fact that this load level range is characterized by a fast evolution of the damage. Before and after this range, corresponding to the initial nonlinear behavior and quasi-completely propagated cracks stage, respectively, a slight decrease in the natural frequencies is detected. Fig. 56(b) shows the corresponding modal shapes of the undamaged configuration. It is worth noting that only the 1st, 4th, 6th, and 7th vibration modes, highlighted with blue color in Fig. 56(b), exhibit purely bending behavior and they will be investigated by virtue of their correspondence with those experimentally obtained [134] in terms of frequency and mode shapes. The frequency values f_i and the percentage frequency variation, of the chosen modal shapes are reported in Table 14. We can note that for each vibration mode the percentage variation of the natural frequencies increases as the damage level increases, providing values higher than 14% for the sixth and seventh modal shapes. However, in the first damage levels (until L5) a clear trend of the frequency variation between the different modal shapes is not detected and oscillating variation values are predicted. After damage level L5, the high-order vibration modes show significant frequency degradations with respect to the low-order ones, reaching a maximum

value of about 19.49% corresponding to the seventh modal shape at the last damage level, thus resulting to be the most affected by the damage evolution.

Table 14. Variation of the natural frequencies of the control beam as the damage level increases

	f_1 [Hz]	v_{f1} [%]	f_4 [Hz]	v_{f4} [%]	f_6 [Hz]	v_{f6} [%]	f_7 [Hz]	v_{f7} [%]
Undamaged	42.43	-	207.98	-	545.91	-	757.10	-
L1	41.52	2.15	206.80	0.57	532.90	2.38	746.03	1.46
L2	40.06	5.58	202.58	2.59	512.51	6.12	721.88	4.65
L3	39.63	6.59	199.91	3.88	502.40	7.97	708.67	6.40
L4	39.25	7.48	196.27	5.63	492.35	9.81	692.15	8.58
L5	38.91	8.28	192.24	7.57	484.65	11.22	669.91	11.52
L6	38.66	8.88	188.60	9.32	479.92	12.09	649.94	14.15
L7	38.28	9.77	185.72	10.70	474.75	13.04	638.76	15.63
L8	37.89	10.69	183.45	11.79	467.52	14.36	626.68	17.23
L9	37.17	12.39	180.06	13.42	456.78	16.33	609.54	19.49

Finally, in order to fully validate the implemented numerical procedure, a comparison with the experimental results reported in [134] has been carried out. Fig. 57(a) shows the numerically and experimentally obtained natural frequencies of the first modal shape order for the different damage levels, while in Fig. 57(b) the corresponding modal shapes at the first and the last damage level, are reported. The good agreement between numerical and experimental results highlights the effectiveness of the proposed model in simulating the damage effects on the dynamic response of the RC structures.

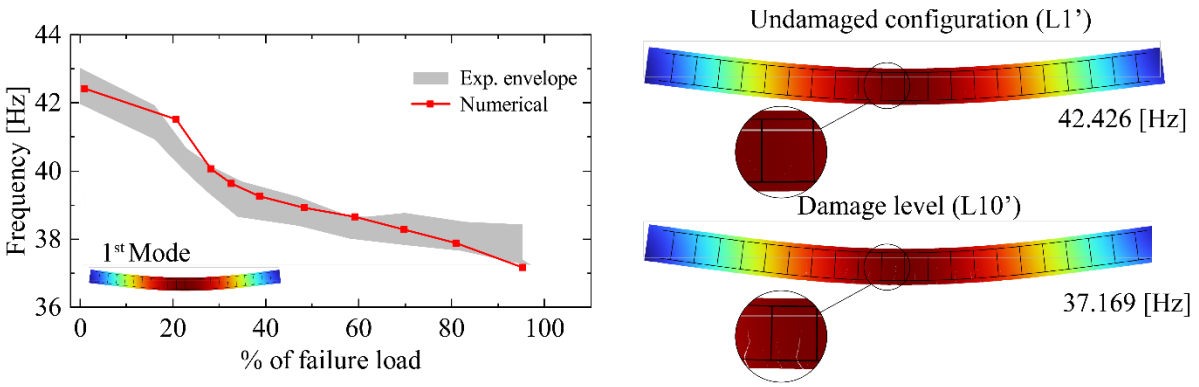

Fig. 57. Comparison between experimental and numerical results (a) and the corresponding modal shapes at damage levels L1 and L9.

4.2.1.4 Damage identification in the FRP-plated RC beams

The proposed numerical procedure has been here employed to investigate the damage effects on both static and dynamic response of strengthened RC structures. In particular, the FRP-plated RC beam described previously is analyzed by following 3 different steps:

a) Numerical simulations of the structure under monotonic and cyclic quasi-static loading conditions to evaluate the load-carrying capacity, crack patterns, and failure mode (Section 4.2.1.5);
b) Modal analysis for each selected damage level to acquire the dynamic properties, in terms of natural frequencies and modal shapes, during the damage evolution (Section 4.2.1.6);
c) Application of available dynamic indicators to detect the damage magnitude and location in the tested FRP-plated RC beam (Section 4.2.1.7).

4.2.1.5 Static analysis of the strengthened RC beam

Quasi-static numerical simulations have been performed under a plane stress state and displacement-controlled loading conditions adopting a displacement increment equal to 5E-2 mm. Fig. 58 shows the predicted loading path of the tested control (scatter line) and strengthened (red line) beams. As widely known, the FRP-plated RC beam predicts a stronger structural response compared to the control one showing a considerable increase of dissipated energy from the rebar yielding stage, (Point A of Fig. 58) until the peak load (Point B of Fig. 58) whose predicted value is about 69.42 kN. After that, the predicted structural response becomes unstable, due to the catastrophic evolution of the FRP debonding phenomenon, and the load drops to a residual value corresponding to the load-carrying capacity of the beam without the strengthening effect of the FRP plate. It is worth noting that, the combined work of the adopted cohesive interface model and embedded truss model, to simulate concrete and rebar mechanical behavior, respectively, allows an accurate prediction of the damage, in terms of global stiffness reduction and crack pattern, as well as the failure modes, which is a fundamental feature for the model-based damage detection procedures. As previously performed in the static analysis of the control beam, unloading processes have been simulated by decreasing the load level down to 0 kN. For comparison purposes, in this case, the load levels from which the unloading processes start, coincide with that defined for the control beam (from L1 to L9), but three new load levels (L10, L11, and L12), corresponding with the rebar yielding and peak loads and an intermediate load level between them (yielding and peak loads), are added in order to capture the effects of rebar plasticity and the partial debonding phenomena which occur at the concrete/FRP interface. As a matter of fact, before the rebar yielding stage, lower residual plastic deformations are predicted compared with the control beam ones because of the strengthening contribution of the FRP system on the global structural stiffness of the beam, while after this stage, significant permanent deformations are detected. Moreover, in addition to the concrete plasticity and the contact effect of

the partially closed crack faces, these high values of permanent deformations are induced by the plasticity of the FRP/concrete bonding adhesive, predicted in the proximity of the partial debonding where important sliding displacements occur, and suitably captured by the improved traction-separation law adopted for the cohesive elements inserted in the FRP/concrete material interface.

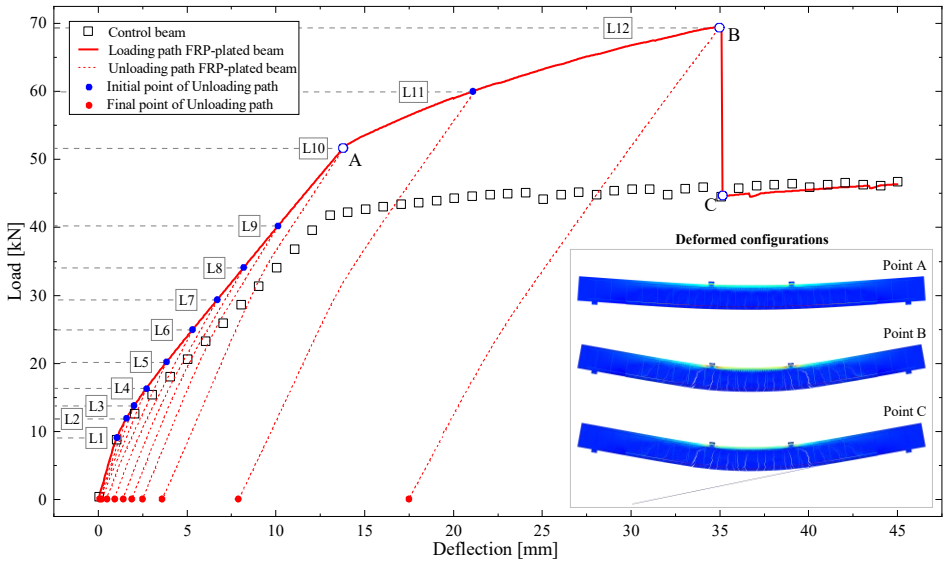

Fig. 58. Global structural response of the FRP-plate RC beam.

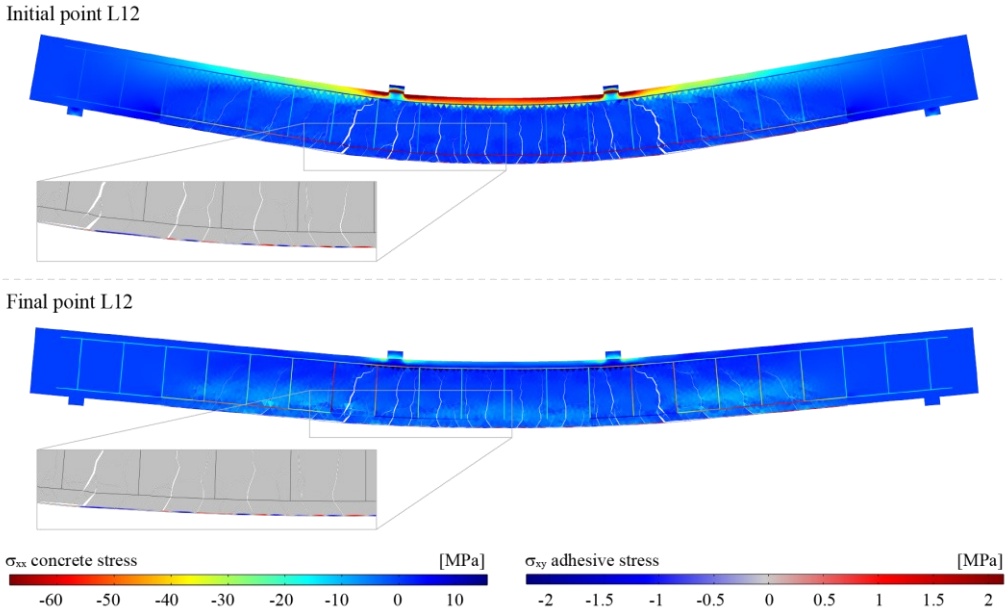

Fig. 59. Deformed configurations and stress maps at the initial and final points of the unloading path L12.

This behavior is confirmed by the deformed configurations at the initial and final points of the last unloading path L12, reported in Fig. 59, showing the partially closed cracks phenomena and the high shear stresses of the adhesive around both crack mouths and partially propagated debonding.

4.2.1.6 Dynamic analysis of the strengthened RC beam

A modal analysis on the FRP-plated RC beam has been performed by solving a linearized eigenvalue problem superimposed on the static solutions obtained at the final points of each unloading path (L1-L12 of Fig. 58). The dynamic response of the strengthened RC beam, in terms of natural frequencies and modal shapes, has been focused on the pure bending modes in order to perform a correct comparison with the dynamic outcomes obtained by the control beam. To this end, the 1st, 4th, 6th, and 7th vibration modes are chosen for the present investigation. Fig. 60 shows the numerically obtained natural frequencies normalized with respect to the undamaged configuration ones and the comparison with the dynamic results previously obtained by the control beam. Similarly to the control beam results, a reduction of the natural frequencies as the load level increases is observed in the dynamic response of the strengthened RC beam. This reduction, until the yielding load of about 51.63 kN, follows the typical trilinear trend, already detected in the control beam (Section 4.2.1.3) and experimental evidence reported in [134,135]. In particular, these three detected slopes correspond to the elastic stage, the crack formation stage, characterized by a fast evolution of the nonlinear damage processes, and the stabilized cracking stage of the static structural response of the tested beam. After yielding load, where significant damage effects arise, mainly induced by both nonlinear crack processes in concrete, rebar yielding, and partial debonding in FRP/concrete interface, the frequencies drop with a steeper slope up to peak load. This trend can be observed in each natural vibration mode investigated (see Fig. 60).

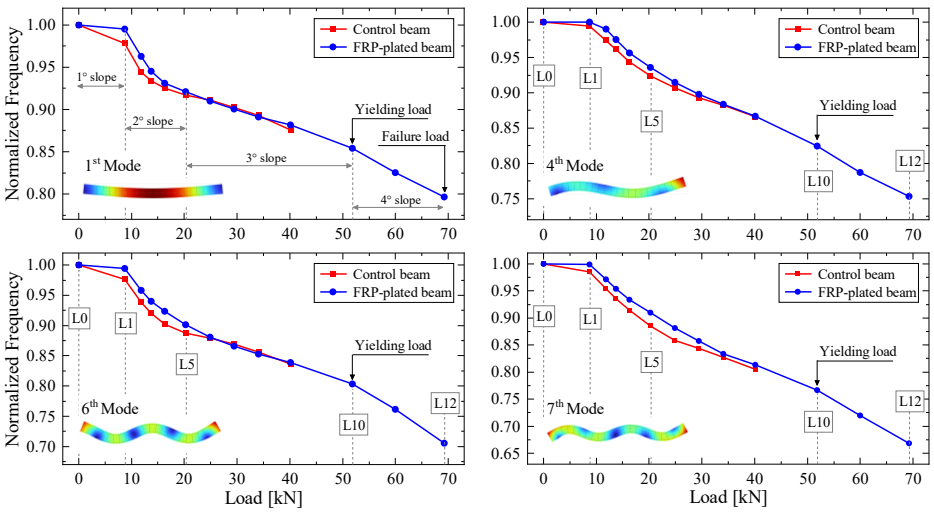

Fig. 60. Degradation of the 1st, 4th, 6th, and 7th mode natural frequencies of the control and strengthened RC beam as the load level increases.

The percentage frequency variations of the FRP-plated beam, at the load levels where the changes of slope occur, i.e., L1, L5, L10 (yielding load), and L12 (failure load), results to be respectively equal to 0.45 %, 7.91%, 14.57, and 20.37% for the first mode, 0.01%, 6.42%, 17.53%, and 24.70% for the

fourth mode, 0.55%, 9.84%, 19.68% and 29.48% for the sixth mode, and 0.15%, 9.02%, 23.33%, and 33.11% for the seventh mode. We can note that the damage mainly affects the natural frequency of the high-order vibration modes (sixth and seventh modes) providing percentage degradations higher than 9% immediately after the initial crack formation stage. In the structural health monitoring framework, this value could be taken as a damage threshold after which serious structural damage phenomena can occur in the monitored structure. For a full understanding, all values of the frequency variations for the chosen vibration modes as the damage level increases are reported in Table 15.

Table 15. Variation of the natural frequencies of the strengthened RC beam as the damage level increases.

	f_1 [Hz]	v_{f1} [%]	f_4 [Hz]	v_{f4} [%]	f_6 [Hz]	v_{f6} [%]	f_7 [Hz]	v_{f7} [%]
Undamaged	42.44	-	208.90	-	546.83	-	758.91	-
L1	42.25	0.45	208.88	0.01	543.81	0.55	757.74	0.15
L2	40.87	3.70	206.92	0.95	523.80	4.21	737.48	2.82
L3	40.12	5.47	203.77	2.46	514.00	6.00	724.23	4.57
L4	39.51	6.91	199.74	4.39	505.09	7.63	708.44	6.65
L5	39.08	7.91	195.49	6.42	493.04	9.84	690.43	9.02
L6	38.63	8.97	191.14	8.50	481.82	11.89	669.27	11.81
L7	38.23	9.92	187.57	10.21	473.54	13.40	650.49	14.29
L8	37.83	10.86	184.61	11.63	466.54	14.68	632.83	16.61
L9	37.42	11.83	181.14	13.29	458.90	16.08	617.31	18.66
Ll0	36.26	14.57	172.29	17.53	439.21	19.68	581.83	23.33
L11	35.04	17.44	164.45	21.28	416.33	23.87	546.18	28.03
L12	33.79	20.37	157.31	24.70	385.65	29.48	507.60	33.11

Moreover, Fig. 60 shows a comparison of the frequency degradation obtained by the control and FRP-plated beam. Lower frequency degradation values are observed in each chosen vibration mode of the strengthened RC beam with respect to the control beam ones. This behavior can be mainly appreciated in the initial stages of the analysis, i.e., within the load range L1-L5, where the frequency degradation values, regarding the first vibration mode of the strengthened RC beam, are lower than 48% and 5% for the load levels L1 and L5, respectively, with respect to those obtained by the control beam. The remaining vibration modes follow the same descending trend as the load level increases, but higher percentage values are recorded. This beneficial effect on the frequency degradation predicted by the strengthened RC beam is mainly induced by the FRP reinforcement system which obstructs the crack opening and delays the damage process evolution in the structure. However, after

load level L5 the frequency degradation values align with the control beam ones, especially in the first and sixth vibration modes (see Fig. 60). This behavior is justified by the diffuse damage effect in the concrete phase, including flexural and shear micro- and macro-cracks, provided by the application of the FRP-plate, which despite obstructs the crack opening, avoids the localization of the damage in narrow bands of the structure. As a matter of fact, the crack patterns predicted by the control and strengthened RC beams in the static analysis at the stabilized cracking stage (see deformed configurations reported in Fig. 55 and Fig. 58) are characterized by localized large-width cracks and diffused narrow-width cracks, respectively.

4.2.1.7 Dynamic damage detection indicators

In this section, the common dynamic damage indicators, available in the technical literature [131,132], have been employed to assess their capability in damage detection of strengthened structures. It is worth highlighting that the natural frequency variation, previously reported in Section 4.2.1.6, is often used as a damage indicator in terms of damage magnitude. Now, the damage indicators based on the modal curvatures, i.e., Modal Curvature (MC) and Curvature Damage Factor (CDF), were used to detect the position of the damage in the monitored structure. The expressions used for the damage indicators are the same as reported in Section 4.2.1.3. Moreover, the comparison with the crack patterns obtained in the static analysis will allow a suitable evaluation of the predictive capabilities of the proposed model-based damage detection method regarding the strengthened structures.

The modal curvatures have been computed considering 47 points, 60 mm equally spaced, distributed along the upper side of the monitored beams (see the blue points in Fig. 61). It is worth noting that in the proximity of load application points, to avoid inconsistent curvature values induced by the large deformations occurring in these zones, no points were counted and the distance between the two consecutive points has been set equal to 120 mm.

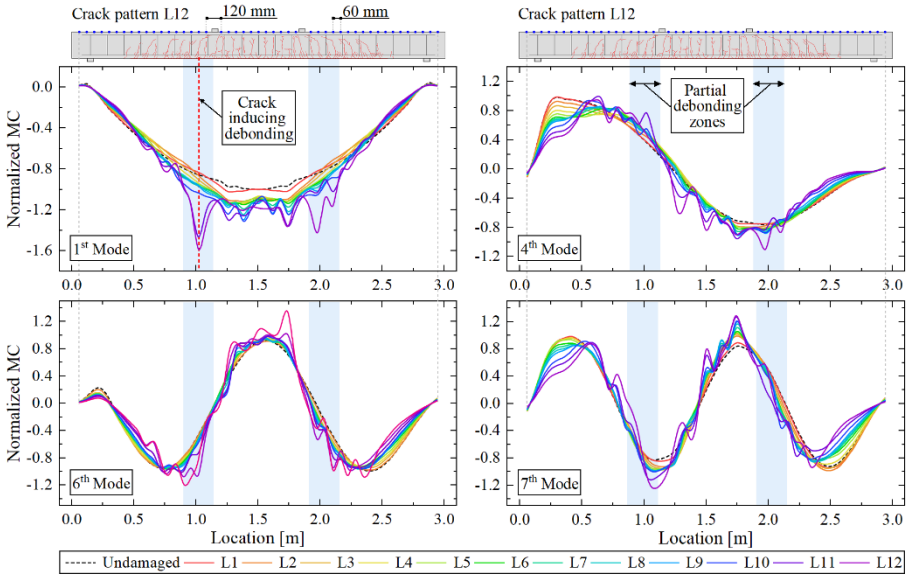

Fig. 61. Modal Curvature of the first, fourth, sixth, and seventh modes at different load levels.

Fig. 61 shows the MCs of the chosen vibration modes (1st, 4th, 6th, and 7th) obtained by the dynamic analyses on different damage scenarios (L1-L12 reported in Fig. 58), normalized with respect to the maximum value recorded for the investigated modal shape in the undamaged configuration. In addition, the crack pattern of the strengthened beam predicted at the load level L12, after which debonding failure occurs, is reported in the upper side of Fig. 61. We can note that for each vibration mode, the MCs present an increasingly oscillating trend as the load level increases, showing local minimum and maximum points in correspondence of the fully developed cracks. In the early load levels, the constant bending zone is most affected by the slope changes of the modal curvature. Subsequently, the reinforcing effect of the FRP plate, mainly provided in the flexural zone, limits the development of these changes, and significant peaks in the curvatures are detected in the shear zones of the beam, where partial detachments of the FRP system are predicted. As a matter of fact, predominant shear cracks are visible in the crack pattern, and an MC value approximately twice as high as the undamaged configuration one is recorded in the curvature envelope of the 1st vibration mode after the yielding stage (L10). Moreover, by comparing the 1st mode MC graph with the crack pattern, we can observe that such a peak coincides with the crack inducing the debonding failure, thus highlighting the good capabilities of the MC method in detecting damage phenomena. However, to detect the diffuse damage evolution, typically provided by the strengthened RC structures, all considered modal shapes must be investigated. Indeed, cracks in the proximity of the FRP plate end do not influence the 1st mode curvature and they are mainly detected by the high-order vibration modes (4th and 7th modes in Fig. 61), where the curvature values differ considerably from the undamaged configuration ones as the load level increases.

A comparison between the MCs of the 1st vibration mode of the control and strengthened beams at the load level L9 is reported in Fig. 62. We can note that the MC of the control beam is characterized

by numerous peaks coinciding with the main cracks observed in the crack pattern reported in the top of Fig. 62. On the other hand, the FRP plate reinforcement, inducing diffuse damage with more cracks having narrower crack widths with respect to that predicted by the control beam, produces a smoother MC with local minimum and maximum points only in the constant bending zone. However, as previously explained, fractures near the supports and the FRP plate end observed in the crack patterns reported in Fig. 62 strongly influence the modal curvature of the high-order vibration modes, therefore it can be deduced that to detect adequately the diffuse damage phenomena through the MC method more than one vibration mode must be analyzed.

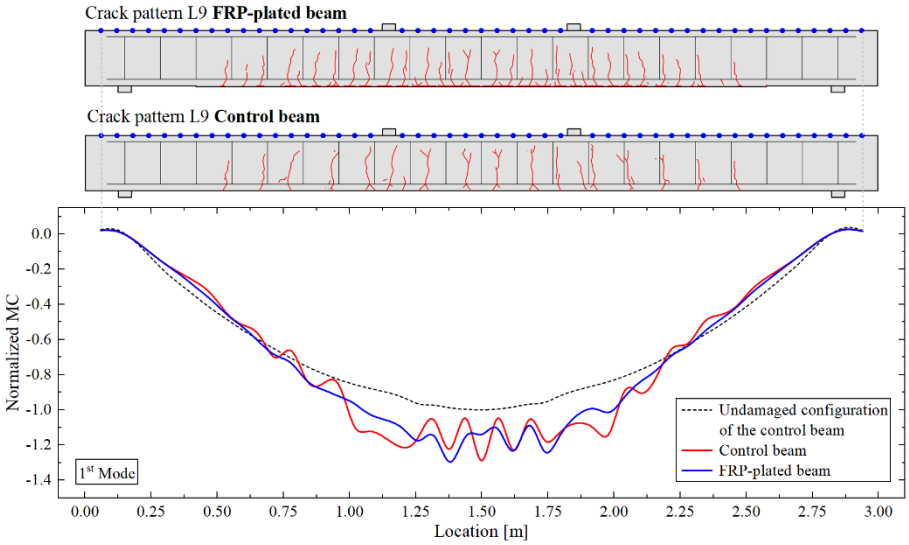

Fig. 62. MC of the 1st vibration mode obtained by the control and strengthened beams for the load level L9.

An efficient damage indicator, which does not focus on the modal curvature of a single vibration mode, is the Curvature Damage Factor (CDF), based on the summation over all investigated modal shapes of the absolute differences between the modal curvatures obtained at the generic $i-$th coordinate by the undamaged and damaged (L1-L12) configurations. Fig. 63 shows the CDF, computed considering the 1st, 4th, 6th, and 7th modes for the previously defined load levels, normalized with respect to its maximum value at the highest investigated load level (L12). We can note that after the earlier load levels, the modal curvature shows local minimum and maximum points distributed along the entire span of the beam, thus capturing the damage phenomena that arise at the FRP plate end. Moreover, the maximum peaks observed at load level L11 (after the yielding stage) coincide with the localized cracks which produce the debonding process starting. After which (L12), despite the significant curvature values predicted in the constant bending zone, these peaks decrease and the immediately adjacent ones increase, highlighting that the FRP detachments rapidly propagate towards the beam end, thus resulting in the complete debonding failure of the beam. It is worth noting that, despite neglecting curvature computation at points under the steel plates, where the loads are applied, smooth modal curvatures with small values also for high load levels, are predicted (see gray zones in

Fig. 63), contrasting the results of the crack pattern where significant cracks are observed in these zones.

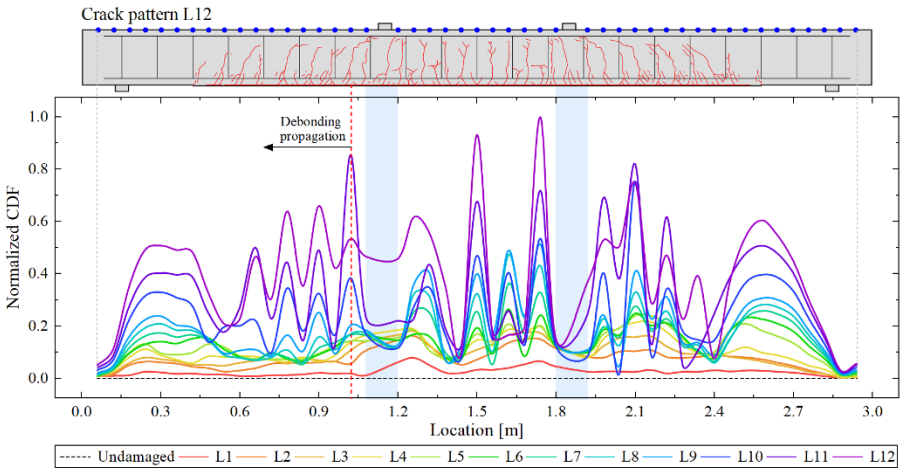

Fig. 63. CDF concerning the 1st, 4th, 6th, and 7th vibration modes as the load level increases.

The numerical investigation on the dynamic characteristic degradation induced by the damage phenomena in strengthened RC structures has been presented in this paragraph. In particular, an improved numerical model, based on the cohesive fracture approach and the embedded truss model to simulate the nonlinear crack processes and mechanical behavior of rebars, respectively, is employed to perform static and dynamic analysis on FRP-plated RC beams. The proposed model is able to capture the material plasticity behavior due to cyclic tensile loads as well as contact phenomena between the crack surfaces. A novelty aspect with respect to the model proposed by some of the authors in [136], concerns the adoption of a suitable Mode-II traction-separation law which takes into account the residual plastic deformations, induced by unloading stages, in the cohesive elements placed along the FRP/concrete interface being strongly affected by mode-II fracture conditions (i.e., sliding). Moreover, an improved determination of the permanent plastic contributions is proposed by introducing a linear variation adequately calibrated to match the experimental results of cyclic tensile tests.

Preliminary static and dynamic simulations have been performed on an unstrengthened control beam and the numerically obtained results have been compared with available experimental outcomes in order to validate the proposed numerical strategy. The static response, in terms of loading curve and crack pattern, has been carried out under monotonic and cyclic quasi-static loading conditions, while the dynamic response, in terms of natural vibration frequencies and modal shapes, has been obtained by solving the problem of free oscillations of small amplitude superimposed on a fixed damaged configuration.

The static structural response shows a good agreement with the reference results, providing a loading curve within the experimental envelope. The dynamic response performed at different load

levels shows a reduction of the natural frequencies as the load level increases mainly induced by the evolution of damage phenomena in the tested structure. In particular, the 1st mode frequency reduction with respect to the undamaged configuration reaches a value of 12.39 % at 95 % of the failure load, corresponding with the yielding load. Moreover, has been observed that the natural frequencies of the high-order modal shapes are most affected by the damage evolution, showing higher percentage variations of the frequencies than the low-order ones. The good agreement between the numerical and experimental results highlights the effectiveness of the proposed model in simulating the damage effects on the dynamic response of the RC structures.

Subsequently, static and dynamic analyses have been performed on an FRP-plated RC beam, providing a suitable comparison with the control beam results. The structural response highlights the strengthening effect of the FRP plate on the load-carrying capacity with respect to the control beam one, showing a considerable increase of dissipated energy from the earlier nonlinear stage until the peak load. Moreover, significant residual plastic deformations, mainly induced by the concrete and rebar plasticity, as well as the contact effect of the partially closed crack faces, are predicted at the high load levels thanks to the adoption of the improved cohesive law. Concerning the dynamic response, the analysis provides natural frequencies higher than the control beam ones, obtaining, in the first five load levels, degradation values lower than 48% and 5% for the load levels L1 and L5, respectively, with respect to those obtained by the control beam. This beneficial effect on the frequency degradation is mainly induced by the FRP reinforcement system which obstructs the crack opening and delays the damage evolution in the structure. Finally, the common dynamic damage indicators, based on the modal curvatures, are employed to identify the location and the extension of the damage. Specifically, the MC method has allowed the main crack location to be correctly identified, but the obtained results strongly depend on the investigated vibration mode. On the other hand, a more comprehensive damage pattern has been predicted by the CDF, able to consider the modal curvatures of different vibration modes, providing accurate detection of partial detachments of the FRP system and the main cracks which induce the debonding failure.

In light of the obtained results, we can conclude that, within the structural health monitoring procedures, based on the coupling between numerical models and experimental data, the proposed numerical model results to be a very useful tool for damage detection of RC structures also strengthened with FRP systems.

4.3 Application of the improved cohesive frictional approach: dynamic properties degradation analysis of plain concrete structures under mixed-mode fracture conditions

This section investigates the crack-induced degradation of the dynamic characteristics in plain concrete elements subjected to mixed-mode fracture conditions. Specifically, the discrete fracture model, based on an inter-element cohesive approach, has been improved taking into account the friction effects, as previously described in section 2.1.4. The obtained numerical results highlight the effectiveness of the proposed model in determining the load-carrying capacity and the degradation of natural vibration frequencies during damage propagation, demonstrating its applicability in the framework of structural health monitoring.

4.3.1 Static and dynamic response of a concrete specimen under mode-I fracture conditions

A three-point bending numerical test is performed involving a plain concrete beam whose geometry and boundary conditions, expressed as a function of height H = 0.2 m , are shown in Fig. 64. The elastic and strength properties of the beam were taken equal to those used in [27]. In particular, Young's modulus and Poisson's ratio of concrete are equal to E = 30 GPa and ν=0.18 respectively, while the cohesive parameters required by the interface law to simulate crack initiation and propagation are shown in Table 16.

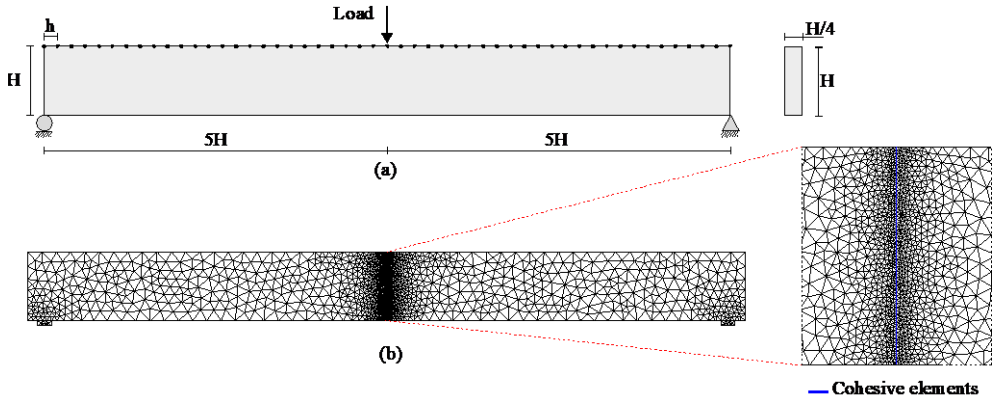

Fig. 64. Geometry and boundary conditions (a); adopted finite element mesh (b) for the three-point bending test.

Table 16. Cohesive parameters required by the cohesive traction-separation law.

K_n^0	K_s^0	t_n^c	t_s^c	G_I^c	G_{II}^c	β
[N/m^3]	[N/m^3]	[MPa]	[MPa]	[N/m]	[N/m]	
1.061e6	8.821e5	3.33	3.33	124	124	225

The values of the initial stiffnesses for the interface law have been calculated by means of the micromechanical calibration methodology proposed in [109] admitting an apparent reduction of the Young's modulus of 2% for the adopted topology and size of the mesh. The mode II parameters, i.e. strength and fracture energy, have been chosen equal to mode I parameters in order to avoid over-resistance effects associated with artificial mesh-induced local mixed-mode state activation. It is important to note that, in order to reduce the computational effort, in the numerical simulations the cohesive elements are inserted only along the vertical line coinciding with the expected path of the main crack (Fig. 64(b)) due to the symmetry for both geometry and boundary conditions. An unstructured mesh (i.e. Delaunay), consisting of three-node planar elements for the solid phase, with a maximum elements size of 42 mm, and zero-thickness four-node elements, arranged along the vertical direction in a number of 30, for the cohesive interfaces, have been used for all simulations.

Quasi-static loading/unloading analyses are performed under plane stress assumption using a displacement-based control algorithm with a displacement increment of 5e-3 mm. The obtained results, in terms of load-deflection curve, are reported in Fig. 65. In particular, at 6 load levels, evaluated as a fraction of the failure load, the tested specimen has been subjected to an unloading stage. They are denoted as: L1, L2, L3, L4, L5, and L6, corresponding to a deflection value of 0.3, 0.515 (deflection at peak load), 0.55, 0.6, 0.8, and 1 mm respectively. The unloading paths have been stopped once a zero value of the load acting on the beam has been reached (points L1', L2', L3', L4', L5', L6' of Fig. 65).

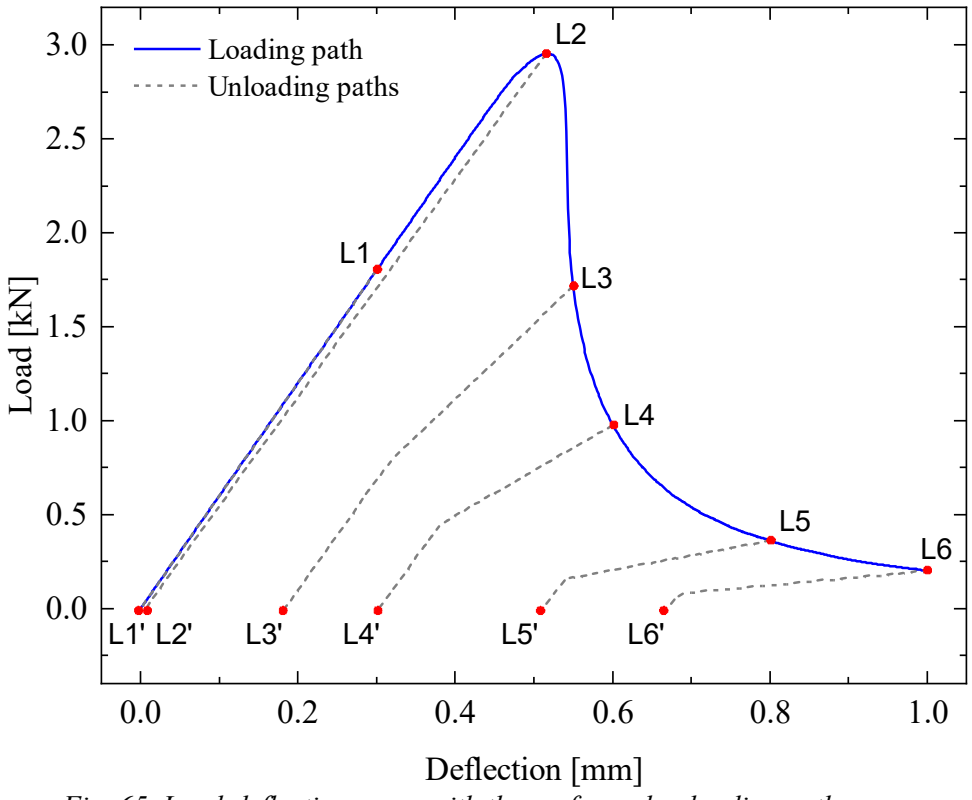

Fig. 65. Load-deflection curve with the performed unloading paths.

The obtained loading curve reflects the typical behavior of quasi-brittle materials with a linearly elastic branch until the peak load, followed by the softening behavior characterized by a fast reduction of the load level. We can note that, along the unloading paths corresponding to different damage levels in the softening branch, where the main crack is almost fully developed, distinct tangent stiffnesses can be observed. This reflects the model's capabilities to predict the intermediate contact state between open and closed cracks, as well as frictional effects resulting from the presence of aggregates that prevent complete crack closure.

Subsequently, the dynamic response of the plain concrete specimen in the presence of damage, previously detected by the quasi-static analysis, is determined by solving the problem of free oscillations of small amplitude, superimposed on the fixed damage configurations. The damage scenarios are associated with the final point of the unloading stages highlighted with red point in Fig. 65. The dynamic behavior in the regime of free oscillations is studied with reference to the damaged framework reached during the unloading stage (points L1'-L6' in Fig. 65). This configuration takes into account the contact phenomena, as well as the friction effects, due to the partial closure of cracks that occur during the unloading phase.

Table 17 shows the variation of the natural vibration frequencies, obtained by the linearized modal analysis at the final point of the unloading branches, as a function of the damage, together with the relative percentage changes with respect to the undamaged configuration for each natural vibration mode. Since at the unloading phase, as previously explained, the stiffening effect of the partial crack closure is taken into account, the reduction of the natural frequencies is quite small. The maximum reduction value of 7.40% comes up at the last unloading stage for the 5th natural vibration mode. However, it should be noted that the damage configurations obtained once the peak load of the system has been exceeded, are difficult to achieve due to the unstable fracture process behavior of the specimen, which is typical in quasi-brittle materials like plain concrete beams (i.e. without any steel reinforcements).

Table 17. Variation of the natural vibration frequencies, as the damage level increase, in the unloading phase.

	f_1 [Hz]	$\Delta f_1/f^0_1$ [%]	f_2 [Hz]	$\Delta f_2/f^0_2$ [%]	f_3 [Hz]	$\Delta f_3/f^0_3$ [%]	f_4 [Hz]	$\Delta f_4/f^0_4$ [%]	f_5 [Hz]	$\Delta f_5/f^0_5$ [%]
Undamaged	77.23	0.00	245.19	0.00	379.94	0.00	671.05	0.00	974.13	0.00
L1'	77.23	0.00	245.19	0.00	379.94	0.00	671.05	0.00	974.13	0.00
L2'	77.01	0.28	245.19	0.00	379.93	0.00	668.77	0.34	973.76	0.04
L3'	76.82	0.53	244.71	0.20	378.87	0.28	665.71	0.80	962.87	1.16

L4'	76.62	0.79	243.76	0.58	376.82	0.82	663.63	1.11	945.34	2.96
L5'	75.86	1.78	241.97	1.31	369.54	2.74	656.05	2.24	922.70	5.28
L6'	75.15	2.69	240.48	1.92	364.76	4.00	653.08	2.68	902.04	7.40

The results in terms of degradation of natural vibration frequencies, normalized with respect to the value obtained for the undamaged configuration, are also reported in Fig. 66.

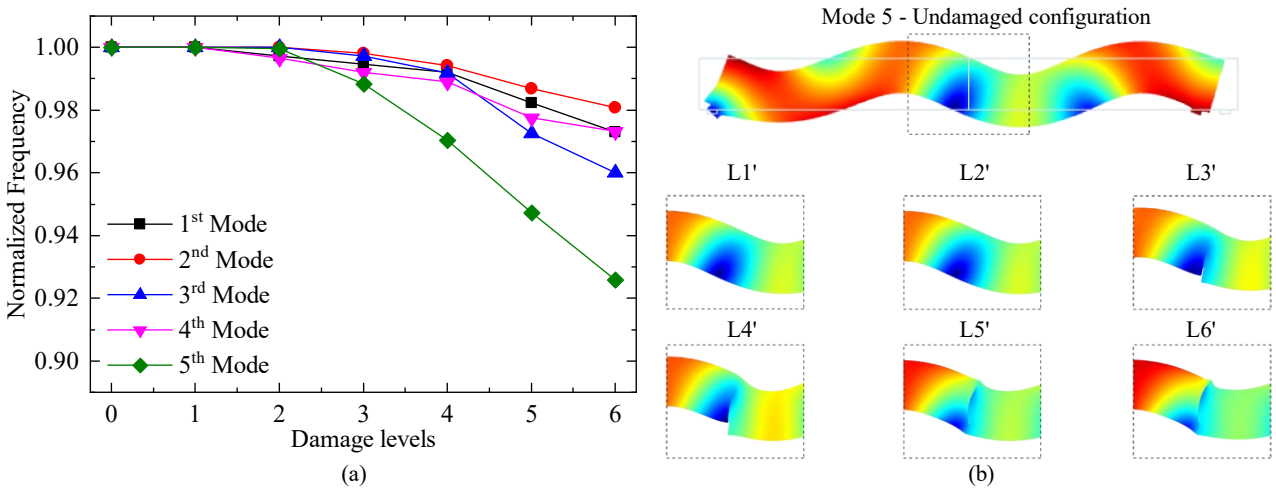

Fig. 66. Variation of the normalized natural vibration frequencies for the first five mode shapes as the damage level increases.

In order to evaluate the effects of the progressive damage on the dynamic characteristic of plain concrete structures, the "Modal Assurance Criterion" (MAC), has been used. Since the damage in structural elements induces a variation in the natural vibration modes, through the MAC values it is possible to obtain a scalar measure of the damage as a function of the correlation between the natural vibration modes before and after the damage occurrence. Such an indicator is expressed as reported in equation (1.66).

Table 18 reports the MAC coefficients evaluated for the different damage levels. Such coefficients correlate the undamaged beam's natural modal shapes for the first five modes with the corresponding damaged ones (L1'-L6'). These values provide a measure of consistency between the two sets of modal vectors, undamaged and damaged. A unit value of the MAC coefficient corresponds to a perfect correlation between the considered two modes, while a value approaching zero indicates a complete inconsistency between the analyzed modal shapes, thus highlighting damage in the considered configuration. The obtained MAC coefficients have been determined with a normalization of the vibration modes through the mass matrix.

It is important to remind that all the modes are related to the unloaded condition. According to the results reported in Table 18, we may note that as the level of damage increases, the correlation between the mode in the damaged configuration and the relatively undamaged one, decreases. This

is evidenced by the diagonal coefficients of the MAC matrix (MAC_{ii}), which increasingly diverge from unity as damage levels increase.

Table 18. MAC for the investigated damage levels with reference to the undamaged configuration

Undamaged – L1'				
1.0000	0.0944	0.0359	0.0008	0.0102
0.0944	1.0000	0.6439	0.0315	0.0048
0.0359	0.6439	1.0000	0.0240	0.0216
0.0008	0.0315	0.0240	1.0000	0.1170
0.0102	0.0048	0.0216	0.1170	1.0000
Undamaged – L2'				
1.0000	0.0944	0.0359	0.0008	0.0102
0.0946	1.0000	0.6438	0.0313	0.0049
0.0359	0.6439	1.0000	0.0241	0.0213
0.0008	0.0315	0.0240	1.0000	0.1201
0.0102	0.0048	0.0216	0.1167	1.0000
Undamaged – L3'				
1.0000	0.0944	0.0361	0.0008	0.0094
0.0933	1.0000	0.6448	0.0324	0.0046
0.0368	0.6452	1.0000	0.0239	0.0189
0.0007	0.0311	0.0229	1.0000	0.1248
0.0104	0.0051	0.0227	0.1053	0.9987
Undamaged – L4'				
0.9999	0.0938	0.0357	0.0008	0.0089
0.0922	0.9999	0.6469	0.0338	0.0041
0.0376	0.6469	0.9999	0.0236	0.0170
0.0007	0.0311	0.0220	0.9980	0.1255
0.0106	0.0057	0.0237	0.0945	0.9939
Undamaged – L5'				
0.9999	0.0944	0.0341	0.0006	0.0173
0.0991	0.9998	0.6479	0.0199	0.0164

0.0335	0.6431	0.9986	0.0345	0.0297
0.0005	0.0333	0.0214	0.9928	0.2167
0.0092	0.0065	0.0284	0.1502	0.9736

Undamaged – L6'

0.9998	0.0938	0.0319	0.0007	0.0228
0.1003	0.9995	0.6498	0.0176	0.0236
0.0330	0.6406	0.9974	0.0361	0.0388
0.0004	0.0359	0.0219	0.9877	0.2438
0.0089	0.0073	0.0302	0.1635	0.9495

However, these deviations are not particularly significant; in fact, the maximum relative percentage deviation is 5 % and is found at the last damage level L6' for mode number 5. Moreover, at the same damage level, the higher modes generally show less correlation than the others. On the other hand, as the level of damage increases, the correlation between different modes increases, i.e. the off-diagonal MACij coefficients take on values gradually greater than the initial one due to the approximate orthogonality between modes. This behavior is related to the expression used for the evaluation of MACs coefficients that is evaluated with reference to a reduced number of degrees of freedom and displacement directions concerning those for which the orthogonality condition is imposed.

Subsequently, to detect the damage position in the tested specimen, the modal curvature (MC) criterion has been employed. In particular, the curvature $\varphi_{ij}^{''}$ of the modal shape at the generic *i*-th coordinate, has been evaluated for each considered damage level, by using the expression (1.67).

Fig. 67 shows the MCs at the different damage levels in the unloading phase (L1'-L6') for the investigated mode shapes considering 51 equidistant points located along the upper edge of the specimen, starting from the left-hand support. The values have been normalized with respect to the value of the maximum curvature obtained by the individual modes in the undamaged configuration. For each mode, as the damage level increases, the curvature shows an increasing peak in proximity to the crack. In particular, the curvature values deviate significantly from those obtained from the undamaged modal shape at points very close to the crack, resulting in noticeable changes in slope. This behavior becomes more pronounced as the level of damage increases, particularly when the crack is nearly fully developed, thus demonstrating the effectiveness of the proposed numerical strategy also in the detection of damage in plain concrete structures.

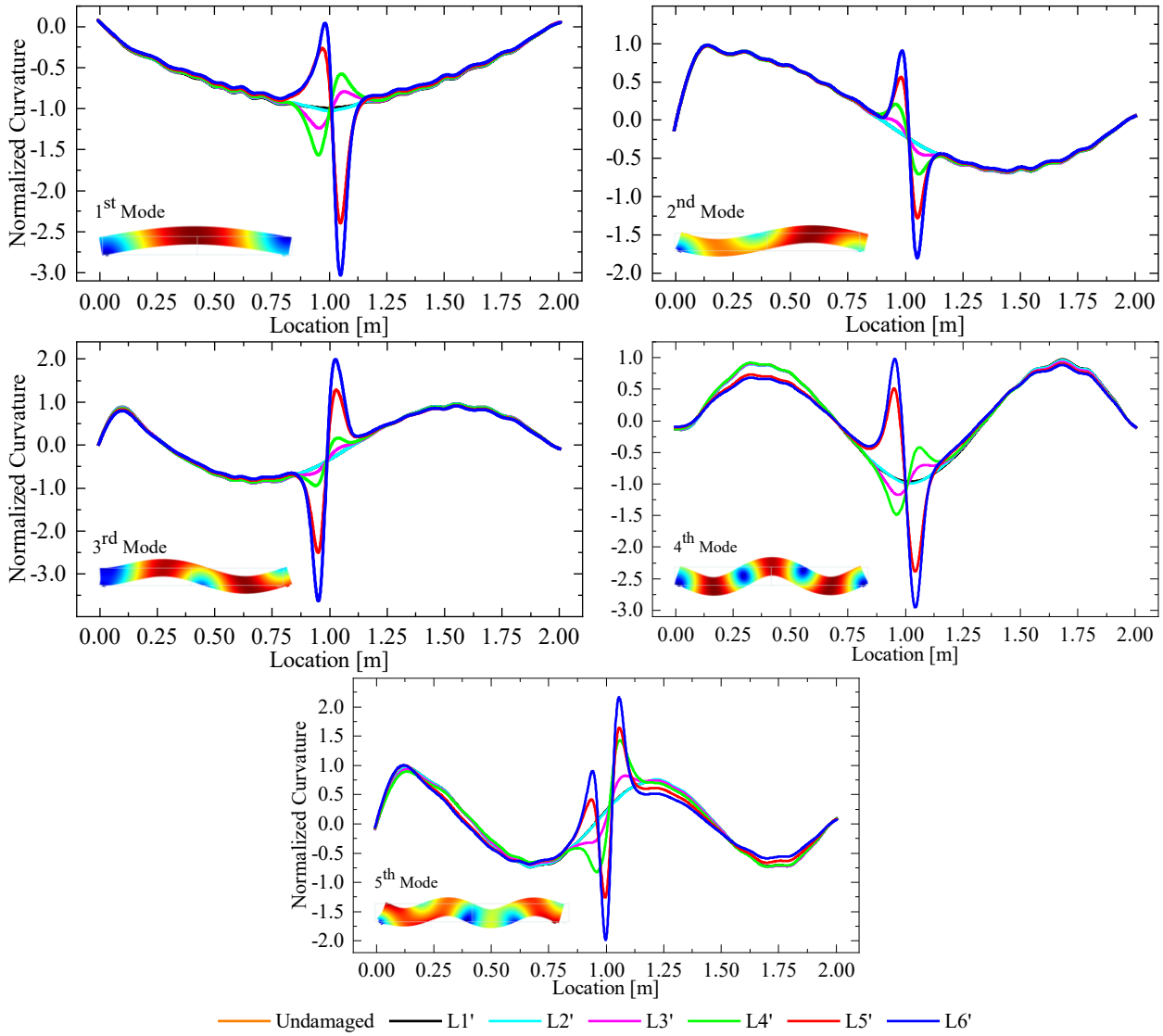

Fig. 67. MC damage factor of the first five mode shapes for all the investigated damage levels at the unloading phase.

4.3.2 Static and dynamic response of a concrete specimen under mixed-mode fracture conditions

The proposed model is here employed to predict the degradation of modal properties of a concrete specimen subjected to general mixed-mode fracture conditions. The analyses refer to a non-symmetric three-point bending test involving a plain concrete notched beam experimentally analyzed by [137]. The geometry of the beam, expressed as a function of the beam height D equal to 75 mm, as well as the unstructured mesh used for the numerical simulations, are reported in Fig. 68. Assuming a linear elastic behavior for the bulk elements, a Young's Modulus of 38 GPa and a Poisson's ratio of 0.20 have been set, according to the parameters reported in [137]. Table 19, instead, reports the inelastic parameters chosen for the cohesive interfaces. As shown in Fig. 68, in order to reduce the degrees of freedom of numerical simulations, the cohesive elements, highlighted in blue in Fig. 68(b), have been included only in the area where damage could potentially evolve. As performed for the

mode I loading conditions test, a Delaunay tessellation, with a maximum size of 18 mm and 2 mm for the bulk and cohesive elements respectively, has been used for the finite element mesh.

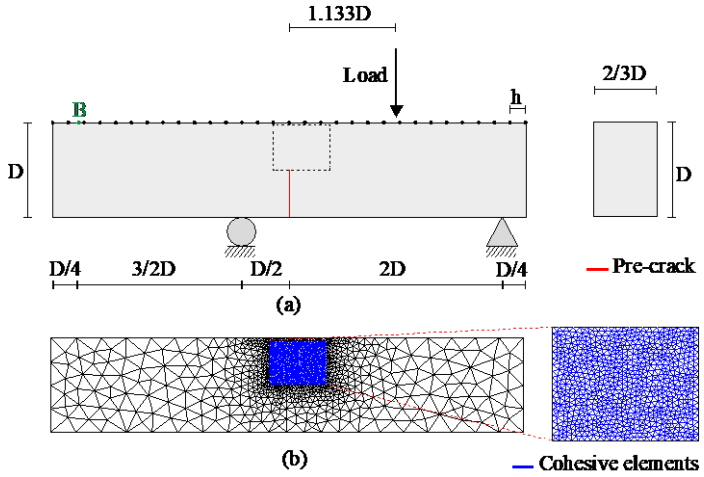

Fig. 68. Geometry and boundary conditions (a) and finite element mesh (b) used for the non-symmetric three-point bending test.

Table 19. Cohesive parameters required by the adopted traction-separation law.

K_n^0	K_s^0	t_n^c	t_s^c	G_I^c	G_{II}^c	β
[N/m^3]	[N/m^3]	[MPa]	[MPa]	[N/m]	[N/m]	
5.492e6	2.746e6	3.00	3.00	69	69	225

A quasi-static numerical simulation to predict the static response in terms of load-carrying capacity, has been performed assuming a plane stress condition and a displacement-based control algorithm with an increment of 5e-4 mm. Similarly to that carried out in the mode-I fracture test, a loading/unloading process has been imposed on the concrete specimen. In particular, at 6 values of displacement of point B reported in (Fig. 68 (a)), i.e., 0.01, 0.0575 (corresponding to the peak load), 0.08, 0.12, 0.16 and 0.2 mm, 6 unloading stages, denoted as L1, L2, …, L6, are performed. It is worth noting that, such unloading processes are performed by decreasing the load level down to 0 kN (reaching points L1', … L6') starting from the load levels corresponding to the previously mentioned displacements of Point B.

The obtained load versus displacement of the point B curve- is reported in Fig. 69. It can be seen that, at the final step of the first two unloading paths (L1 and L2), very small residual plastic deformations are predicted. On the other hand, considering the unloading paths starting from the load levels in the softening branch, the permanent residual deformations increase since the predicted crack is almost fully developed. Moreover, after a certain load level in the unloading path, we can note a stiffer structural behavior induced by the contact effects of the partially closed crack faces occurring

in the cracked specimen. Such a static analysis has provided the damaged structural configurations (one for each considered damage level L1', … L6') on which the dynamic analyses were performed in order to assess the corresponding modal properties.

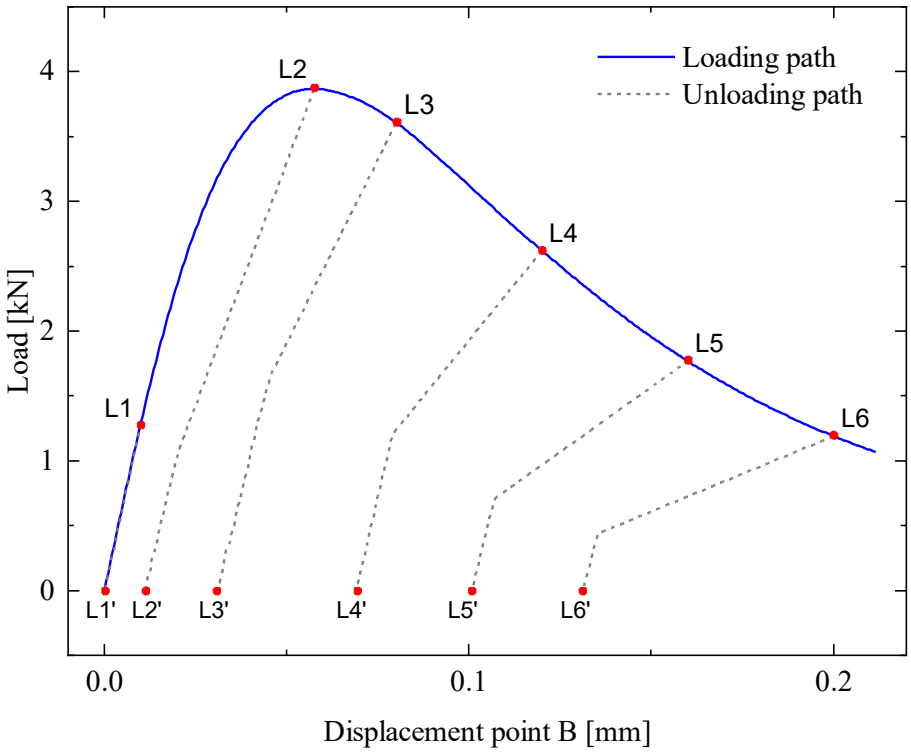

Fig. 69. Load-displacement curve for the non-symmetric three-point bending test with the performed unloading paths.

Now, a linearized eigenvalue problem has been solved at the endpoint of each unloading path in order to take into account the effects of the complex nonlinear phenomena, such as concrete plasticity and partial crack closure behavior, on the natural vibration frequencies. The obtained results in terms of frequencies and their variations with respect to the undamaged configuration are reported in Table 20.

Table 20. Variation of the natural vibration frequencies, as the damage level increases, in the unloading phase for the non-symmetric three-point bending test.

	f_1	$\Delta f_1/f^0_1$	f_2	$\Delta f_2/f^0_2$	f_3	$\Delta f_3/f^0_3$	f_4	$\Delta f_4/f^0_4$	f_5	$\Delta f_5/f^0_5$
	[Hz]	[%]	[Hz]	[%]	[Hz]	[%]	[Hz]	[%]	[Hz]	[%]
Undamaged	632.9	0.00	2448.2	0.00	3423.5	0.00	5252.3	0.00	6696.2	0.00
L1'	632.9	0.00	2448.2	0.00	3423.5	0.00	5252.3	0.00	6696.2	0.00
L2'	601.8	4.91	2422.6	1.05	3230.3	5.64	5114.5	2.62	6674.7	0.32
L3'	581.1	8.18	2406.0	1.72	3191.7	6.77	5039.9	4.04	6653.1	0.64
L4'	588.6	6.99	2399.1	2.01	3190.3	6.81	5012.5	4.57	6623.5	1.09

L5'	567.3	10.36	2368.6	3.25	3071.9	10.27	4896.7	6.77	6582.6	1.70
L6'	546.2	13.69	2329.3	4.86	2988.7	12.70	4767.2	9.24	6545.2	2.26

The reduction of the natural vibration frequencies is not monotonically increasing for higher vibration modes. In fact, as reported in Table 20, the greatest reduction occurs for modes 1 and 3, which have frequency variation values of 13.69% and 12.70%, respectively. Such behavior is related to the peculiarity of the mixed-mode test of non-symmetric boundary conditions imposed on the analyzed concrete beam.

As is well known, the frictional effects become more prominent in all those cases where mixed-mode loading conditions are employed. To this end, in addition to the analysis of the frequency degradation, an interesting comparison in terms of variation of natural vibration frequencies predicted by the proposed model and by the same model without taking into account frictional effects, is reported in Fig. 70.

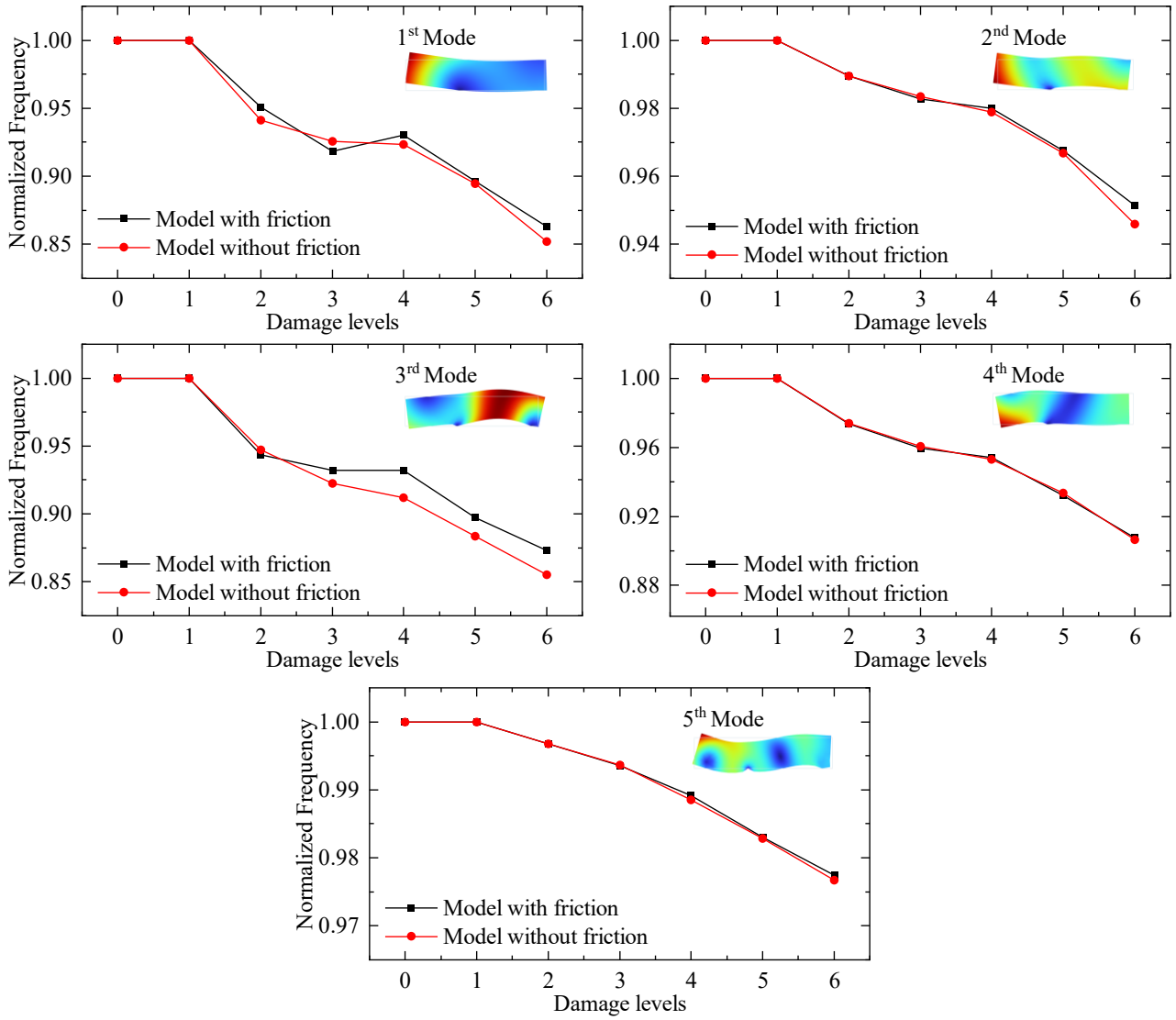

Fig. 70. Normalized frequencies as the damage level increase, of all the investigated mode shapes: effects of the friction contribution on the cohesive mode II traction-separation law.

We can see that, the general trend is such that the contribution of the friction tends to increase the natural vibration frequencies and therefore to attenuate their degradation as the damage level increases, thus suitably simulating the real behavior of concrete structures. Such a behavior is further pronounced by the contact between the crack faces characterized by a partial closure due to the presence of the aggregates. Small exceptions occur only for a few damage levels in some vibration modes (see mode shapes number 1 and 4 of Fig. 71), characterized mainly by mode shapes that involve the free portion of the beam, beyond the left-hand support, and therefore do not involve the area affected by the growth of the damage. As a result, since the portion of the beam outside the cohesive zone is characterized by a linear elastic behavior, the friction effects are partially activated and are not high enough to generate a relatively large increase in the vibration frequencies. In fact, for the fourth mode, the frequency values associated with the cohesive model including the effects of friction are almost equal to those without ones.

Afterwards, the MAC coefficients have been evaluated through Equation (66) and reported in Table 21. As can be seen, perfect correspondence occurs only for the first load level; in fact, in this case, all contributions along the diagonal are equal to 1. On the other hand, as the damage level increases, the values of the diagonal coefficients deviate more and more from the unit value. Furthermore, the same table highlights the growing inconsistency between some of the analyzed mode shapes; in particular, the off-diagonal coefficients indicating the correlation between modes 2 and 5 decrease as the damage level increases, settling at zero from level L4’ onwards.

Table 21. MAC for the investigated damage levels with respect to the undamaged configuration for the non-symmetric three-point bending test.

Undamaged – L1’				
1.0000	0.3658	0.1074	0.0137	0.0026
0.3658	1.0000	0.2882	0.0014	0.0009
0.1074	0.2882	1.000	0.0815	0.0003
0.0137	0.0014	0.0815	1.0000	0.8299
0.0026	0.0009	0.0003	0.8299	1.0000

Undamaged – L2’				
1.0000	0.3926	0.1089	0.0144	0.0024
0.3711	1.0000	0.2880	0.0020	0.0007
0.1040	0.2635	0.9997	0.0871	0.0001
0.0139	0.0012	0.0749	0.9998	0.8419
0.0023	0.0006	0.0007	0.8272	0.9997

Undamaged – L3'

0.9997	0.3602	0.1177	0.0585	0.0019
0.3533	0.9994	0.2781	0.0004	0.0001
0.1145	0.2913	0.9962	0.1078	0.0004
0.0148	0.0015	0.0585	0.9583	0.8715
0.0021	0.0007	0.0031	0.8199	0.9958

Undamaged – L4'

0.9997	0.2021	0.1538	0.1582	0.0016
0.3501	0.9645	0.2308	0.0234	0.0000
0.1172	0.4610	0.9895	0.1187	0.0013
0.0139	0.0036	0.0578	0.8214	0.8821
0.0028	0.0033	0.0036	0.6296	0.9929

Undamaged – L5'

0.9998	0.2444	0.1303	0.2220	0.0015
0.3520	0.9811	0.2597	0.0112	0.0000
0.1159	0.4121	0.9952	0.2388	0.0010
0.0141	0.0027	0.0613	0.7332	0.8739
0.0026	0.0027	0.0028	0.4332	0.9949

Undamaged – L6'

0.9997	0.2405	0.1307	0.4954	0.0012
0.3495	0.9792	0.2589	0.0506	0.0000
0.1174	0.4151	0.9944	0.3144	0.0018
0.0144	0.0022	0.0601	0.2252	0.8802
0.0025	0.0033	0.0030	0.0458	0.9933

In addition, the Modal Curvature (MC) for each vibration mode has been evaluated by using the previously explained Equation (67). In particular, 31 reference points, 11.25 mm equally spaced, have been located along the upper edge of the specimen, as depicted in Fig. 68a. Fig. 71 shows the obtained modal curvatures for the first 5 modes as the damage level increases. We can note that the variations of curvature values are concentrated in the region where the damage phenomena occur. Furthermore,

the loading conditions imposed on the specimen lead to frictional forces that contribute to the expansion of the damaged area beyond the immediate vicinity of the macro crack. This broader understanding underscores the complexity of structural deterioration and highlights the importance of comprehensive assessment methods in ensuring the reliability and safety of the material under consideration.

Additionally, the curves associated with the higher vibration modes present increasingly complex oscillatory trends; such behavior is most emphasized for the fifth vibration mode shape (see Fig. 71**Errore. L'origine riferimento non è stata trovata.**). As a matter of fact, as the level of damage increases, beyond the peak point at which the coalescence of different micro-cracks into a single macro-crack occurs, the curves deviate more and more from that representing the undeformed condition. It is important to remind, however, that the undamaged condition and the condition associated with the L1' level, represented by the orange and black lines in Fig. 71 respectively, are completely overlapping since, as can be seen from the displacement-load curve (Fig. 69), the first unloading path has been carried out for a displacement value that is still associated to a linear-elastic behavior.

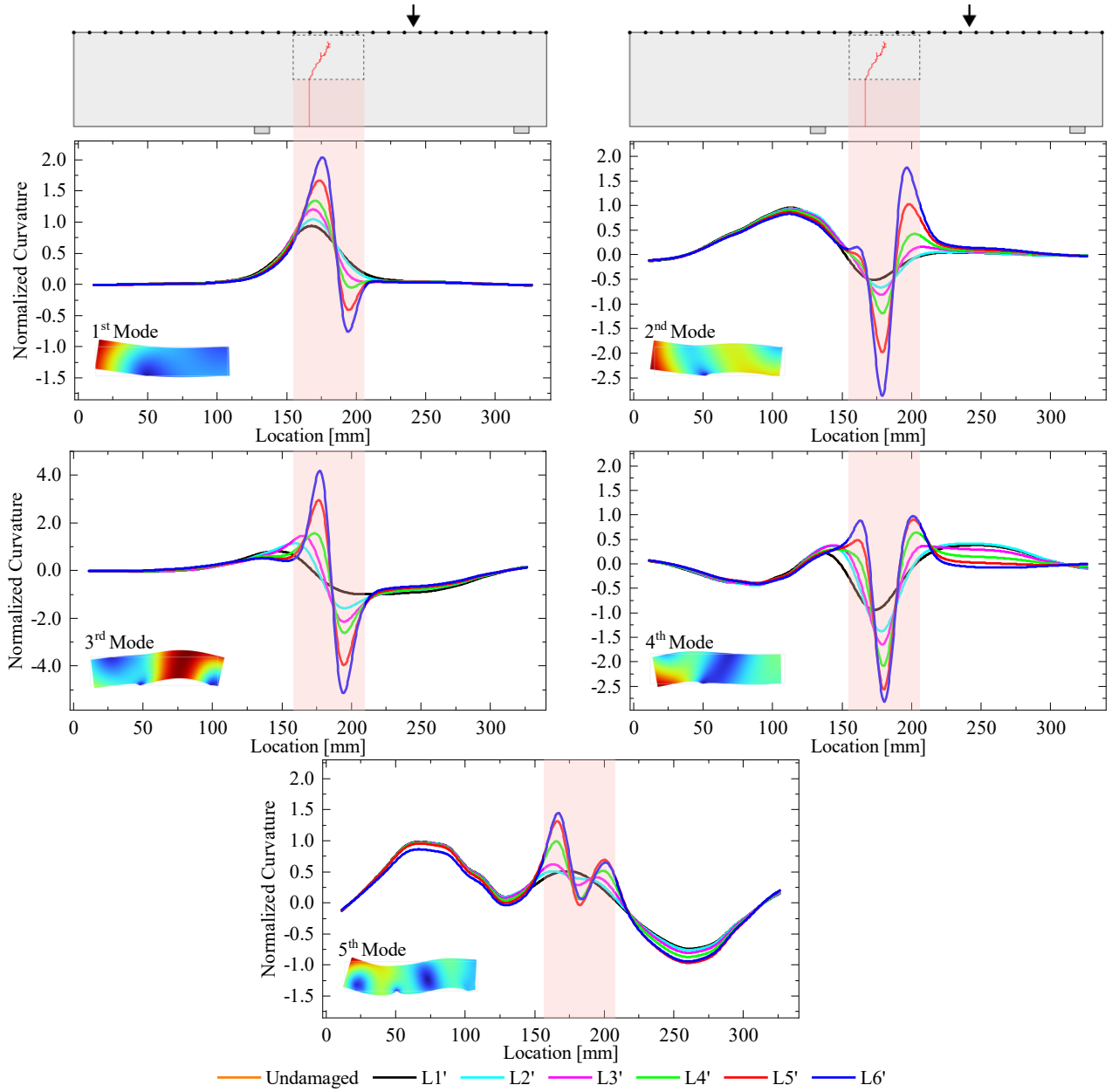

Fig. 71. MC damage factor of the first five mode shapes for all the investigated damage levels at the unloading phase (no-symmetric three-point bending test).

Conclusions

In this thesis, the failure analysis of heterogeneous materials and structures has been widely investigated from a numerical point of view, by means of newly advanced modeling approaches based on a cohesive/volumetric finite element method and multiscale models. Such advanced methods constitute an efficient numerical framework for the simulation of the complex behavior of structures, composed of different materials. The models are able to reproduce the complex non-linear phenomena exhibited by these structures, including crack onset and propagation, and the more complex non-linear phenomena generated for existing structures during cycling loading conditions. The basic concepts of fracture mechanics have been briefly reported in the introduction of the first chapter, whereas the computational modeling approaches for cracking analysis have been critically discussed in the same chapter. In particular, the main goal of the present thesis is to develop two different numerical models, both based on a cohesive/volumetric finite element framework, for the analysis of materials and structures at both macro/mesoscopic and microscopic scales.

The first model is an approach that combines the cohesive fracture model with a hierarchical multiscale approach, so it can be referred to as a "two-scale" model. In particular, the proposed hybrid continuous/discontinuous model belongs to the family of hierarchical multiscale methods. As shown, the numerical applications involve different tests provided by the technical literature, in order to assess the reliability of the proposed model also with reference to experimental results. The main novelty of the proposed model is the incorporation of an additional non-linear homogenization procedure performed on the interfaces, alongside the classical volumetric non-linear homogenization scheme, being still valid until the coalescence of several micro-cracks into a single macro crack; this additional homogenization step is used to compute the microscopically informed traction-separation law for the embedded cohesive interfaces, which is related to the softening part of the RUC's homogenized response. Such an approach, valid for periodic heterogeneous materials, is proposed to overcome the limitations of purely volumetric approaches, which may experience also spurious mesh sensitivity in the presence of strain localization phenomena. It is important to remind that the diffuse interface model has been used in this context to model crack nucleation and propagation at both microscopic and macroscopic scales. Moreover, the off-line homogenization method is proposed to solve nonlinear two-scale problems at the cost of one-scale problems, based on the construction of distinct databases for bulk and cohesive interface homogenization steps.

The second model, on the other hand, is totally based on an inter-element fracture approach and has been used for the dynamic analysis of plain and reinforced concrete structures, as well as FRP-strengthened reinforced concrete beams. The main novelty introduced by the present thesis is the definition of an appropriate traction-separation law able to reproduce the behavior of such structures

subjected to cyclic loading conditions. In particular, the proposed model allows, through a series of properly calibrated parameters, the effects of concrete plasticity to be taken into account, as well as the effects related to the partial contact between the crack faces that cannot completely close due to the presence of aggregates. The numerical formulation, widely validated with preliminary simulations on different kinds of structures, has been further improved by incorporating the friction effects in the mode-II traction-separation law, according to the well-known Coulomb-type friction model. The addition of such an effect is required to adequately model the constitutive behavior of the cohesive elements during the unloading phase characterized by compression states, especially when mixed-mode fracture conditions have been employed.

Both models, whose formulations are fully described in Chapter 2, share a unique diffuse interface approach, which has been developed to be used for the failure analysis of heterogeneous materials and structures at different scales, i.e. microscopic in the first case by employing the proposed fracture model into a hierarchical multiscale method, and macroscopic in the second one in order to develop structural analysis procedures that can be included among the structural health monitoring techniques.

The first part of the numerical results, see Chapter 3, is devoted to the failure analysis of heterogeneous materials. In this context, the two different models previously recalled have been successfully applied at both macro and micro-scales.

In particular, the implemented diffuse interface model has been tested to evaluate the effect of nano-modified epoxy resin on the behavior of FRP-plated concrete structures, providing some interesting results reported in section 3.1. A nano-additive epoxy resin has been considered as a novel method to guarantee the bond between the structural elements and the FRP sheets used as a reinforcement. Preliminary, a calibration step was necessary in order to assess how the embedded nanomaterials modify the bond-slip law between the concrete and the FRP. Such a step, performed on a double lap shear test, presented very good results and the numerical response provided by numerical simulations is in agreement with the experimental one. Subsequently, once the parameters required from the bond-slip law had been adequately calibrated, the model has been tested on a reinforced concrete beam, showing the beneficial effect of the additive resin, compared to the classical one, in terms of strength. Furthermore, the model also showed positive effects in terms of fracture behavior, with the nano-modified epoxy resin showing a smaller width of the developed cracks.

On the other hand, in section 3.2, the hybrid cohesive/volumetric homogenization strategy, where the cohesive diffuse model has been implemented into a two-step homogenization procedure, has been applied for the failure analysis of fiber-reinforced composite elements. In detail, the numerical outcomes involve a composite beam under global mode-I fracture conditions during a three-point bending test, and a composite panel subjected to global mixed-mode boundary conditions. Linear and

non-linear homogenization procedures have been performed in order to evaluate the undamaged moduli and the homogenized response in terms of the stress-strain curve, respectively. The latter procedure includes the novel development provided in this thesis, i.e. the interface homogenization involved in the two-step homogenization strategy, in order to derive a properly homogenized traction-separation law. The obtained curves have been used as input files for the description of the behavior of the homogenized material. After these initial steps, the structural response of the fiber-reinforced specimens has been analyzed in terms of Load-CMOD curve for the composite beam, and Force-Displacement for the composite panel. The numerical results have been compared with the outcomes obtained by a Direct Numerical Simulation on the fully meshed specimen and interesting results have been shown. For the mode-I fracture conditions test, three different meshes have been employed in the finite element framework and the results are almost in agreement with the DNS ones, with small exceptions for the unstructured mesh used to discretize the area where cracks can grow. The numerical investigation has however shown that the strength overestimation obtained in this case is not related to the homogenization scheme, but rather to the artificial crack path tortuosity induced by the diffuse interface model. For the mixed-mode test, the same procedures have been adapted to an L-shaped composite panel, widely studied in the technical literature for both homogeneous and heterogeneous materials. In this case, the multiscale and direct analysis presents an overall error on the peak load of about 4%, due to the fact the nonlinear homogenization procedure performed on the repeating unit cell follows a pure mode-I fracture propagation due to the applied loading path.

In the second part of the results, the improved numerical formulation for loading/unloading processes has been applied for the non-linear analysis of the load-induced degradation of vibration characteristics in structural elements. As is widely known, common civil structures and infrastructures are subjected to cyclic loading conditions, with loading phases alternating with the unloading ones. To this end, to study the static and dynamic behavior of such structures, it is necessary to take into account the residual plastic deformation due to the consecutive loading stages, once the elastic phase is exceeded. Moreover, it is also important to take into account all the possible effects that arise during the unloading phase, and the neglecting of these effects leads to an error in the evaluation of the structural response. It was, therefore, necessary to implement these effects within the cohesive law and thus obtain a numerical model that is as accurate as possible for these types of applications. Such implementation, explained in detail in Chapter 2, has been successfully validated and used in the numerical results reported in this thesis, with reference to Chapter 4. In particular, the response of reinforced concrete beams, as well as that of FRP-strengthened beams, have been investigated in the first part of Chapter 4. The obtained outcomes provided insight into how the increase in damage affects the natural vibration frequencies. Preliminary, the innovative model has been validated by means of a comparison with experimental results provided by the technical literature on the damage

assessment of reinforced concrete structures. Following the validation procedure, an FRP-plated reinforced concrete beam has been analyzed in order to extend the formulation to other application fields. This choice is motivated by the fact that such structural health monitoring procedures are mostly applied to existing structures that may be subjected to structural repair or reinforcement using both innovative (i.e. composite materials) or traditional (i.e. steel) materials. The obtained results have shown a good capacity of the model to predict the variation of the natural vibration frequencies, as the damage level increases, also for these kinds of structures, highlighting its complete versatility. Moreover, also the most common damage indicators that have been evaluated following the theoretical expression reported in the same chapter, have shown the capability of the model to predict the correlation between the different mode shapes and to adequately identify the real damage scenario in the structural elements.

In the last part of the numerical results presented in the same chapter, the model has been applied to the investigation of dynamic properties of damaged plain concrete structures, with the novelty of the incorporation of the effects related to the friction phenomena. In order to capture these effects, a non-symmetric three-point bending test, which as is well known involves mixed-mode crack propagation, has been studied. Here, a comparison in terms of variation of the natural vibration frequencies as the damage level increases has been made between the model with the friction contributions and the standard model (i.e. no friction effects included) used for the numerical tests reported in the first part of Chapter 4. In this case, the friction effects are prominent for the odd-numbered modes, i.e. the mode shapes that involve the area of the beam where the damage may grow due to the presence of the cohesive elements.

The obtained outcomes confirm the reliability of the proposed model to adequately reproduce the dynamic response of different kinds of concrete structures, and the strength of the proposed numerical model in being able to capture, if appropriately modeled and taking into account as shown in the present thesis, all the aspect linked to the behavior of the material during the cyclic loading conditions. As future perspectives of this work, the following research directions could be explored:

- Extension of the proposed diffuse interface model to the 3D case in order to study the nonlinear response of reinforced concrete beams.
- Improving the proposed cohesive/friction formulation (see 2.1.4) in order to study the influence of diffuse damage, in the field of structural health monitoring techniques, on the vibrational properties of reinforced concrete beams under more general loading conditions.
- Referring to the hybrid cohesive/volumetric homogenization approach, a possible improvement could be the extension to a 3D case, in order to simulate more complex failure mechanisms in cross-ply laminates under general loading conditions. Furthermore, the model could be also applied to more complex microstructures (i.e. particle reinforced composites,

random composites etc). Moreover, another possible improvement could be the incorporation of plasticity as well as the adoption of more efficient crack modelling.

Bibliography

[1] S. Nemat-Nasser, M. Hori, Micromechanics: overall properties of heterogeneous materials, North-Holland, Amsterdam ; New York, 1993.

[2] D. Bruno, F. Greco, P. Lonetti, P. Nevone Blasi, Influence of micro-cracking and contact on the effective properties of composite materials, Simulation Modelling Practice and Theory 16 (2008) 861–884. https://doi.org/10.1016/j.simpat.2008.05.006.

[3] X.-P. Xu, A. Needleman, Numerical simulations of fast crack growth in brittle solids, Journal of the Mechanics and Physics of Solids 42 (1994) 1397–1434. https://doi.org/10.1016/0022-5096(94)90003-5.

[4] Y. Sheng, D. Yang, Y. Tan, J. Ye, Microstructure effects on transverse cracking in composite laminae by DEM, Composites Science and Technology 70 (2010) 2093–2101. https://doi.org/10.1016/j.compscitech.2010.08.006.

[5] F.K. Wittel, J. Schulte-Fischedick, F. Kun, B.-H. Kröplin, M. Frieß, Discrete element simulation of transverse cracking during the pyrolysis of carbon fibre reinforced plastics to carbon/carbon composites, Computational Materials Science 28 (2003) 1–15. https://doi.org/10.1016/S0927-0256(03)00035-1.

[6] M.L. Boubakar, F. Trivaudey, D. Perreux, L. Vang, A meso–macro finite element modelling of laminate structures, Composite Structures 58 (2002) 271–286. https://doi.org/10.1016/S0263-8223(02)00049-1.

[7] P. Ladeveze, E. Ledantec, Damage modelling of the elementary ply for laminated composites, Composites Science and Technology 43 (1992) 257–267. https://doi.org/10.1016/0266-3538(92)90097-M.

[8] C. Miehe, J. Schröder, M. Becker, Computational homogenization analysis in finite elasticity: material and structural instabilities on the micro- and macro-scales of periodic composites and their interaction, Computer Methods in Applied Mechanics and Engineering 191 (2002) 4971–5005. https://doi.org/10.1016/S0045-7825(02)00391-2.

[9] T.J. Massart, R.H.J. Peerlings, M.G.D. Geers, Mesoscopic modeling of failure and damage-induced anisotropy in brick masonry, European Journal of Mechanics - A/Solids 23 (2004) 719–735. https://doi.org/10.1016/j.euromechsol.2004.05.003.

[10] M. Hain, P. Wriggers, Numerical homogenization of hardened cement paste, Comput Mech 42 (2008) 197–212. https://doi.org/10.1007/s00466-007-0211-9.

[11] Z.P. Bažant, J. Planas, Fracture and Size Effect in Concrete and Other Quasibrittle Materials, 1st ed., Routledge, 2019. https://doi.org/10.1201/9780203756799.

[12] Inglis, C.E., Stresses in Plate due to the Presence of Cracks and Sharp Corners, Trans. Insitute of Naval Architecture 55 (1913) 219–241.

[13] Griffith, A.A., The Phenomena of Rupture and Flows in Solids., Philosophical Transactions of the Royal Society of London. Series A: Mathematical, Physical and Engineering Sciences (1921) 163–167.

[14] Irwin, G.R., Analysis of stresses ad strains near the end of a crack traversing a plate, J. Appl. Mech. 24 (1957) 361–361.

[15] J.R. Rice, A Path Independent Integral and the Approximate Analysis of Strain Concentration by Notches and Cracks, Journal of Applied Mechanics 35 (1968) 379–386. https://doi.org/10.1115/1.3601206.

[16] Rice, J.R., Mathematical analysis in the mechanics of fracture. Fracture: an advanced treatise, 2 (n.d.) 191–311.

[17] Irwin, G.R., Fracture, Handbuch Der Physik VI, Flugge Ed (n.d.) 551–590.

[18] D.S. Dugdale, Yielding of steel sheets containing slits, Journal of the Mechanics and Physics of Solids 8 (1960) 100–104. https://doi.org/10.1016/0022-5096(60)90013-2.

[19] F.M. Burdekin, D.E.W. Stone, The crack opening displacement approach to fracture mechanics in yielding materials, Journal of Strain Analysis 1 (1966) 145–153. https://doi.org/10.1243/03093247V012145.

[20] The application of fracture mechanics to yielding materials, Proc. R. Soc. Lond. A 285 (1965) 34–45. https://doi.org/10.1098/rspa.1965.0087.

[21] Evans, R.H. and Marathe, M.S., Microcracking and Stress-Strain Curves for Concrete in tension, (n.d.).

[22] Rashid, Y.R., Nucl. Eng. Design, Analysis of Prestresse Concrete Pressure Vessels (1968).

[23] Scanlon, A, Time-dependent deflection of reinforced concrete slab (PhD Thesis), (1971).

[24] G.I. Barenblatt, The Mathematical Theory of Equilibrium Cracks in Brittle Fracture, in: Advances in Applied Mechanics, Elsevier, 1962: pp. 55–129. https://doi.org/10.1016/S0065-2156(08)70121-2.

[25] M. Kuna, Finite Elements in Fracture Mechanics: Theory - Numerics - Applications, Springer Netherlands, Dordrecht, 2013. https://doi.org/10.1007/978-94-007-6680-8.

[26] A. Hillerborg, M. Modéer, P.-E. Petersson, Analysis of crack formation and crack growth in concrete by means of fracture mechanics and finite elements, Cement and Concrete Research 6 (1976) 773–781. https://doi.org/10.1016/0008-8846(76)90007-7.

[27] Petersson, P.E., Crack growth and development of fracture zone in plain concrete and similar materials (No. TVBM-100)., (1981).

[28] A.R. Ingraffea, W.H. Gerstk, P. Gergely, V. Saouma, Fracture Mechanics of Bond in Reinforced Concrete, J. Struct. Eng. 110 (1984) 871–890. https://doi.org/10.1061/(ASCE)0733-9445(1984)110:4(871).

[29] K. Park, H. Choi, G.H. Paulino, Assessment of cohesive traction-separation relationships in ABAQUS: A comparative study, Mechanics Research Communications 78 (2016) 71–78. https://doi.org/10.1016/j.mechrescom.2016.09.004.

[30] J.H. Rose, J. Ferrante, J.R. Smith, Universal Binding Energy Curves for Metals and Bimetallic Interfaces, Phys. Rev. Lett. 47 (1981) 675–678. https://doi.org/10.1103/PhysRevLett.47.675.

[31] A. Needleman, An analysis of decohesion along an imperfect interface, Int J Fract 42 (1990) 21–40. https://doi.org/10.1007/BF00018611.

[32] V. Tvergaard, J.W. Hutchinson, The relation between crack growth resistance and fracture process parameters in elastic-plastic solids, Journal of the Mechanics and Physics of Solids 40 (1992) 1377–1397. https://doi.org/10.1016/0022-5096(92)90020-3.

[33] M. Ortiz, A. Pandolfi, Finite-deformation irreversible cohesive elements for three-dimensional crack-propagation analysis, Int. J. Numer. Meth. Engng. 44 (1999) 1267–1282. https://doi.org/10.1002/(SICI)1097-0207(19990330)44:9<1267::AID-NME486>3.0.CO;2-7.

[34] P. Bocca, A. Carpinteri, S. Valente, Mixed mode fracture of concrete, International Journal of Solids and Structures 27 (1991) 1139–1153. https://doi.org/10.1016/0020-7683(91)90115-V.

[35] W.H. Gerstle, M. Xie, FEM Modeling of Fictitious Crack Propagation in Concrete, J. Eng. Mech. 118 (1992) 416–434. https://doi.org/10.1061/(ASCE)0733-9399(1992)118:2(416).

[36] I. Carol, P.C. Prat, C.M. López, Normal/Shear Cracking Model: Application to Discrete Crack Analysis, J. Eng. Mech. 123 (1997) 765–773. https://doi.org/10.1061/(ASCE)0733-9399(1997)123:8(765).

[37] D.A. Cendón, J.C. Gálvez, M. Elices, J. Planas, [No title found], International Journal of Fracture 103 (2000) 293–310. https://doi.org/10.1023/A:1007687025575.

[38] M.V.K.V. Prasad, C.S. Krishnamoorthy, Computational model for discrete crack growth in plain and reinforced concrete, Computer Methods in Applied Mechanics and Engineering 191 (2002) 2699–2725. https://doi.org/10.1016/S0045-7825(02)00210-4.

[39] J.C. Gálvez, J. Červenka, D.A. Cendón, V. Saouma, A discrete crack approach to normal/shear cracking of concrete, Cement and Concrete Research 32 (2002) 1567–1585. https://doi.org/10.1016/S0008-8846(02)00825-6.

[40] G.T. Camacho, M. Ortiz, Computational modelling of impact damage in brittle materials, International Journal of Solids and Structures 33 (1996) 2899–2938. https://doi.org/10.1016/0020-7683(95)00255-3.

[41] L.G. Margolin, A generalized Griffith criterion for crack propagation, Engineering Fracture Mechanics 19 (1984) 539–543. https://doi.org/10.1016/0013-7944(84)90010-9.

[42] J.K. Dienes, Comments on “a generalized griffith criterion for crack propagation” by L. G. Margolin, Engineering Fracture Mechanics 23 (1986) 615–617. https://doi.org/10.1016/0013-7944(86)90165-7.

[43] N. Moës, T. Belytschko, Extended finite element method for cohesive crack growth, Engineering Fracture Mechanics 69 (2002) 813–833. https://doi.org/10.1016/S0013-7944(01)00128-X.

[44] J. Planas, M. Elices, Asymptotic analysis of a cohesive crack: 1. Theoretical background, Int J Fract 55 (1992) 153–177. https://doi.org/10.1007/BF00017275.

[45] J. Planas, M. Elices, Asymptotic analysis of a cohesive crack: 2. Influence of the softening curve, International Journal of Fracture 64 (1993) 221–237.

[46] J. Dolbow, N. Moës, T. Belytschko, Discontinuous enrichment in finite elements with a partition of unity method, Finite Elements in Analysis and Design 36 (2000) 235–260. https://doi.org/10.1016/S0168-874X(00)00035-4.

[47] F. Erdogan, G.C. Sih, On the Crack Extension in Plates Under Plane Loading and Transverse Shear, Journal of Basic Engineering 85 (1963) 519–525. https://doi.org/10.1115/1.3656897.

[48] B. Gee, M. Parchei-Esfahani, R. Gracie, XFEM simulation of a mixed-mode fracture experiment in PMMA, Engineering Fracture Mechanics 229 (2020) 106945. https://doi.org/10.1016/j.engfracmech.2020.106945.

[49] B. Gee, M. Parchei-Esfahani, R. Gracie, XFEM simulation of a mixed-mode fracture experiment in PMMA, Engineering Fracture Mechanics 229 (2020) 106945. https://doi.org/10.1016/j.engfracmech.2020.106945.

[50] G. Zi, T. Belytschko, New crack-tip elements for XFEM and applications to cohesive cracks, Int. J. Numer. Meth. Engng. 57 (2003) 2221–2240. https://doi.org/10.1002/nme.849.

[51] R. de de Borst, M.A. Gutiérrez, G.N. Wells, J.J.C. Remmers, H. Askes, Cohesive-zone models, higher-order continuum theories and reliability methods for computational failure analysis: COMPUTATIONAL FAILURE ANALYSIS, Int. J. Numer. Meth. Engng. 60 (2004) 289–315. https://doi.org/10.1002/nme.963.

[52] J. Mergheim, E. Kuhl, P. Steinmann, A finite element method for the computational modelling of cohesive cracks, Int. J. Numer. Meth. Engng 63 (2005) 276–289. https://doi.org/10.1002/nme.1286.

[53] T. Belytschko, N. Moës, S. Usui, C. Parimik, Arbitrary discontinuities in finite elements, International Journal for Numerical Methods in Engineering 50 (2001) 993–1013.

[54] M. Stolarska, D.L. Chopp, N. Moës, T. Belytschko, Modelling crack growth by level sets in the extended finite element method, Int. J. Numer. Meth. Engng. 51 (2001) 943–960. https://doi.org/10.1002/nme.201.

[55] J.M. Sancho, J. Planas, D.A. Cendón, E. Reyes, J.C. Gálvez, An embedded crack model for finite element analysis of concrete fracture, Engineering Fracture Mechanics 74 (2007) 75–86. https://doi.org/10.1016/j.engfracmech.2006.01.015.

[56] J.C. Simo, J. Oliver, F. Armero, An analysis of strong discontinuities induced by strain-softening in rate-independent inelastic solids, Computational Mechanics 12 (1993) 277–296. https://doi.org/10.1007/BF00372173.

[57] T.C. Gasser, G.A. Holzapfel, 3D Crack propagation in unreinforced concrete., Computer Methods in Applied Mechanics and Engineering 195 (2006) 5198–5219. https://doi.org/10.1016/j.cma.2005.10.023.

[58] P. Jäger, P. Steinmann, E. Kuhl, Modeling three-dimensional crack propagation-A comparison of crack path tracking strategies, Int. J. Numer. Meth. Engng 76 (2008) 1328–1352. https://doi.org/10.1002/nme.2353.

[59] J.M. Sancho, J. Planas, J.C. Gálvez, E. Reyes, D.A. Cendón, An embedded cohesive crack model for finite element analysis of mixed mode fracture of concrete*, Fatigue Fract Eng Mat Struct 29 (2006) 1056–1065. https://doi.org/10.1111/j.1460-2695.2006.01076.x.

[60] J.M. Sancho, J. Planas, J.C. Gálvez, E. Reyes, D.A. Cendón, An embedded cohesive crack model for finite element analysis of mixed mode fracture of concrete, Fat Frac Eng Mat Struct 29 (2006) 1056–1065. https://doi.org/10.1111/j.1460-2695.2006.01076.x.

[61] L.M. Kachanov, Introduction to continuum damage mechanics, M. Nijhoff, Dordrecht ; Boston, 1986.

[62] J.C. Simo, J.W. Ju, Strain- and stress-based continuum damage models—I. Formulation, International Journal of Solids and Structures 23 (1987) 821–840. https://doi.org/10.1016/0020-7683(87)90083-7.

[63] J.C. Simo, J.W. Ju, Strain- and stress-based continuum damage models—II. Computational aspects, International Journal of Solids and Structures 23 (1987) 841–869. https://doi.org/10.1016/0020-7683(87)90084-9.

[64] J. Lemaitre, J.-L. Chaboche, B. Shrivastava, Mechanics of solid materials, 1. paperback ed., repr.transferred to digital print, Cambridge Univ. Press, Cambridge, 2002.

[65] M.G.D. Geers, R. de Borst, W.A.M. Brekelmans, R.H.J. Peerlings, Strain-based transient-gradient damage model for failure analyses, Computer Methods in Applied Mechanics and Engineering 160 (1998) 133–153. https://doi.org/10.1016/S0045-7825(98)80011-X.

[66] R.H.J. Peerlings, R. de Borst, W.A.M. Brekelmans, M.G.D. Geers, Gradient enhanced damage modelling of concrete fracture, Mechanics of Cohesive-Frictional Materials 3 (1998) 323–342.

[67] M. Jirásek, Non-local damage mechanics with application to concrete, Revue Française de Génie Civil 8 (2004) 683–707. https://doi.org/10.1080/12795119.2004.9692625.

[68] D. Krajcinovic, G.U. Fonseka, The Continuous Damage Theory of Brittle Materials, Part 1: General Theory, Journal of Applied Mechanics 48 (1981) 809–815. https://doi.org/10.1115/1.3157739.

[69] E. Kuhl, E. Ramm, Simulation of strain localization with gradient enhanced damage models, Computational Materials Science 16 (1999) 176–185. https://doi.org/10.1016/S0927-0256(99)00060-9.

[70] W. Zhou, J. Zhao, Y. Liu, Q. Yang, Simulation of localization failure with strain-gradient-enhanced damage mechanics, Int. J. Numer. Anal. Meth. Geomech. 26 (2002) 793–813. https://doi.org/10.1002/nag.225.

[71] L. Leonetti, N. Fantuzzi, P. Trovalusci, F. Tornabene, Scale Effects in Orthotropic Composite Assemblies as Micropolar Continua: A Comparison between Weak- and Strong-Form Finite Element Solutions, Materials 12 (2019) 758. https://doi.org/10.3390/ma12050758.

[72] I.M. Gitman, H. Askes, L.J. Sluys, Representative volume: Existence and size determination, Engineering Fracture Mechanics 74 (2007) 2518–2534. https://doi.org/10.1016/j.engfracmech.2006.12.021.

[73] V. Phu Nguyen, O. Lloberas-Valls, M. Stroeven, L. Johannes Sluys, On the existence of representative volumes for softening quasi-brittle materials – A failure zone averaging scheme, Computer Methods in Applied Mechanics and Engineering 199 (2010) 3028–3038. https://doi.org/10.1016/j.cma.2010.06.018.

[74] Z. Hashin, S. Shtrikman, A variational approach to the theory of the elastic behaviour of multiphase materials, Journal of the Mechanics and Physics of Solids 11 (1963) 127–140. https://doi.org/10.1016/0022-5096(63)90060-7.

[75] W.J. Drugan, J.R. Willis, A micromechanics-based nonlocal constitutive equation and estimates of representative volume element size for elastic composites, Journal of the Mechanics and Physics of Solids 44 (1996) 497–524. https://doi.org/10.1016/0022-5096(96)00007-5.

[76] M. Ostoja-Starzewski, Microstructural Randomness Versus Representative Volume Element in Thermomechanics, Journal of Applied Mechanics 69 (2002) 25–35. https://doi.org/10.1115/1.1410366.

[77] R. Hill, Elastic properties of reinforced solids: Some theoretical principles, Journal of the Mechanics and Physics of Solids 11 (1963) 357–372. https://doi.org/10.1016/0022-5096(63)90036-X.

[78] Z. Hashin, Analysis of Composite Materials—A Survey, Journal of Applied Mechanics 50 (1983) 481–505. https://doi.org/10.1115/1.3167081.

[79] F. Greco, Homogenized mechanical behavior of composite micro-structures including micro-cracking and contact evolution, Engineering Fracture Mechanics 76 (2009) 182–208. https://doi.org/10.1016/j.engfracmech.2008.09.006.

[80] T. Belytschko, J. Song, Coarse-graining of multiscale crack propagation, Numerical Meth Engineering 81 (2010) 537–563. https://doi.org/10.1002/nme.2694.

[81] P. Kanouté, D.P. Boso, J.L. Chaboche, B.A. Schrefler, Multiscale Methods for Composites: A Review, Arch Computat Methods Eng 16 (2009) 31–75. https://doi.org/10.1007/s11831-008-9028-8.

[82] V.G. Kouznetsova, M.G.D. Geers, W.A.M. Brekelmans, Multi-scale second-order computational homogenization of multi-phase materials: a nested finite element solution strategy, Computer Methods in Applied Mechanics and Engineering 193 (2004) 5525–5550. https://doi.org/10.1016/j.cma.2003.12.073.

[83] I.M. Gitman, H. Askes, L.J. Sluys, Coupled-volume multi-scale modelling of quasi-brittle material, European Journal of Mechanics - A/Solids 27 (2008) 302–327. https://doi.org/10.1016/j.euromechsol.2007.10.004.

[84] P. Trovalusci, M.L. De Bellis, M. Ostoja-Starzewski, A. Murrali, Particulate random composites homogenized as micropolar materials, Meccanica 49 (2014) 2719–2727. https://doi.org/10.1007/s11012-014-0031-x.

[85] M. Tuna, L. Leonetti, P. Trovalusci, M. Kirca, ‘Explicit’ and ‘implicit’ non-local continuous descriptions for a plate with circular inclusion in tension, Meccanica 55 (2020) 927–944. https://doi.org/10.1007/s11012-019-01091-3.

[86] T.J. Massart, R.H.J. Peerlings, M.G.D. Geers, An enhanced multi-scale approach for masonry wall computations with localization of damage, Numerical Meth Engineering 69 (2007) 1022–1059. https://doi.org/10.1002/nme.1799.

[87] T. Belytschko, S. Loehnert, J. Song, Multiscale aggregating discontinuities: A method for circumventing loss of material stability, Numerical Meth Engineering 73 (2008) 869–894. https://doi.org/10.1002/nme.2156.

[88] C.V. Verhoosel, J.J.C. Remmers, M.A. Gutiérrez, R. De Borst, Computational homogenization for adhesive and cohesive failure in quasi-brittle solids, Numerical Meth Engineering 83 (2010) 1155–1179. https://doi.org/10.1002/nme.2854.

[89] V.P. Nguyen, O. Lloberas-Valls, M. Stroeven, L.J. Sluys, Homogenization-based multiscale crack modelling: From micro-diffusive damage to macro-cracks, Computer Methods in Applied Mechanics and Engineering 200 (2011) 1220–1236. https://doi.org/10.1016/j.cma.2010.10.013.

[90] F.F. Abraham, J.Q. Broughton, N. Bernstein, E. Kaxiras, Spanning the continuum to quantum length scales in a dynamic simulation of brittle fracture, Europhys. Lett. 44 (1998) 783–787. https://doi.org/10.1209/epl/i1998-00536-9.

[91] E.B. Tadmor, M. Ortiz, R. Phillips, Quasicontinuum analysis of defects in solids, Philosophical Magazine A 73 (1996) 1529–1563. https://doi.org/10.1080/01418619608243000.

[92] G.J. Wagner, W.K. Liu, Coupling of atomistic and continuum simulations using a bridging scale decomposition, Journal of Computational Physics 190 (2003) 249–274. https://doi.org/10.1016/S0021-9991(03)00273-0.

[93] S.P. Xiao, T. Belytschko, A bridging domain method for coupling continua with molecular dynamics, Computer Methods in Applied Mechanics and Engineering 193 (2004) 1645–1669. https://doi.org/10.1016/j.cma.2003.12.053.

[94] P. Raghavan, S. Ghosh, Concurrent multi-scale analysis of elastic composites by a multi-level computational model, Computer Methods in Applied Mechanics and Engineering 193 (2004) 497–538. https://doi.org/10.1016/j.cma.2003.10.007.

[95] F.J. Vernerey, M. Kabiri, An adaptive concurrent multiscale method for microstructured elastic solids, Computer Methods in Applied Mechanics and Engineering 241–244 (2012) 52–64. https://doi.org/10.1016/j.cma.2012.04.021.

[96] S. Ghosh, J. Bai, P. Raghavan, Concurrent multi-level model for damage evolution in microstructurally debonding composites, Mechanics of Materials 39 (2007) 241–266. https://doi.org/10.1016/j.mechmat.2006.05.004.

[97] C. Bernardi, Y. Maday, A.T. Patera, Domain Decomposition by the Mortar Element Method, in: H.G. Kaper, M. Garbey, G.W. Pieper (Eds.), Asymptotic and Numerical Methods for Partial Differential Equations with Critical Parameters, Springer Netherlands, Dordrecht, 1993: pp. 269–286. https://doi.org/10.1007/978-94-011-1810-1_17.

[98] J. Guedes, N. Kikuchi, Preprocessing and postprocessing for materials based on the homogenization method with adaptive finite element methods, Computer Methods in Applied Mechanics and Engineering 83 (1990) 143–198. https://doi.org/10.1016/0045-7825(90)90148-F.

[99] V. Kouznetsova, M.G.D. Geers, W.A.M. Brekelmans, Multi-scale constitutive modelling of heterogeneous materials with a gradient-enhanced computational homogenization scheme, Numerical Meth Engineering 54 (2002) 1235–1260. https://doi.org/10.1002/nme.541.

[100] F. Feyel, J.-L. Chaboche, FE2 multiscale approach for modelling the elastoviscoplastic behaviour of long fibre SiC/Ti composite materials, Computer Methods in Applied Mechanics and Engineering 183 (2000) 309–330. https://doi.org/10.1016/S0045-7825(99)00224-8.

[101] V. Kouznetsova, M.G.D. Geers, W.A.M. Brekelmans, Multi-scale constitutive modelling of heterogeneous materials with a gradient-enhanced computational homogenization scheme, Numerical Meth Engineering 54 (2002) 1235–1260. https://doi.org/10.1002/nme.541.

[102] K. Matous, M. Kulkarni, P. Geubelle, Multiscale cohesive failure modeling of heterogeneous adhesives, Journal of the Mechanics and Physics of Solids 56 (2008) 1511–1533. https://doi.org/10.1016/j.jmps.2007.08.005.

[103] M.V. Cid Alfaro, A.S.J. Suiker, C.V. Verhoosel, R. De Borst, Numerical homogenization of cracking processes in thin fibre-epoxy layers, European Journal of Mechanics - A/Solids 29 (2010) 119–131. https://doi.org/10.1016/j.euromechsol.2009.09.006.

[104] F.V. Souza, D.H. Allen, Multiscale modeling of impact on heterogeneous viscoelastic solids containing evolving microcracks, Numerical Meth Engineering 82 (2010) 464–504. https://doi.org/10.1002/nme.2773.

[105] V.P. Nguyen, M. Stroeven, L.J. Sluys, An enhanced continuous–discontinuous multiscale method for modeling mode-I cohesive failure in random heterogeneous quasi-brittle materials, Engineering Fracture Mechanics 79 (2012) 78–102. https://doi.org/10.1016/j.engfracmech.2011.10.005.

[106] T. Belytschko, S. Loehnert, J. Song, Multiscale aggregating discontinuities: A method for circumventing loss of material stability, Numerical Meth Engineering 73 (2008) 869–894. https://doi.org/10.1002/nme.2156.

[107] U. De Maio, D. Cendón, F. Greco, L. Leonetti, P. Nevone Blasi, J. Planas, Investigation of concrete cracking phenomena by using cohesive fracture-based techniques: A comparison between an embedded crack model and a refined diffuse interface model, Theoretical and Applied Fracture Mechanics 115 (2021) 103062. https://doi.org/10.1016/j.tafmec.2021.103062.

[108] R.D.S.G. Campilho, M.D. Banea, J.A.B.P. Neto, L.F.M. Da Silva, Modelling adhesive joints with cohesive zone models: effect of the cohesive law shape of the adhesive layer, International Journal of Adhesion and Adhesives 44 (2013) 48–56. https://doi.org/10.1016/j.ijadhadh.2013.02.006.

[109] U. De Maio, F. Greco, L. Leonetti, R. Luciano, P. Nevone Blasi, S. Vantadori, A refined diffuse cohesive approach for the failure analysis in quasibrittle materials—part I: Theoretical

formulation and numerical calibration, Fatigue Fract Eng Mat Struct 43 (2020) 221–241. https://doi.org/10.1111/ffe.13107.

[110] M.R. Irshidat, M.H. Al-Saleh, Effect of using carbon nanotube modified epoxy on bond–slip behavior between concrete and FRP sheets, Construction and Building Materials 105 (2016) 511–518. https://doi.org/10.1016/j.conbuildmat.2015.12.183.

[111] O. Kononova, A. Krasnikovs, R. Stonys, G. Sahmenko, R. Vitols, INVESTIGATION OF INFLUENCE OF NANO-REINFORCEMENT ON THE MECHANICAL PROPERTIES OF COMPOSITE MATERIALS, JOURNAL OF CIVIL ENGINEERING AND MANAGEMENT 22 (2016) 425–433. https://doi.org/10.3846/13923730.2015.1106578.

[112] W. Meng, K.H. Khayat, Mechanical properties of ultra-high-performance concrete enhanced with graphite nanoplatelets and carbon nanofibers, Composites Part B: Engineering 107 (2016) 113–122. https://doi.org/10.1016/j.compositesb.2016.09.069.

[113] J. He, G. Xian, Y.X. Zhang, Numerical modelling of bond behaviour between steel and CFRP laminates with a ductile adhesive, International Journal of Adhesion and Adhesives 104 (2021) 102753. https://doi.org/10.1016/j.ijadhadh.2020.102753.

[114] G. Bilbie, C. Dascalu, R. Chambon, D. Caillerie, Micro-fracture instabilities in granular solids, Acta Geotech. 3 (2008) 25–35. https://doi.org/10.1007/s11440-007-0046-8.

[115] U. De Maio, F. Fabbrocino, F. Greco, L. Leonetti, P. Lonetti, A study of concrete cover separation failure in FRP-plated RC beams via an inter-element fracture approach, Composite Structures 212 (2019) 625–636. https://doi.org/10.1016/j.compstruct.2019.01.025.

[116] C.E.-I du B. (CEB-FIP), CEB-FIP Model Code for concrete structures 2010, (2013).

[117] T.J. Massart, R.H.J. Peerlings, M.G.D. Geers, An enhanced multi-scale approach for masonry wall computations with localization of damage, Numerical Meth Engineering 69 (2007) 1022–1059. https://doi.org/10.1002/nme.1799.

[118] M.G.D. Geers, V.G. Kouznetsova, W.A.M. Brekelmans, Multi-scale computational homogenization: Trends and challenges, Journal of Computational and Applied Mathematics 234 (2010) 2175–2182. https://doi.org/10.1016/j.cam.2009.08.077.

[119] F. Feyel, A multilevel finite element method (FE2) to describe the response of highly non-linear structures using generalized continua, Computer Methods in Applied Mechanics and Engineering 192 (2003) 3233–3244. https://doi.org/10.1016/S0045-7825(03)00348-7.

[120] U. De Maio, F. Greco, L. Leonetti, R. Luciano, P. Nevone Blasi, S. Vantadori, A refined diffuse cohesive approach for the failure analysis in quasibrittle materials—part II: Application to plain and reinforced concrete structures, Fatigue Fract Eng Mater Struct 42 (2019) 2764–2781. https://doi.org/10.1111/ffe.13115.

[121] M.R. Irshidat, M.H. Al-Saleh, H. Almashagbeh, Effect of carbon nanotubes on strengthening of RC beams retrofitted with carbon fiber/epoxy composites, Materials & Design 89 (2016) 225–234. https://doi.org/10.1016/j.matdes.2015.09.166.

[122] F. Greco, Homogenized mechanical behavior of composite micro-structures including micro-cracking and contact evolution, Engineering Fracture Mechanics 76 (2009) 182–208. https://doi.org/10.1016/j.engfracmech.2008.09.006.

[123] F. Greco, L. Leonetti, P. Nevone Blasi, Adaptive multiscale modeling of fiber-reinforced composite materials subjected to transverse microcracking, Composite Structures 113 (2014) 249–263. https://doi.org/10.1016/j.compstruct.2014.03.025.

[124] L.P. Canal, C. González, J. Segurado, J. LLorca, Intraply fracture of fiber-reinforced composites: Microscopic mechanisms and modeling, Composites Science and Technology 72 (2012) 1223–1232. https://doi.org/10.1016/j.compscitech.2012.04.008.

[125] G. Meschke, P. Dumstorff, Energy-based modeling of cohesive and cohesionless cracks via X-FEM, Computer Methods in Applied Mechanics and Engineering 196 (2007) 2338–2357. https://doi.org/10.1016/j.cma.2006.11.016.

[126] J. Oliver, M. Caicedo, A.E. Huespe, J.A. Hernández, E. Roubin, Reduced order modeling strategies for computational multiscale fracture, Computer Methods in Applied Mechanics and Engineering 313 (2017) 560–595. https://doi.org/10.1016/j.cma.2016.09.039.

[127] W.I. Hamad, J.S. Owen, M.F.M. Hussein, Modelling the degradation of vibration characteristics of reinforced concrete beams due to flexural damage: VIBRATION CHARACTERISTICS OF DAMAGED REINFORCED CONCRETE BEAMS, Struct. Control Health Monit. 22 (2015) 939–967. https://doi.org/10.1002/stc.1726.

[128] U. De Maio, F. Greco, L. Leonetti, R. Luciano, P. Nevone Blasi, S. Vantadori, A refined diffuse cohesive approach for the failure analysis in quasibrittle materials—part II: Application to plain and reinforced concrete structures, Fatigue Fract Eng Mater Struct 42 (2019) 2764–2781. https://doi.org/10.1111/ffe.13115.

[129] U. De Maio, F. Greco, L. Leonetti, R. Luciano, P. Nevone Blasi, S. Vantadori, A refined diffuse cohesive approach for the failure analysis in quasibrittle materials—part I: Theoretical formulation and numerical calibration, Fatigue Fract Eng Mater Struct 43 (2020) 221–241. https://doi.org/10.1111/ffe.13107.

[130] U. De Maio, F. Fabbrocino, F. Greco, L. Leonetti, P. Lonetti, A study of concrete cover separation failure in FRP-plated RC beams via an inter-element fracture approach, Composite Structures 212 (2019) 625–636. https://doi.org/10.1016/j.compstruct.2019.01.025.

[131] R.J. Allemang, D.L. Brown, A Correlation Coefficient for Modal Vector analysis, in: Proceeding of the 1st International Modal Analysis Conference 110-116, 1982.

[132] M.M. Abdel Wahab, G. De Roeck, DAMAGE DETECTION IN BRIDGES USING MODAL CURVATURES: APPLICATION TO A REAL DAMAGE SCENARIO, Journal of Sound and Vibration 226 (1999) 217–235. https://doi.org/10.1006/jsvi.1999.2295.

[133] Comsol AB, Comsol Multiphysics Physics Builder Manual, (2018).

[134] W.I. Hamad, J.S. Owen, M.F.M. Hussein, Modelling the degradation of vibration characteristics of reinforced concrete beams due to flexural damage: VIBRATION CHARACTERISTICS OF DAMAGED REINFORCED CONCRETE BEAMS, Struct. Control Health Monit. 22 (2015) 939–967. https://doi.org/10.1002/stc.1726.

[135] N. Baghiee, M. Reza Esfahani, K. Moslem, Studies on damage and FRP strengthening of reinforced concrete beams by vibration monitoring, Engineering Structures 31 (2009) 875–893. https://doi.org/10.1016/j.engstruct.2008.12.009.

[136] A. Pranno, F. Greco, P. Lonetti, R. Luciano, U. De Maio, An improved fracture approach to investigate the degradation of vibration characteristics for reinforced concrete beams under progressive damage, International Journal of Fatigue 163 (2022) 107032. https://doi.org/10.1016/j.ijfatigue.2022.107032.

[137] J.C. Gálvez, M. Elices, G.V. Guinea, J. Planas, [No title found], International Journal of Fracture 94 (1998) 267–284. https://doi.org/10.1023/A:1007578814070.